



DISSERTATION

Investigating Hot-Carrier Effects using the Backward Monte Carlo Method

ausgeführt zum Zwecke der Erlangung des akademischen Grades eines
Doktors der technischen Wissenschaften unter der Leitung von

Ao.Univ.Prof. Dipl.-Ing. Dr.techn. Hans KOSINA
E360 - Institut für Mikroelektronik

eingereicht an der Technischen Universität Wien
Fakultät für Elektrotechnik und Informationstechnik

von

DIPL. ING. MARKUS KAMPL

0925977 / E 786 710



Wien, im April 2019

Abstract

Hot carrier effects are a severe reliability concern in state-of-the-art transistors. Carriers with high energies influence the lifetime of MOSFET devices through the generation of defects in the gate dielectric. Any physically based model for hot-carrier-degradation requires a detailed description of the high-energy-tail of the energy distribution function (EDF). The EDF in a semiconductor device is determined by the Boltzmann transport equation which can be solved by the Monte Carlo (MC) method. Calculation of the high-energy-tail of the EDF using the traditional forward MC method, however, is very time-consuming. To overcome this problem, a stable backward MC method has been developed and implemented. If the carrier-energy of interest is high, a forward trajectory is very unlikely to gain so much energy, whereas in the backward method only these unlikely trajectories are considered, and no computation time is wasted with the vast majority of trajectories that do not gain the required energy. This fact allows the calculation of the drain current of a MOSFET in the entire sub-threshold region including the leakage current in the off-state. Symmetric current estimators are proposed which produce less statistical error than the non-symmetric ones. The significant difference compared to the original version of the backward method is that the transition rates for the backward trajectories are chosen to adhere to the principle of detailed balance. This property guarantees the stability of the numerical method and allows for a clear physical interpretation of the estimators. By assuming a Maxwellian distribution at an elevated temperature for the initial points of the backward trajectories, the method will generate more sampling points at higher energies. This method of statistical enhancement reduces the statistical error of quantities that depend on the high-energy tail of the EDF. The different estimators and their properties have been evaluated by simulations of an n-channel MOSFET. Strongly varying quantities can be resolved quickly over many orders of magnitude, such as the sub-threshold current and the EDF.

It is commonly accepted that electron-electron scattering alters the EDF and thus plays a vital part in physics-based hot-carrier degradation models. In this work, we assume an equilibrium distribution for the partner electrons. This model is suitable to describe the interaction of channel hot electrons with a reservoir of cold electrons in the drain region of a MOSFET. The single-particle scattering rate has been formally derived and implemented for both full-band and analytic band structure models. The scattering rate for the parabolic band approximation is obtained by analytic integration. The full-band scattering rate needs to be pre-calculated and stored for the MC simulations. It has been shown that the transition rates obtained from this model obey the principle of detailed balance. Thus, the presented model predicts a Maxwellian tail at high energies also in the presence of electron-electron scattering.

Kurzfassung

Heiße Ladungsträger stellen ein schwerwiegendes Zuverlässigkeitsproblem in modernen Transistoren dar. Ladungsträger mit hohen Energien beeinflussen die Lebensdauer von MOS Transistoren durch die Generation von Defekten im Gate-Dielektrikum. Jedes physikalische Modell der Degradation durch heiße Ladungsträger (engl. hot-carrier-degradation) benötigt eine detaillierte Beschreibung des Hochenergiebereiches der Ladungsträgerenergieverteilung. Diese Verteilung wird durch die Boltzmann-Transport-Gleichung bestimmt, welche durch eine Monte Carlo (MC) Methode gelöst werden kann. Bei der Berechnung des Hochenergiebereiches der Verteilung mittels der herkömmlichen Vorwärts-MC Methode wird jedoch sehr viel Rechenzeit benötigt. Um dieses Problem zu lösen, wurde eine stabile Version der Rückwärts-MC Methode entwickelt und implementiert. Wenn die zu untersuchende Ladungsträgerenergie hoch ist, wird eine herkömmliche Vorwärts-Trajektorie diese Energie nur sehr selten erreichen. In der Rückwärts-Methode jedoch werden nur diese unwahrscheinlichen Trajektorien berücksichtigt. Somit wird keine Rechenzeit mit dem Großteil der Trajektorien verschwendet, welche die benötigte Energie nie erreichen. Diese Eigenschaft der Rückwärts-Methode führt dazu, dass man für einen MOS Transistor den Drainstrom im gesamten Sub-Threshold Bereich bis hin zum Leckstrom im ausgeschalteten Zustand berechnen kann. Es werden symmetrische Stromschätzer vorgestellt, die einen geringeren statistischen Fehler aufweisen als die nicht-symmetrischen. Der wichtigste Unterschied der verwendeten Rückwärts-Methode gegenüber der ursprünglichen Methode besteht darin, dass die Rückwärts-Trajektorien so gewählt werden, dass sie das Prinzip des detaillierten Gleichgewichts einhalten. Diese Eigenschaft garantiert die numerische Stabilität der Methode und erlaubt eine physikalische Interpretation des Strom-Schätzers. Wenn die Zustände der injizierten Teilchen aus einer Maxwellverteilung mit erhöhter Temperatur gewählt werden, so besitzen diese Teilchen im Mittel eine höhere Energie. Diese statistische Anreicherung reduziert den statistischen Fehler von jenen Größen, die vom Hochenergiebereich der Verteilungsfunktion abhängen. Verschiedene Strom-Schätzer und deren Eigenschaften wurden anhand von Simulationen eines n-Kanal MOSFET untersucht. Physikalische Größen können verhältnismäßig schnell über mehrere Größenordnungen aufgelöst werden, wie etwa der Sub-Threshold-Strom und die Ladungsträgerverteilung.

Es wird allgemein angenommen, dass die Elektron-Elektron-Streuung den Hochenergiebereich der Ladungsträgerverteilung verändert. Dadurch spielt sie eine wichtige Rolle in physikalischen Degradationsmodellen. Die vorliegende Arbeit nimmt eine Gleichgewichtsverteilung für die Partnerelektronen an. Dieses Modell eignet sich um die Interaktion von heißen Ladungsträgern mit einem Reservoir von kalten Ladungsträgern im Draingebiet eines MOSFET zu beschreiben. Die Einteilchen-Streureate wurde für analytische sowie numerische Bandstrukturen hergeleitet und implementiert. Die Streureate für ein parabolisches Band kann mittels analytischer Integration berechnet werden. Im Fall einer numerischen Bandstruktur muss man im Vorfeld für jede MC Simulation die Streureate numerisch berechnen und in einer Tabelle ablegen. Es wurde gezeigt, dass die Einteilchen-Streureate des vorgestellten Modells das Prinzip des detaillierten Gleichgewichts erfüllt. Somit wird er maxwellsche Energieabfall des Hochenergiebereiches durch die Elektron-Elektron Streuung laut diesem Modell nicht verändert.

Contents

List of Figures	vii
1. Introduction	1
1.1. Motivation	1
1.2. Modeling Approaches	1
1.3. Outline	3
2. Semi-Classical Transport Theory	5
2.1. Band-Structure	5
2.1.1. Reciprocal Lattice	6
2.1.2. Parabolic Band Approximation	9
2.1.3. Non-Parabolic Band Approximation	11
2.1.4. Full-Band Structure	12
2.2. Semiclassical Electron Dynamics	13
2.3. Scattering	14
2.3.1. Impurity Scattering	15
2.3.2. Phonon Scattering	16
2.3.3. Carrier-Carrier Scattering	16
2.4. The Boltzmann Transport Equation	17
3. Transport Modeling Approaches	19
3.1. Method of Moments	19
3.1.1. The Drift Diffusion Model	22
3.2. Spherical harmonic expansion	23
3.3. Monte Carlo Method	24
3.3.1. Monte Carlo Integration	24
3.3.2. Generation of Random Numbers	25
3.3.3. Duration of the Free Flight	26
3.3.4. Selection of the Scattering Process	27
3.3.5. Generation of an Equilibrium Distribution	28
3.3.6. Calculation of Equilibrium Averages	31
3.3.7. Estimation of Non-Equilibrium Averages	31
3.3.8. Current Estimation	36

4. Backward Monte Carlo Method	39
4.1. Theory of the Backward Monte Carlo Method	40
4.1.1. Probability Density Functions	41
4.1.2. The Backward MC Method	42
4.2. Current Estimators	45
4.2.1. The Boundary Distribution	46
4.2.2. Injection from an Equilibrium Maxwellian	47
4.2.3. Injection from a Velocity-weighted Maxwellian	48
4.2.4. Injection from a Non-equilibrium Maxwellian	48
4.2.5. Injection from the Equilibrium Concentration	49
4.2.6. Symmetric Sampling	51
4.2.7. Estimation of the Statistical Error	51
4.3. Multi-Band Semiconductors	52
4.4. The Combined Backward-Forward MC Method	53
4.5. Results and Discussion	54
4.5.1. Transfer Characteristics	55
4.5.2. Output Characteristics	58
4.5.3. Injection from a Non-equilibrium Distribution	60
4.5.4. Energy Distribution Function	62
4.5.5. Hot Carrier Degradation	62
4.6. Conclusion	64
5. Electron-Electron Scattering	65
5.1. Matrix Element	65
5.2. Two-particle Transition Rate	67
5.2.1. Principle of Detailed Balance	67
5.3. Single-particle Transition Rate	68
5.3.1. Spin Degeneracy and Normalization	69
5.3.2. A Model for the Partner Electrons	70
5.3.3. Principle of Detailed Balance	70
5.3.4. Angular Integration of the Transition Rate	71
5.3.5. Transition Rate for Boltzmann Statistics	73
5.3.6. Transition Rate for Fermi Dirac Statistics	74
5.4. Implementation for Full-Band Structures	75
5.4.1. Total Scattering Rate	75
5.4.2. Obtaining the Final State	75
5.5. Implementation for Parabolic and Isotropic Bands	78
5.5.1. The Total Scattering Rate for Boltzmann Statistics	78
5.5.2. Two-particle Scattering Rate for Boltzmann Statistics	80
5.5.3. Single-particle Scattering Rate for Boltzmann Statistics	82
5.5.4. Random Selection of the Momentum Transfer q	83
5.6. Results and Discussion	84
5.6.1. Screened Coulomb Scattering Mechanisms	84
5.6.2. Results for Bulk Silicon	84
5.6.3. Results for an $n^+n^-n^+$ Diode	85
5.6.4. Results for a n-channel MOSFET	86

6. Outlook and Conclusion	91
6.1. Possible Further Improvements of the BMC Method	91
6.1.1. Combination of Methods	91
6.2. Possible Further Improvements for the EES	92
6.3. Conclusion	92
A. Integration over the Brillouin Zone	95
A.1. The partition function	95
A.2. Average Energy and Injection Velocity	96
A.3. Fourier Transform of the Screened Coulomb Potential	98
A.4. The Normalized Maxwell-Boltzmann Distribution	99
A.4.1. Evaluating the Transition Rate Integral	99
A.5. The Normalized Fermi-Dirac Distribution	100
A.5.1. Evaluating the Transition Rate Integral	100
A.5.2. Asymptotic behaviour of EES	101
Bibliography	103
List of Publications	115

List of Figures

2.1.	Band-structure of a one-dimensional lattice from the Kronig-Penny model [55]. The (first) Brillouin zone is indicated in red.	7
2.2.	Face-centered-cubic structure and its base-vectors	8
2.3.	<u>Light gray:Brillouin zone of silicon; dark gray:the irreducible wedge</u>	9
2.4.	Symmetry operations for a cubic lattice	10
2.5.	Valley approximation of a band-structure. The Γ -valley is in the point $\mathbf{k} = (0, 0, 0)$. The X-valley is along the $\langle 100 \rangle$ direction but not necessarily on the X-symmetry point. The L-valley is along the $\langle 111 \rangle$ direction in the L-symmetry point.	11
2.6.	Ellipsoidal constant energy surfaces of the X-valleys.	12
2.7.	Silicon full-band-structure (picture taken from [60])	13
2.8.	Comparison of the dispersion relation of unstrained silicon in direction of the [100] axis with both parabolic and non-parabolic approximations, as well as EPM.	14
2.9.	Scattering of the wave-vector \mathbf{k} into \mathbf{k}' by the perturbation potential $U_S(\mathbf{r}, t)$	15
2.10.	Illustration of the continuity aspect in \mathbf{k} and \mathbf{r} space of the BTE	18
3.1.	The scattering rate $\lambda(t)$, the picewise constant scattering rate $\Gamma(t)$ and the global maximum Γ_{\max}	28
3.2.	Sampling using the box method.	29
3.3.	Sampling using the before-scattering method.	30
3.4.	Constant time sampling method.	30
3.5.	Boundary method sampling in a device. The dashed lines are the boundaries between the Voronoi volumes.	33
3.6.	Conduction band edge (red) and the electron density (blue) in an $n^+n^-n^+$ diode with abrupt junctions.	34

List of Figures

3.7.	Comparison of two different averaging methods in an silicon $n^+n^-n^+$ diode with constant and variable grid size. Both images show the region around the n^+n^- junction at 200 nm.	35
3.8.	Sketch of a device contact in the x - z plane.	36
4.1.	Principle of the backward MC method applied to a MOSFET. The injected particle has a chosen state in r - and k -space. A trajectory is traced back in time to its origin to calculate its weight [P4]. . . .	40
4.2.	Illustration of a backward trajectory starting at time t_0 and reaching time 0 after three free flights. The symbols used in the estimator (4.16) are shown.	43
4.3.	Unstable BMC algorithm. Particle tend to higher energies.	44
4.4.	Stable BMC algorithm, satisfying the principle of detailed balance.	45
4.5.	Principle of the combined backward-forward MC method for a MOSFET. The injected particle has a chosen state in \mathbf{r} - and \mathbf{k} -space. A trajectory is traced back in time to its origin to calculate the weight. The local attributes are calculated from the weighted forward trajectories [P4].	54
4.6.	Sketch of a MOSFET.	55
4.7.	Transfer characteristics of the nMOSFET for two drain voltages, simulated with Minimos-NT, the backward and the forward MC methods.	56
4.8.	Relative Error (relative standard deviation) of the drain current for two drain voltages. Each bias point is calculated with 10^6 backward trajectories. The current estimator (4.37) was used.	57
4.9.	Computation times by a single core of an Intel i7 processor. The operating points of the transfer characteristics at $V_{DS} = 2.2$ V are considered. A relative standard deviation of 10^{-2} is assumed. . . .	57
4.10.	Output characteristics of the MOSFET for two gate voltages, simulated with MinimosNT, the forward and the backward MC methods.	58
4.11.	Relative errors of the output characteristics at two gate voltages. The non-symmetric and the symmetric estimator based on the velocity-weighted Maxwellian are compared. Each bias point involves the calculation of 10^6 backward trajectories.	59
4.12.	Temperature stability of the current estimators (4.37), (4.39) and (4.56) which are based, respectively, on a Maxwellian (MW) and a velocity-weighted Maxwellian (vel.weighted MW) injection PDF. Operating point is $V_{GS} = 0.6$ V and $V_{DS} = 2.2$ V.	60
4.13.	Comparison of the relative errors of the current estimators (4.37), (4.39) and (4.56). Operating point is $V_{GS} = 0.6$ V and $V_{DS} = 2.2$ V. . . .	61

4.14. Energy distribution function for full-bands at three surface points in the channel. The distances from the left edge of the gate electrode are given. Operating point is $V_{GS} = 2.2\text{ V}$ and $V_{DS} = 2.2\text{ V}$. Solid lines: Forward MC simulation with 10^9 trajectories. Dotted lines: High energy tails computed with the backward MC method. 62

4.15. Acceleration integral for a 65nm nMOS, simulated with FMC and BMC method at different injection temperatures. 63

5.1. All contributing neighbors of a point \mathbf{k}_n are recursively included. In the first step, all direct neighbours are added. For the second and third step, the tetrahedrons $\text{Tet}_{2,1}$ and $\text{Tet}_{2,1,1}$, respectively, are exemplarily illustrated. For the calculation of the scattering rate, all tetrahedra are represented by the center \mathbf{k}_m and their volume V_m . 76

5.2. Electron-electron scattering rate calculated from (5.86) assuming $m = 0.3m_0$, $\epsilon_s = 11.68\epsilon_0$ and $T = 300\text{ K}$ and the electron concentrations $n = 10^{17}/10^{18}/10^{19}\text{ cm}^{-3}$. The dashed line represents the unscreened limit of the scattering rate. 85

5.3. Ionized-impurity scattering rate obtained from the Brooks-Herring model [43] for the same parameters as in Fig. 5.2. 86

5.4. Conduction band edge in a $n^+n^-n^+$ diode with abrupt junctions. The total electron density (S+D) and the partial density due to electrons injected from the source contact (S) are shown. 87

5.5. Average electron energy in the $n^+n^-n^+$ diode. The upper curves (S) consider only the (hot) electrons originating from the source region and clearly show the additional energy relaxation due to EES. The lower curves (S+D) consider all electrons and show a stronger carrier cooling because in addition to energy relaxation there occurs also a mixing of the hot carriers with the cold carriers in the drain. . . . 88

5.6. EDF at three surface points in the channel of a MOSFET with and without EES. A parabolic dispersion is assumed in the transport model to be consistent with the EES-rate (5.86). 89

5.7. EDF at three surface points in the channel with EES and fullband effects included. The backward MC simulation accounts for interaction with cold drain electrons and predicts a Maxwellian tail (dashed line). ViennaSHE considers interaction with non-equilibrium electrons at fixed energy and severely overestimates the high-energy tail. 90

6.1. Combination of the approaches in Fig. 4.3 and Fig. 4.4. 92

List of Acronyms

BMC	backward Monte Carlo
BTE	Boltzmann transport equation
BZ	Brillouin zone
DD	drift diffusion
DF	distribution function
EDF	energy distribution function
EES	electron-electron scattering
FMC	forward Monte Carlo
HC	hot carrier
HCD	hot carrier degradation
MC	Monte Carlo
MOSFET	metal oxide semiconductor field effect transistor
nMOS	n channel MOSFET
SHE	spherical harmonics expansion
VMC	Vienna Monte Carlo Simulator

Chapter 1

Introduction

This chapter pictures the motivation for this work and presents a brief outline of the same.

1.1. Motivation

With the down-scaling of semiconductor devices, a detailed understanding of the underlying physical processes is required in order to further improve device performance. To gain some insights into modern semiconductor devices through numerical simulations, accurate, theoretical descriptions of carrier transport fundamentals have to be available. Technology Computer Aided Design (TCAD) has become a powerful tool for the development of faster, smaller and more power-efficient devices [87].

Scaling influences the reliability of semiconductor devices due to single point defects and a small amount of dopants in the channel, leading to fluctuation in the electrostatic potential [6]. Hot-carrier degradation (HCD) is a severe reliability concern in state-of-the-art transistors. Thus, for an accurate description of the HCD effect, a detailed description of the high-energy tail of the carrier distribution function is needed. Due to small device geometries and low supply voltages the hot-carriers result mainly from scattering processes in the semiconductor [104].

1.2. Modeling Approaches

Transport models for semiconductor devices are commonly based on the Boltzmann Transport Equation (BTE) [65]. One method, derived from the BTE, is the drift-diffusion (DD) model. Based on the first two moments of the BTE, the DD model is neglecting non-local effects. This method became very popular for

1. Introduction

macroscopic devices in the last century. Till today the DD model is used as a trade-off between computational efficiency and accuracy [30, 33, 82, 91–93].

With shrinking device geometry and the need to include hot-carrier effects, this method suffers some severe drawbacks. In particular, the DD model assumes that the average carrier energy is in equilibrium with the local electric field. This assumption has been shown to be invalid as the average carrier energy lags behind the electric field [27, 30]. The DD model is unable to calculate non-local effects and all kinds of hot carrier effects [28, 87, 97]. Despite these limitations, there are some attempts to estimate the high-energy-tail within the DD model [92]. The DD model includes the first two moments of BTE. Including more moments of the BTE leads to the hydrodynamic and energy-transport models. However, for small devices, they often do not deliver the expected improved accuracy. For higher accuracy in smaller devices a six moments model was proposed [29].

In the 1970s a stochastic approach for the solution of the BTE became popular. The Monte Carlo method is based on the calculation of random carrier trajectories in a semiconductor. The trajectory calculation takes into account realistic band-structure models and various kinds of scattering processes in the semiconductor [21, 34, 43, 51, 59, 61].

In the beginning, an analytic model of the semiconductor band structure was sufficient for Monte Carlo simulations, but with the growing significance of hot-carrier effects, a more accurate band structure model was required. This accuracy was achieved by calculating the full-band structure of a semiconductor numerically and embedding it into the Monte Carlo simulation [65].

A problem in hot-carrier modeling is that Monte Carlo is a stochastic method and therefore a huge number of carrier trajectories is needed for obtaining an adequate ensemble of rare states representing the hot-carriers. A solution to this problem was suggested in the late 1980s, known as the backward Monte Carlo method. The theory is based on generating the states of hot-carriers in a device first and letting the carriers travel back in time to their origin at an injecting contact. With this backward Monte Carlo (BMC) algorithm, the probability of each hot-carrier state can be calculated, and no other carriers than those of interest have to be simulated. This brings a vast decrease in simulation time. The initial version of this algorithm was numerically unstable. Therefore, it was never implemented in a semiconductor device simulator [45, 73].

In 2003, a stable backward Monte Carlo algorithm was proposed [61] and finally implemented in a semiconductor device simulator in 2015 [P4]. The backward Monte Carlo method is able to overcome the statistical drawbacks of the conventional Monte Carlo method. In particular, the capability to include particles with arbitrary energies and the usage of full-bands, is giving this method an advantage

over simulators using conventional Monte Carlo algorithms or deterministic solvers [P4, 62].

A deterministic method to solve the BTE is based on spherical harmonics expansion (SHE). This method relies on the spherical symmetry for the band-structure model. Thus, the dispersion relation for higher energies is not well represented [22, 24, 25, 39, 40, 50, 84, 87].

1.3. Outline

Chapter 2 focuses on the semi-classical transport theory and shows basic equations to describe the transport in a semiconductor device. The limitations are also discussed. The classical propagation as particles and the quantum-mechanical scattering are described there. Further, the fundamentals of band-structure calculation are briefly addressed.

Chapter 3 is dealing with different approaches to model the carrier transport in a semiconductor device. The solution of the BTE can be estimated by using the method of moments and its well-known representative, the drift-diffusion (DD) equations, by using spherical harmonics expansion (SHE) and solving the BTE deterministically, or by a stochastic solution method called Monte Carlo. All these methods have their advantages and drawbacks, which will be discussed there.

Chapter 4 describes the backward MC method proposed in the 1980s and its mathematical stability problems. A stable method, proposed in 2003 and its implementation, as well as various current estimators are discussed in this chapter. Moreover, results of semiconductor device simulations presented.

Chapter 5 is focused on the modeling of electron-electron scattering (EES). With the BMC method, there is now a possibility to investigate hot-carriers in MC simulations more efficiently. This chapter introduces an EES model derived from physical reflections to describe the relaxation of channel hot-carriers in the drain region of a MOSFET.

Chapter 2

Semi-Classical Transport Theory

In quantum mechanics, electrons are treated as waves. For semiconductor devices with a slowly varying potential profile, however, carriers can be described classically as particles [65]. The interaction with the surroundings is modeled by scattering processes. The term *semi-classical*, in turn, stems from the conjoined classical electron dynamic and the quantum-mechanical treatment of scattering processes. The classical electron dynamic is derived from the band-structure of the material.

2.1. Band-Structure

Quantum-mechanics provides the basics to describe the possible states of carriers in a semiconductor lattice [60, 89]. The lattice is described with a periodic energy potential. The state of a carrier is described by its wave function, which is the solution of the Schrödinger Equation of the system [65].

$$i\hbar \frac{\partial \Psi}{\partial t} = -\frac{\hbar^2}{2m_0} \nabla^2 \Psi + [E_{C0}(\mathbf{r}) + U_C(\mathbf{r}) + U_S(\mathbf{r}, t)] \Psi(\mathbf{r}, t). \quad (2.1)$$

The probability density of finding a electron in (\mathbf{r}, t) is represented by $|\Psi(\mathbf{r}, t)|^2$. The potential energy in the equation above has three different parts [60]. The first part, $E_{C0}(\mathbf{r})$, is the so-called built-in potential which results from the distribution of the ionized dopands in the semiconductor. The second part, $U_C(\mathbf{r})$, is the periodic crystal potential which results from the atoms' electrostatic potential. And the third part, $U_S(\mathbf{r}, t)$, is the scattering potential, which describes random potential fluctuations causing scattering processes. Further details about scattering mechanisms will be discussed later in this thesis.

2. Semi-Classical Transport Theory

Neglecting both built-in and scattering potential, Schrödinger's Equation solely depends on the periodic crystal potential. Thus the time-independent Schrödinger Equation is given by [60]:

$$\left(-\frac{\hbar^2}{2m_0}\nabla^2 + U_C(\mathbf{r})\right)\Psi(\mathbf{k}, \mathbf{r}) = \mathcal{E}(\mathbf{k})\Psi(\mathbf{k}, \mathbf{r}), \quad (2.2)$$

The wave-function in a periodic potential has the form of a Bloch wave [55, 77],

$$\Psi(\mathbf{k}, \mathbf{r}) = \frac{1}{\sqrt{\Omega}}u_k(\mathbf{r})e^{i\mathbf{k}\cdot\mathbf{r}}, \quad (2.3)$$

where Ω represents the crystal volume, and $\mathbf{p} = \hbar\mathbf{k}$ represents the crystal momentum. The Bloch functions are periodic,

$$u_k(\mathbf{r} + \mathbf{a}) = u_k(\mathbf{r}) \quad (2.4)$$

where \mathbf{a} is a vector of the direct lattice. When inserting the Bloch waves in the one-electron wave equation (2.2) with the periodicity condition (2.4), discrete eigenvalues

$$\mathcal{E}_n(\mathbf{k}) \quad n = 1, 2, \dots \quad (2.5)$$

can be obtained [65]. Every eigenvalue is periodic in \mathbf{k} -space.

$$\mathcal{E}_n(\mathbf{k}) = \mathcal{E}_n(\mathbf{k} + \mathbf{K}), \quad (2.6)$$

where \mathbf{K} is a vector of the reciprocal lattice. Each eigenvalue $\mathcal{E}_n(\mathbf{k})$ represents one band of the semiconductor. Because of its periodicity, all the information is included in one period which is called the Brillouin zone [65]. The band-structure of a one-dimensional lattice is shown in Fig. 2.1.

The electron-wave can propagate in three dimensions. Thus, the Brillouin zone is a volume [65]. The resulting geometric shape can be determined from the reciprocal lattice-vectors.

2.1.1. Reciprocal Lattice

The diamond structure of the silicon crystal comes with two atoms in its primitive cell. This kind of lattice can be represented as two intertwining face-centered-cubic (FCC) structures, see Fig. 2.2. Every point of the diamond lattice can be described with the following base-vectors [1, 36, 55, 96, 99, 111]:

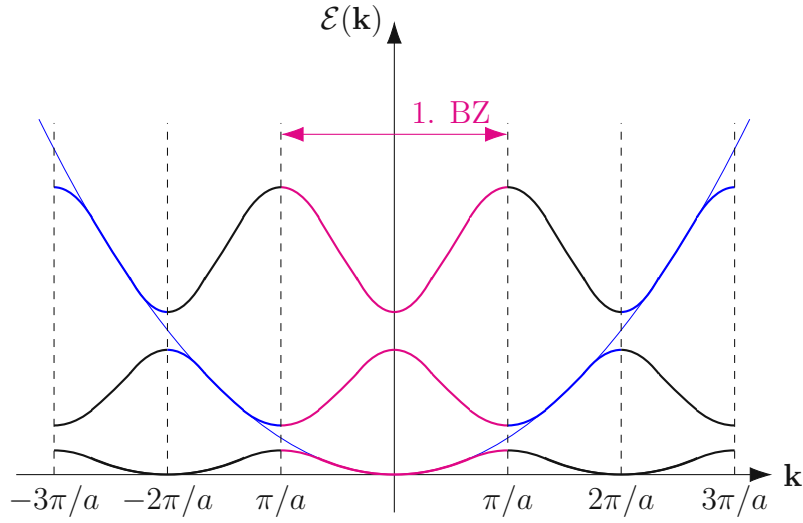


Figure 2.1.: Band-structure of a one-dimensional lattice from the Kronig-Penny model [55]. The (first) Brillouin zone is indicated in red.

$$\mathbf{a}_1 = \frac{a}{2} (\mathbf{e}_y + \mathbf{e}_z), \quad (2.7)$$

$$\mathbf{a}_2 = \frac{a}{2} (\mathbf{e}_x + \mathbf{e}_z), \quad (2.8)$$

$$\mathbf{a}_3 = \frac{a}{2} (\mathbf{e}_x + \mathbf{e}_y), \quad (2.9)$$

$$(2.10)$$

where a is the lattice constant of the crystal. The base-vectors $(\mathbf{a}_1, \mathbf{a}_2, \mathbf{a}_3)$ of the crystal lattice can be transformed in base-vectors $(\mathbf{b}_1, \mathbf{b}_2, \mathbf{b}_3)$ of the reciprocal lattice [54], which represent wave vectors [20, 96]:

$$\mathbf{b}_1 = 2\pi \frac{\mathbf{a}_2 \times \mathbf{a}_3}{\mathbf{a}_1 \cdot (\mathbf{a}_2 \times \mathbf{a}_3)}, \quad (2.11)$$

$$\mathbf{b}_2 = 2\pi \frac{\mathbf{a}_3 \times \mathbf{a}_1}{\mathbf{a}_1 \cdot (\mathbf{a}_2 \times \mathbf{a}_3)}, \quad (2.12)$$

$$\mathbf{b}_3 = 2\pi \frac{\mathbf{a}_1 \times \mathbf{a}_2}{\mathbf{a}_1 \cdot (\mathbf{a}_2 \times \mathbf{a}_3)}. \quad (2.13)$$

$$(2.14)$$

The reciprocal lattice of the FCC lattice is face-centered cubic [110]. A Brillouin zone is defined as a Wigner-Seitz primitive cell in the reciprocal lattice [55]. The

2. Semi-Classical Transport Theory

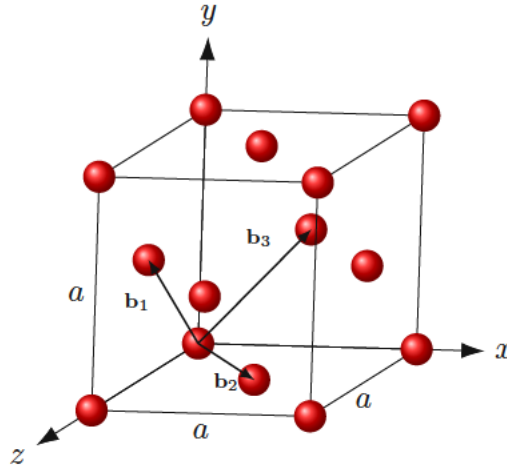


Figure 2.2.: Face-centered-cubic structure and its base-vectors

Brillouin zone of Silicon is a truncated octahedron [53, 67], shown in Fig 2.3. The band structure in this volume is highly symmetric and can be represented in just a fraction of the full volume and several symmetry operations. In the case of a cubic lattice, there are 48 symmetry operations [65]:

- 8 mirroring operations across a (100) plane
- 2 mirroring operations across a (110) plane
- and 3 rotation by $2\pi/3$ along the [111] direction.

These operations are illustrated in Fig 2.4. This fraction of the Brillouin zone is called irreducible wedge and is defined by [65]

$$\begin{aligned} 0 \leq k_z \leq k_x \leq k_y \leq 2\pi/a \\ k_x + k_y + k_z \leq 3\pi/a \end{aligned} \quad (2.15)$$

Fig. 2.3 shows the irreducible wedge and also the standard notation of the symmetry points in the Brillouin zone:

- Γ represents the point $\mathbf{k} = 0$
- X represents the points at the BZ boundary in $\langle 100 \rangle$ directions
- L represents the points at the BZ boundary along the $\langle 111 \rangle$ diagonals

At the symmetry points or along the axes between these symmetry points, there are often local minimum or maxima of the $\mathcal{E}(\mathbf{k})$ relation, also called valleys. In simple band-structure models, every valley is approximated by a quadratic function as shown in Fig. 2.5.

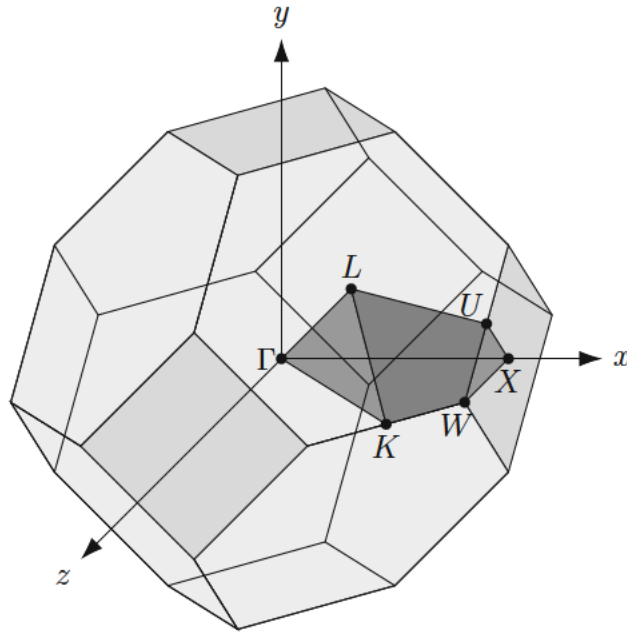


Figure 2.3.: Light gray: Brillouin zone of silicon; dark gray: the irreducible wedge

2.1.2. Parabolic Band Approximation

Band-structures for commonly used semiconductors are known through experiments and numerical calculations [65]. The majority of electrons will stay at lower energies and will not reach most of the areas in the band-structure where energies are higher. Approximations are used to describe this majority of carriers around the energy minimum. For a given band-structure, a Taylor expansion can be performed [65].

$$\mathcal{E}(\mathbf{k}) = \mathcal{E}(0) + \left. \frac{\partial \mathcal{E}(\mathbf{k})}{\partial \mathbf{k}} \right|_{\mathbf{k}=0} \mathbf{k} + \frac{1}{2} \left. \frac{\partial^2 \mathcal{E}(\mathbf{k})}{\partial \mathbf{k}^2} \right|_{\mathbf{k}=0} \mathbf{k}^2 + \dots \quad (2.16)$$

The linear term is always zero for a minimum or a maximum. For semiconductors, where the energy minimum is at $\mathbf{k} = 0$, the quadratic approximation can be written as

$$\mathcal{E}(\mathbf{k}) = \mathcal{E}(0) + \frac{\hbar^2 \mathbf{k}^2}{2m^*}, \quad (2.17)$$

where

$$\frac{1}{m^*} = \frac{1}{\hbar^2} \frac{\partial^2 \mathcal{E}(\mathbf{k})}{\partial \mathbf{k}^2} \quad (2.18)$$

2. Semi-Classical Transport Theory

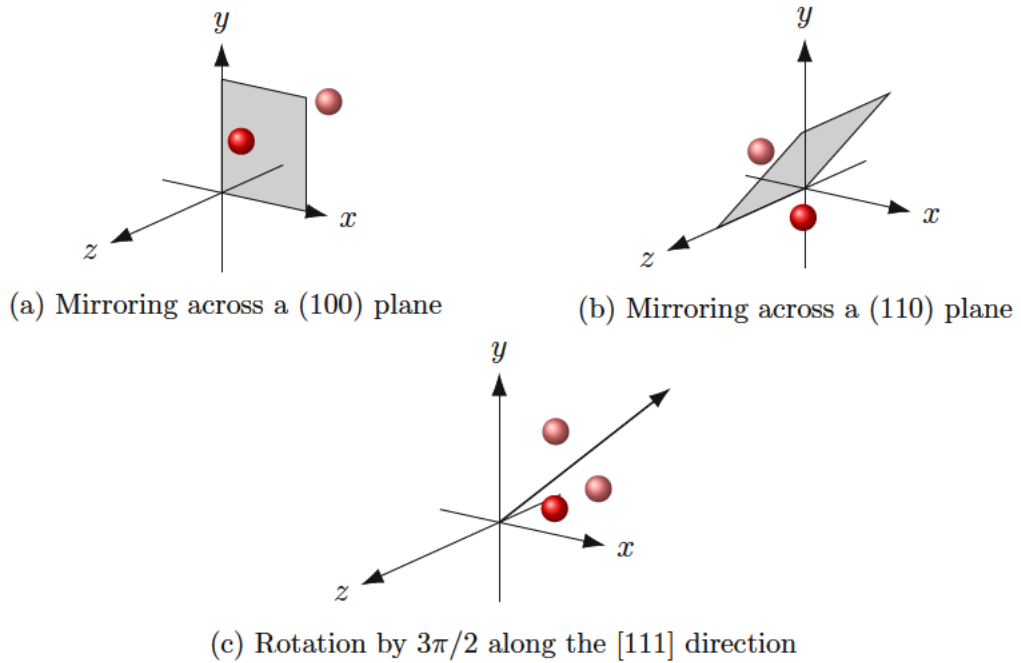


Figure 2.4.: Symmetry operations for a cubic lattice

is the effective mass of one specific band-structure minimum [65]. This approximation shows that the electrons in a crystal can be treated like free electrons with different masses around the energy minimum.

The effective mass often display different values depending on the crystallographic orientation [65]. If a valley has rotational symmetry along one axis the effective mass can be split into one transversal and one longitudinal mass. In this case, (2.17) changes to

$$\mathcal{E}(\mathbf{k}) = \mathcal{E}(\mathbf{k}_0) + \frac{\hbar^2}{2} \left[\frac{k_l^2}{m_l^*} + \frac{k_t^2}{m_t^*} \right]. \quad (2.19)$$

This equation describes a band-structure with ellipsoidal constant energy surfaces in the main directions of silicon [102], shown in figure Fig. 2.6. Equation (2.19) uses a tensor for the effective mass and describes the conduction bands in the X-valleys and the L-valleys.

The parabolic band approximation is derived for energies around the band minimum. At higher energies, other band structure models are required [46].

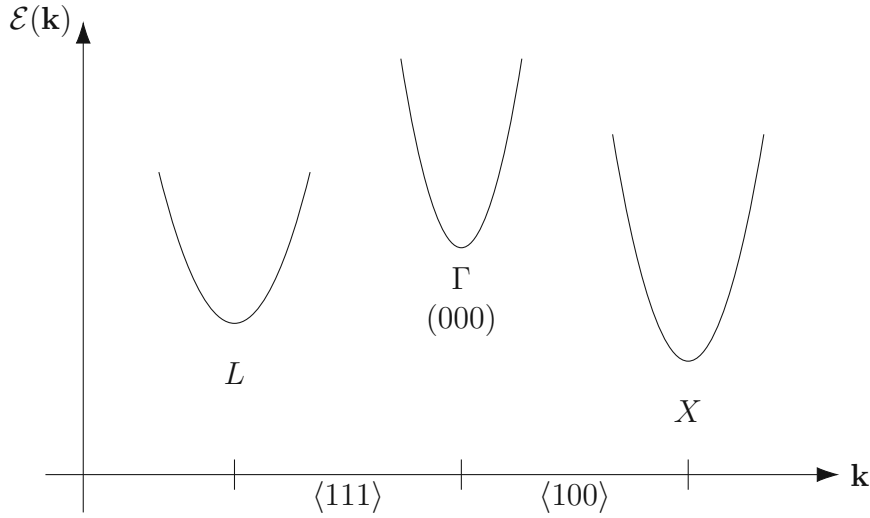


Figure 2.5.: Valley approximation of a band-structure. The Γ -valley is in the point $\mathbf{k} = (0, 0, 0)$. The X-valley is along the $\langle 100 \rangle$ direction but not necessarily on the X-symmetry point. The L-valley is along the $\langle 111 \rangle$ direction in the L-symmetry point.

2.1.3. Non-Parabolic Band Approximation

For high applied fields, carriers may reach energies far above the minimum, and higher order terms in the Taylor series expansion (2.16) cannot be ignored. For the conduction band, non-parabolicity is often described by a relation of the form [21, 44, 65, 68]:

$$\mathcal{E}(1 + \alpha\mathcal{E}) = \frac{\hbar^2 \mathbf{k}^2}{2m^*}, \quad (2.20)$$

where m^* is the effective mass at the minimum and α is non-parabolicity factor. For a direct semiconductor the non-parabolic factor of the Γ -valley is given by [102]

$$\alpha = \frac{1}{E_g} \left(1 - \frac{m^*}{m_0} \right), \quad (2.21)$$

with E_g being the energy gap.

2. Semi-Classical Transport Theory

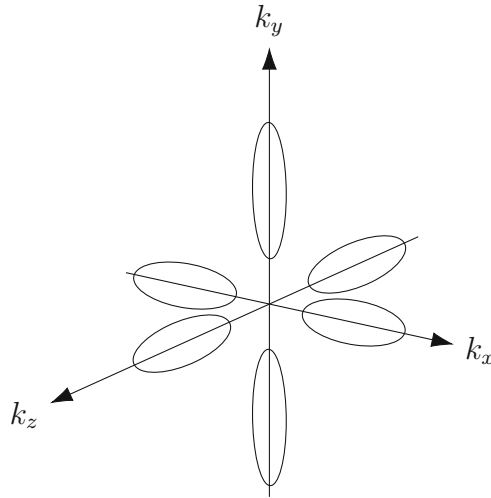


Figure 2.6.: Ellipsoidal constant energy surfaces of the X-valleys.

2.1.4. Full-Band Structure

The non-parabolic band approximation can be used for energies up to 2 eV [65]. For carriers with higher kinetic energies, a more detailed description of the $\mathcal{E}(\mathbf{k})$ relation is needed. Models of physical processes such as impact ionization and carrier-carrier scattering, as well as reliability models are relying on an accurate description of high-energy carriers [P3]. A commonly used method to handle carriers with higher energies is the full-band-structure [105], where the complete $\mathcal{E}(\mathbf{k})$ relation in the irreducible wedge of the Brillouin zone is provided [110]. The band-structure can be found by solving the Schrödinger Equation (2.1).

Empirical Pseudopotential Method

The empirical pseudopotential method is an effective way of calculating band structures of various materials. The method is derived from the orthogonal plane wave method [35] and the Phillips-Kleinman cancellation theorem [16, 17, 76, 96]. The key simplifications of this method is that the valence electrons determine the band-structure and the effect of the core electrons can be neglected [96]. The resulting potential, which is used in the Schrödinger equation, is expanded into a Fourier series over the reciprocal lattice [105, 112]. The coefficients of this series are altered with form factors to fit the empirical data [56, 96]. One reason for the popularity of the empirical pseudopotential method is the low number of parameters. Furthermore, the results yielded by this method are in many cases more accurate than ab-initio calculations [105]. Fig. 2.7 shows the band-structure in silicon, calculated

by the empirical pseudopotential method [101].

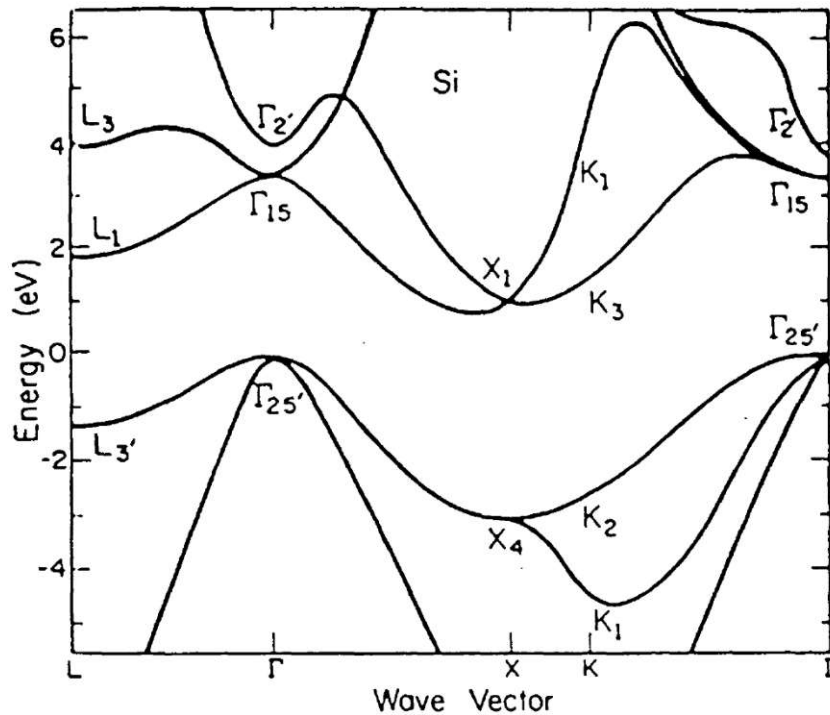


Figure 2.7.: Silicon full-band-structure (picture taken from [60])

The three different band-structure approximations introduced above are compared for unstrained silicon in Fig 2.8, where the dispersion relation along the [100] direction is illustrated. Moreover, it shows the need for a detailed description of the band structure above 2 eV.

2.2. Semiclassical Electron Dynamics

In semiconductor devices, where the built-in potential varies very slowly, quantum-mechanical effects like tunneling and reflection are absent [65]. For such devices, electrons can be described as particles with the charge $-e$ [60]. Thus, the electron obeys Newton's law of motion [7, 42, 60]:

$$\hbar \frac{d\mathbf{k}}{dt} = -\nabla_{\mathbf{r}} E_{C0}(\mathbf{r}) = \mathbf{F}_e(\mathbf{r}, t), \quad (2.22)$$

2. Semi-Classical Transport Theory

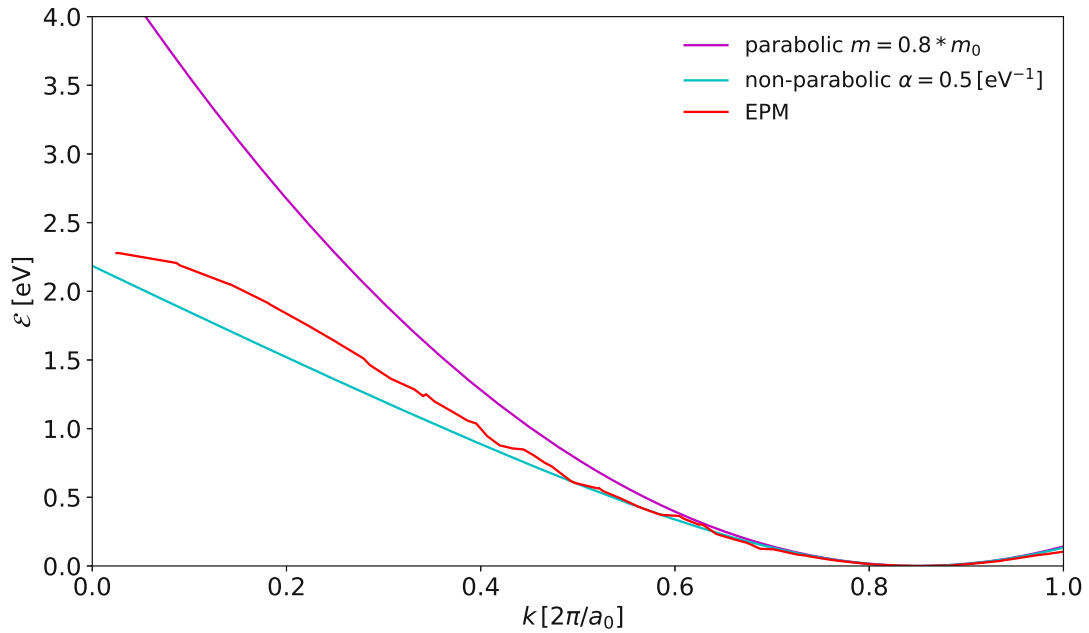


Figure 2.8.: Comparison of the dispersion relation of unstrained silicon in direction of the [100] axis with both parabolic and non-parabolic approximations, as well as EPM.

where $\hbar\mathbf{k}$ represents the momentum and \mathbf{F}_e the force applied to the electron. The particle's kinetic energy can be retrieved from the dispersion relation $\mathcal{E}(\mathbf{k})$. The particle's velocity corresponds to the group velocity [60]:

$$\mathbf{v}(\mathbf{k}) = \frac{1}{\hbar} \nabla_{\mathbf{k}} \mathcal{E}(\mathbf{k}) \quad (2.23)$$

2.3. Scattering

Carriers, characterized by Bloch waves, propagate through the ideal lattice according to the dispersion relation without any perturbation. Many effects such as lattice vibrations, impurities, and high energy particles, create a scattering potential $U_S(\mathbf{r}, t)$ and therefore cause a perturbation of the carrier state [65]. These perturbations induce an instant change of the particle's wave-vector \mathbf{k} into \mathbf{k}' , as illustrated in Fig 2.9.

The transition probability from \mathbf{k} to \mathbf{k}' can be calculated using Fermi's Golden Rule, which is derived from the time-dependent perturbation theory of the first

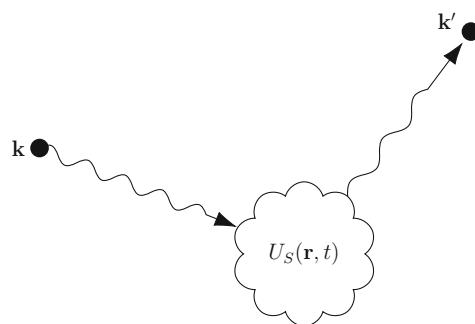


Figure 2.9.: Scattering of the wave-vector \mathbf{k} into \mathbf{k}' by the perturbation potential $U_S(\mathbf{r}, t)$

order [102]. The heart of the Golden Rule is the so-called matrix element of the perturbation potential [102]:

$$\langle \mathbf{k}' | U_S | \mathbf{k} \rangle = \int_{\Omega} \Psi_{\mathbf{k}'}^*(\mathbf{r}) U_S(\mathbf{r}) \Psi_{\mathbf{k}}(\mathbf{r}) d^3\mathbf{r}, \quad (2.24)$$

where Ψ represents the wave function of the carrier and Ω is the volume of the crystal in which the wave functions are normalized. The transition rate from state \mathbf{k} to state \mathbf{k}' is expressed by Fermi's Golden Rule [102]:

$$S(\mathbf{k}, \mathbf{k}') = \frac{2\pi}{\hbar} |\langle \mathbf{k}' | U_S | \mathbf{k} \rangle|^2 \delta(\mathcal{E}(\mathbf{k}') - \mathcal{E}(\mathbf{k}) \mp \hbar\omega), \quad (2.25)$$

where the delta-function expresses conservation of energy.

The following section should illustrate which scattering mechanisms are at play in carrier transport. A more detailed mathematical description can be found in [51, 65, 102].

2.3.1. Impurity Scattering

Carriers in a semiconductor device are usually supplied or removed through doping. In doped regions, the carrier motion is significantly disturbed by scattering due to ionized impurities, which are distributed randomly.

The electrostatic potential due to a point charge in vacuum is coulombic. However, the potential due to an impurity charge in a crystal is more or less screened depending on how many free carriers are present. Scattering due to the screened coulomb potential has been evaluated mainly with the Brooks-Herring approach [51, 102].

2.3.2. Phonon Scattering

Bloch states are the eigenstates of a perfect crystal. Therefore, electrons are not scattered by the purely periodic potential associated with the array of ions constituting the crystal. However, electrons are scattered by lattice vibrations propagating in the crystal because the periodicity of the crystal is disturbed. A small displacement of an ion in the crystal causes a small change in the crystal potential. Hence, the deviation of the crystal potential from pure periodicity may be expressed, theoretically, by the amplitude of the lattice vibrations. However, because of the difficulty of knowing the crystal potential itself, this deviation is expressed in a rather phenomenological way, such as the deformation potential method. Since the lattice vibrations can be quantized as phonons, the influence of lattice vibrations on electron motions is referred to the electron-phonon interaction [102].

This type of interaction is one of the dominant scattering processes in semiconductor devices at room temperature. Carriers in small-sized devices can acquire high energies from the high electric field applied. Therefore, scatterings based on the spontaneous emission of phonons take place even though there are only a few phonons present at low temperature [102].

There exists two types of phonon modes: acoustic and optical. For acoustic mode phonons, neighboring atoms displace in the same direction, and hence the changes in lattice spacing are produced by the strain or differential displacement. For optical phonons, neighboring atoms displace in opposite direction. Hence, the displacement produces the change in lattice spacing directly. Since the acoustic and optical phonon scatterings can be expressed by a deformation potential, which relates lattice vibrations to changes in the band energies, they are referred to as deformation potential scattering [102].

2.3.3. Carrier-Carrier Scattering

There are two types of carrier-carrier scattering processes. One is a binary scattering in which two carriers collide, and the other is a scattering due to the excitation of the collective motion of carriers, also known as plasma scattering. In this work, the first process will be described in Chapter 5.

The main difficulty in the calculation of binary scattering arises from the lack of knowledge of the distribution function, which comes into the calculation in three ways: one is through the screening factor of the interaction potential; the second is the Boltzmann scattering operator which contains a product of the distribution function and is thus non-linear. The third is by the fact that the scattering is restricted by the distribution function via Pauli's exclusion principle. Because

of screening, the collisions between carriers will be less frequent with increasing carrier density [P5, 102].

2.4. The Boltzmann Transport Equation

In classical transport theory, the Boltzmann Transport Equation (BTE) describes the kinetics of gas. In semi-classical carrier transport, this equation is used to describe the kinetics of particles with a quantum-mechanical extension [51, 95]. The BTE combines motion in \mathbf{r} and \mathbf{k} space as well as scattering processes [51]. The distribution function $f(\mathbf{r}, \mathbf{k}, t)$ represents the probability of finding a carrier with crystal momentum \mathbf{p} , at location \mathbf{r} , at time t . The BTE can be interpreted as a “bookkeeping” equation for the distribution function [65]. Thus it can be seen as a continuity equation for carriers in the six-dimensional phase-space [60], see Fig. 2.10. The following equation represents the BTE for multiple bands [49, 51, 65, 66]:

$$\left\{ \frac{\partial}{\partial t} + \mathbf{F}_n(\mathbf{r}, t) \cdot \nabla_{\mathbf{k}} + \mathbf{v}_n(\mathbf{k}) \cdot \nabla_{\mathbf{r}} \right\} f_n(\mathbf{r}, \mathbf{k}, t) = \sum_{n'} \int_{\text{BZ}} S_{n',n}(\mathbf{k}', \mathbf{k}) f_{n'}(\mathbf{r}, \mathbf{k}', t) - S_{n,n'}(\mathbf{k}, \mathbf{k}') f_n(\mathbf{r}, \mathbf{k}, t) d^3k', \quad (2.26)$$

where n represents the band index. The left hand side represents the total time derivative of the distribution function $f(\mathbf{r}, \mathbf{k}, t)$ [60]. The right hand side of the BTE describes all scattering processes into the state $(n, \mathbf{r}, \mathbf{k})$ and also out of the same state to any arbitrary state [37, 51].

The solutions to the BTE are the distribution functions for all bands, $f_n(\mathbf{r}, \mathbf{k}, t)$. With the knowledge of f_n , all quantities of interest could be calculated. However, the numerical solution of the BTE is difficult. Consequently, different approaches have been developed over the past decades to achieve a satisfying solution. The following chapter shall introduce the most commonly used approaches.

2. Semi-Classical Transport Theory

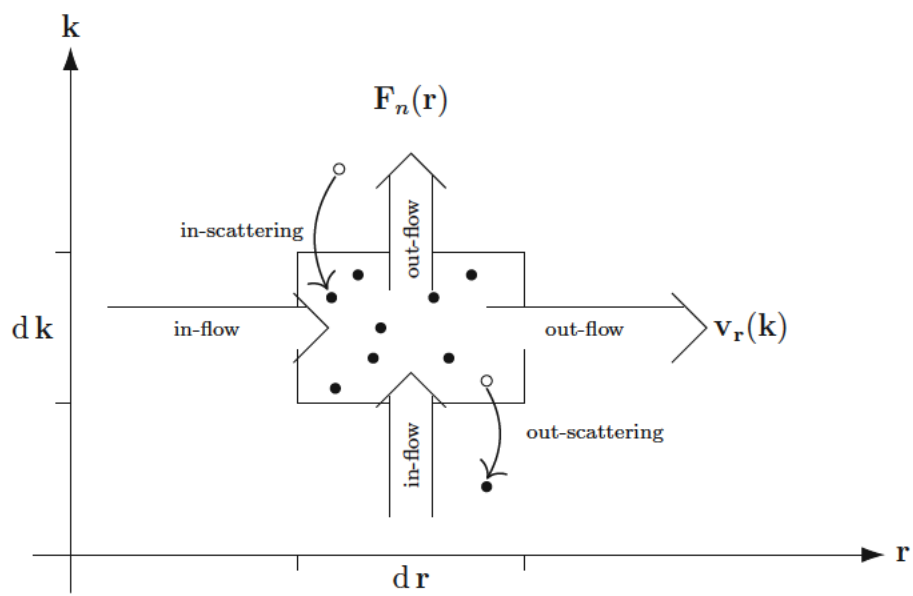


Figure 2.10.: Illustration of the continuity aspect in k and r space of the BTE

Chapter 3

Transport Modeling Approaches

The BTE is commonly used to describe the carrier transport in the semi-classical regime. Over the last century, different methods have been developed and improved to describe carrier transport based on the BTE [86]. This chapter covers a short introduction on methods based on the moments of the BTE, a deterministic approach with spherical harmonics expansion, and a stochastic approach with the Monte Carlo method. Furthermore, the advantages and the drawbacks of all these methods are discussed.

3.1. Method of Moments

This method is based on the principle, that every term of the BTE is multiplied with a weight function and subsequently integrated over the Brillouin zone (BZ). This integration leads to a saturation of the coordinates in \mathbf{k} space and leaves a set of differential equations in (\mathbf{r}, t) space. Thus, some information about the original distribution function is lost. But in many cases the equations in (\mathbf{r}, t) space are sufficient. The weight functions are often chosen as powers of \mathbf{k} with some scaling factors to achieve physically meaningful quantities. The moments of the distribution function are defined as [2, 8, 30, 98]

$$M_j = \langle \phi_j \rangle = \int \phi_j f d^3k, \quad (3.1)$$

where ϕ_j represents the weight functions, which are scalars for even orders and vectors for odd orders of \mathbf{k} . This work will only cover the basic principle of the moments method, and therefore only moments up to the third order will be considered. A more detailed description of this method can be found in [30]. The weight functions up to order three read:

3. Transport Modeling Approaches

$$\phi_0 = 1 \quad (3.2)$$

$$\phi_1 = \mathbf{p} = \hbar \mathbf{k} \quad (3.3)$$

$$\phi_2 = \mathcal{E} = \frac{\hbar^2 k^2}{2m^*} \quad (3.4)$$

$$\phi_3 = \mathbf{v}\mathcal{E} = \frac{\hbar^3 k^2 \mathbf{k}}{2(m^*)^2} \quad (3.5)$$

where \mathbf{p} is the momentum, \mathbf{k} is the wave-vector, \mathcal{E} is the kinetic energy and m^* is the effective mass.

The weight function ϕ_2 considers only a band-structure with one isotropic and parabolic valley, as described in (2.17) [30]. Applying the method of moments to the BTE for electrons the moment equation can be written as [30]:

$$\partial_t \langle \phi_j \rangle + \nabla_r \cdot \langle \mathbf{v} \phi_j \rangle + q \mathbf{E} \cdot \langle \nabla_p \phi_j \rangle = \int \phi_j \mathcal{Q} d^3k \quad \text{for even } j, \quad (3.6)$$

$$\partial_t \langle \phi_j \rangle + \nabla_r \cdot \langle \mathbf{v} \otimes \phi_j \rangle + q \mathbf{E} \cdot \langle \nabla_p \otimes \phi_j \rangle = \int \phi_j \mathcal{Q} d^3k \quad \text{for odd } j, \quad (3.7)$$

where \mathcal{Q} represents the scattering integral of the BTE, which is the right hand side of (2.26).

Equations (3.6) and (3.7) contain gradients of the weight functions, which can be calculated as [30]:

$$\nabla_p \phi_0 = 0 \quad (3.8)$$

$$\nabla_p \otimes \phi_1 = \mathbb{1} \quad (3.9)$$

$$\nabla_p \phi_2 = \mathbf{v} \quad (3.10)$$

$$\nabla_p \otimes \phi_3 = \frac{\mathcal{E}}{m^*} \mathbb{1} + \mathbf{v} \otimes \mathbf{v} \quad (3.11)$$

Here, $\mathbb{1}$ is the unit matrix in three dimensions. The integrate over the scattering integral, on the other hand, can be modeled with the relaxation time approximation [30, 72]:

$$\int \phi_j \mathcal{Q} d^3k \approx -\frac{\langle \phi_j \rangle - \langle \phi_j \rangle_0}{\tau_{\phi_j}}, \quad (3.12)$$

where the index 0 represents an average over the equilibrium distribution function. This approach assumes, that the moment $\langle \phi_j \rangle$ decays exponentially towards its equilibrium value with the time constant τ_{ϕ_j} after the field is switched off [65]. Applying these approximations to the equations of moments (3.6) and (3.7), a set of equations can be obtained [30]:

$$\phi_0 : \quad \partial_t \langle 1 \rangle + \nabla \cdot \langle \mathbf{v} \rangle = 0 \quad (3.13)$$

$$\phi_1 : \quad \nabla \cdot \langle \mathbf{v} \otimes \mathbf{p} \rangle + q\mathbf{E} \langle \mathbb{1} \rangle = -\frac{\langle \mathbf{p} \rangle}{\tau_m} \quad (3.14)$$

$$\phi_2 : \quad \partial_t \langle \mathcal{E} \rangle + \nabla \cdot \langle \mathbf{v} \mathcal{E} \rangle + q\mathbf{E} \langle \mathbf{v} \rangle = -\frac{\langle \mathcal{E} \rangle - \langle \mathcal{E} \rangle_0}{\tau_{\mathcal{E}}} \quad (3.15)$$

$$\phi_3 : \quad \nabla \cdot \langle \mathbf{v} \otimes \mathbf{v} \mathcal{E} \rangle + q\mathbf{E} \left\langle \frac{\mathcal{E}}{m^*} \mathbb{1} + \mathbf{v} \otimes \mathbf{v} \right\rangle = -\frac{\langle \mathbf{v} \mathcal{E} \rangle}{\tau_s}, \quad (3.16)$$

where τ_m , $\tau_{\mathcal{E}}$ and τ_s are the relaxation times for momentum, energy and energy flux, respectively. The equations above contain statistical averages of a symmetric tensor of the form $\langle \mathbf{v} \otimes \mathbf{v} \rangle$. These averages can be evaluated with the *diffusion approximation* [90] which leads to a diagonal tensors with all diagonal elements being equal [30]:

$$\langle \mathbf{v} \otimes \mathbf{v} \rangle = \frac{\langle v^2 \rangle}{3} \mathbb{1}, \quad (3.17)$$

$$\langle \mathbf{v} \otimes \mathbf{v} \mathcal{E} \rangle = \frac{\langle \mathcal{E} v^2 \rangle}{3} \mathbb{1}. \quad (3.18)$$

The statistical averages in the equations (3.13), (3.14), and (3.15), are commonly expressed by the electron concentration n , the electron temperature T_n and the electrical current density \mathbf{J} , respectively:

$$\phi_0 : \langle 1 \rangle = n \quad (3.19)$$

$$\phi_1 : \langle \mathbf{v} \rangle = \frac{\mathbf{J}}{nq} \quad (3.20)$$

$$\phi_2 : \langle \mathcal{E} \rangle = \frac{3}{2} k_B n T_n \quad (3.21)$$

$$\phi_3 : \langle \mathbf{v} \mathcal{E} \rangle = \mathbf{S}_n, \quad (3.22)$$

The averages of ϕ_0 and ϕ_2 represent densities, whereas ϕ_1 and ϕ_3 represent fluxes. With these expressions the equations of moments up to the third order can be written in the final form [30]:

3. Transport Modeling Approaches

$$\phi_0 : \quad \partial_t n - \frac{1}{q} \nabla \cdot \mathbf{J}_n = 0 \quad (3.23)$$

$$\phi_1 : \quad \mathbf{J}_n = \frac{q \tau_m}{m^*} (\nabla (k_B n T_n) + q \mathbf{E} n) \quad (3.24)$$

$$\phi_2 : \quad \frac{3}{2} k_B \partial_t (n T_n) + \nabla \cdot \mathbf{S}_n - \mathbf{E} \cdot \mathbf{J}_n = \frac{3}{2} k_B n \frac{T_n - T_L}{\tau_\varepsilon} \quad (3.25)$$

$$\phi_3 : \quad \mathbf{S}_n = -\tau_S \left(\frac{1}{3} \nabla \langle \phi_4 \rangle + \frac{5 q k_B}{2 m^*} \mathbf{E} n T_n \right) \quad (3.26)$$

One characteristic of the method of moments is that the transport equation of the order i contains the moment of order $i + 1$. This highest moment has to be approximated, which is commonly referred to as the closure of the hierarchy of moment equations [30].

3.1.1. The Drift Diffusion Model

The drift-diffusion equation is obtained from the equations of moments by considering only the two moments (3.23) and (3.24). The term

$$\frac{q \tau_m}{m^*} = \mu_n \quad (3.27)$$

represents the electron mobility. The assumption that the carriers have the same temperature as the lattice ($T_n = T_L$), also known as thermal equilibrium approximation [3, 70], gives the closure relation

$$\langle \phi_2 \rangle = \frac{3}{2} k_B n T_L, \quad (3.28)$$

With this relation the drift-diffusion transport model is obtained [30, 33, 82, 91, 93]:

$$\nabla \cdot \mathbf{J}_n = q \partial_t n \quad (3.29)$$

$$\mathbf{J}_n = \mu_n k_B \left(\nabla (n T_L) + \frac{q}{k_B} \mathbf{E} n \right) \quad (3.30)$$

This model considers local quantities only. Therefore, it neglects non-local transport effects which occur, for example, in a sudden variation of the electric field. In order to deal with non-equilibrium effects, field-dependent mobility models were introduced [30].

More accurate macroscopic transport models include the average carrier energy. The energy transport model and the hydrodynamic model are derived from the first four moments of the BTE [30, 87].

3.2. Spherical harmonic expansion

Spherical harmonics are mathematical functions defined on the surface of the unit sphere. The spherical harmonics $Y^{l,m}$ form an orthogonal basis [6, 26, 38–40]:

$$\int_{\theta=0}^{\pi} \int_{\varphi=0}^{2\pi} Y^{l,m} Y^{l',m'} \sin(\theta) d\varphi d\theta = \delta_{l,l'} \delta_{m,m'}, \quad (3.31)$$

where $(\delta_{a,b})$ is the *Kronecker delta*.

A deterministic approach to solve the BTE relies on the expansion of the distribution function $f(\mathbf{r}, \mathbf{k}, t)$ into spherical harmonics [22, 24, 25, 39, 50, 84, 87]:

$$f(\mathbf{r}, \mathbf{k}, t) = \sum_{l=0}^{\infty} \sum_{m=-l}^l f_{l,m}(\mathbf{r}, \mathcal{E}, t) Y^{l,m}(\theta, \varphi) \quad (3.32)$$

where the wave vector \mathbf{k} in the distribution function is transformed into spherical coordinates \mathcal{E} , θ and φ on equi-energy surfaces.

The elliptical valleys are transformed into spherical ones by the Herring-Vogt transformation [23, 86]. The spherical coordinates of the wave-vector (k, θ, φ) can be mapped to spherical coordinates of energy $(\mathcal{E}, \theta, \varphi)$. This direct one-to-one mapping can be achieved with the non-parabolic band-structure approximation [50, 58, 86], mentioned in Section 2.1.3. Therefore, the seven-dimensional space $(\mathbf{r}, \mathbf{k}, t)$ of the BTE can be reduced to a five-dimensional space $(\mathbf{r}, \mathcal{E}, t)$. This reduces the computational expenses for the deterministic solution.

Recently, many improvements have been made in the field of the SHE method to solve the BTE. Full-band effects have been considered as well as quantum mechanical effects. Further, the treatment of three-dimensional devices, as well as carrier-carrier scattering, is possible [6, 40, 48, 106].

A drawback of this method is that it relies on the spherical symmetry of the analytical band-structure and therefore is unable to account for the fully anisotropic numerical structure. Considering only some full-band effects, this method is not very accurate in the treatment of high-energy carriers.

3.3. Monte Carlo Method

The Monte Carlo method is a stochastic approach to integrate functions in general and to solve integral equations in particular [21, 34, 43, 51, 59, 61].

The Monte Carlo method for carrier transport in semiconductors calculates trajectories of carriers in \mathbf{r} - and \mathbf{k} -space under the influence of acceleration by the electric field and of scattering mechanisms. The duration of free-flight, the type of the scattering mechanism, and the final state after scattering are calculated using random numbers. With a sufficiently large number of trajectories, the averages of the attributes can be calculated [18, 60].

One drawback of stochastic simulations is that the statistical error of the estimator is declining with the factor $1/\sqrt{N}$, where N is the number of random events. In other words, if one wants to reduce the error by a factor N , the calculation cost will increase by N^2 .

An advantage of the Monte Carlo method is that individual trajectories of carriers are much simpler to calculate than solving the BTE with a deterministic approach. Furthermore, the Monte Carlo method allows one to use full-band structures to estimate the carrier distribution function $f(\mathbf{r}, \mathbf{k}, t)$. Because of these advantages the Monte Carlo method is used in many cases as a reference method for simpler transport models [60].

3.3.1. Monte Carlo Integration

As mentioned above, the Monte Carlo method is in general a stochastic method to solve integrals. A integral over a function $\varphi(x)$,

$$I = \int_a^b \varphi(x) dx \quad (3.33)$$

can be expressed as an expectation value of some random variable. For this purpose, the function $\varphi(x)$ is factorized:

$$\varphi(x) = f(x) p(x), \quad I = \int_a^b f(x) p(x) dx, \quad (3.34)$$

where $p(x)$ is a density function of the Monte Carlo samples satisfying

$$p(x) \geq 0, \quad \int_a^b p(x) dx = 1. \quad (3.35)$$

The integral in (3.34) represents an expectation value $I = E\{f\}$. The Monte Carlo method estimates the expectation value by a sample mean:

$$I \approx \frac{1}{N} \sum_{i=1}^N f(x_i), \quad (3.36)$$

where N is the number of sampling points [61].

3.3.2. Generation of Random Numbers

Monte Carlo methods rely on uniformly distributed random numbers. Since the generation of random numbers on computers is difficult, pseudo-random numbers are used [9, 47, 75]. These pseudo-random numbers have one big advantage for testing: if the same seed is used every time, the sequence is reproducible [P3, 78].

Inversion Method

The uniformly distributed pseudo-random number r , used in this method, has the property [51]

$$0 \leq r < 1. \quad (3.37)$$

For the generation of a random number with a given probability density $p(x)$, its cumulative distribution function is needed [9, 46, 51, 52]:

$$P(x) = \int_{-\infty}^x p(x') dx', \quad (3.38)$$

with

$$P(-\infty) = 0, \quad 0 \leq P(x) \leq 1, \quad P(\infty) = 1. \quad (3.39)$$

A $p(x)$ distributed random number x can be calculated through the inverse of the cumulative distribution function

$$x = P^{-1}(r), \quad (3.40)$$

where r is a pseudo-random number of type (3.37). However, this method is only applicable if the analytic integral of the function $p(x)$ is possible to evaluate. Otherwise, different approaches to generate $p(x)$ distributed pseudo-random numbers are needed.

3. Transport Modeling Approaches

Rejection Method

For the generation of a random number with a given probability density $p(x)$, where $p(x)$ is bounded in the finite interval (x_{\min}, x_{\max}) , a uniform distributed random number r with the properties

$$0 \leq r < \max[p(x)] \quad (3.41)$$

is chosen for the sample point x . If the random number r lies in the range of

$$0 \leq r < p(x) \quad (3.42)$$

it gets accepted. Else the random number gets rejected [12, 46]. The accepted random number is $p(x)$ distributed. This method is always applicable, with any bounded function $p(x)$ in a finite interval. However, if the function $p(x)$ is heavily peaked, many rejections will occur and the computational expenses will become high.

Combined Method

To keep the rejection rate small, the function which represents the maximum of the probability density, $\max[p(x)]$, could be replaced by an analytically integrate-able function $g(x)$. In the interval (x_{\min}, x_{\max}) , $g(x)$ must be always greater than $p(x)$.

Here, a random number r can be directly obtained from $g(x)$ with the inversion method. This random number r can then be applied to the rejection method, where the number of rejections can be significantly reduced by finding a suitable function $g(x)$. In the case, that $g(x)$ is chosen as a constant, this method will result in the rejection method, described above.

3.3.3. Duration of the Free Flight

The solution of the BTE for carrier transport can be estimated with the Monte Carlo method. One random parameter in this method is the time of the free-flight of a carrier. This parameter depends on the total scattering rate $\lambda(t)$. The probability for the scattering of a carrier in an interval Δt at a time t is $\lambda(t) \Delta t$, where $\lambda(t)$ represents the \mathbf{r} and \mathbf{k} dependent scattering rate at the time t :

$$\lambda(t) = \lambda(\mathbf{k}(t), \mathbf{r}(t)) \quad (3.43)$$

With the assumption, that the carrier scatters at $t = 0$, the cumulative distribution function $P(t)$ can be calculated. In this case, no other scattering process takes

place until the time t . Thus, the carrier is in free-flight for the duration of t [60]:

$$P(t) = \begin{cases} 1 - e^{-\int_0^t \lambda(\tau) d\tau} & : t \geq 0 \\ 0 & : t < 0 \end{cases}. \quad (3.44)$$

Using the inversion method, the duration of the free-flight t_f can be calculated from the equation $P(t_f) = r$ as

$$\int_0^{t_f} \lambda(\mathbf{k}(t), \mathbf{r}(t)) dt = -\ln(1 - r), \quad (3.45)$$

where r represents a uniform distributed random number [46]. The integration takes place along the trajectory of the carrier $(\mathbf{k}(t), \mathbf{r}(t))$, which can be acquired by integrating the equations of motion (2.22) and (2.23).

The full-band simulations use constant total scattering rates Γ_{\max} , as shown in Fig. 3.1 [110]. In case Γ is constant, the duration of the free-flight is [P3]:

$$t_f = -\frac{1}{\Gamma} \ln(1 - r). \quad (3.46)$$

Because Γ_{\max} must be larger than the sum of the scattering rates of all physical scattering processes $\lambda(t)$, the self-scattering is more likely to occur in areas where $\lambda(t)$ is significant smaller than Γ_{\max} . For this reason $\lambda(t)$ can be approximated by local, picewise constant values $\Gamma_{\max}(t)$. Since these local values are smaller than the global Γ_{\max} , self-scattering is reduced. The duration of a collision-less free-flight is given by [51]

$$\Gamma_{\max}(t_f - t_j) = -\ln(1 - r) - \sum_{k=1}^j \Gamma_{\max}(t_k - t_{k-1}) \quad \text{for} \quad t_j < t_f < t_{j+1}, \quad (3.47)$$

where t_j is the time at which the particle passes a change in $\Gamma_{\max}(t)$ during the free-flight t_f .

3.3.4. Selection of the Scattering Process

After the free-flight, another uniformly distributed random number,

$$0 \leq r < \Gamma_{\max}, \quad (3.48)$$

3. Transport Modeling Approaches

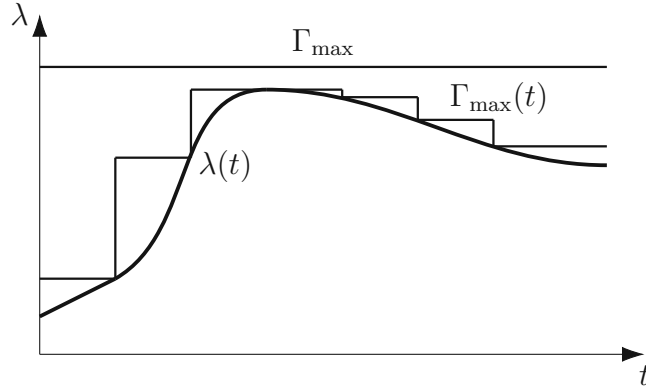


Figure 3.1.: The scattering rate $\lambda(t)$, the piecewise constant scattering rate $\Gamma(t)$ and the global maximum Γ_{\max} .

is used to select the scattering process, as described in [51, 60]. The actual scattering rates from all the implemented processes must be smaller than or equal to the constant total scattering rate Γ_{\max} ,

$$\Gamma_{\max} \geq \sum_{i=1}^N \lambda_i(t_f), \quad (3.49)$$

where λ_i is the rate of the i^{th} scattering process. The scattering process m is chosen when

$$\sum_{i=1}^{m-1} \lambda_i(t_f) \leq r < \sum_{i=1}^m \lambda_i(t_f). \quad (3.50)$$

If the random number is in the range of

$$\Gamma_{\max} \geq r > \sum_{i=1}^N \lambda_i(t_f), \quad (3.51)$$

self scattering occurs [60].

3.3.5. Generation of an Equilibrium Distribution

Equilibrium distributions at given temperatures are needed for injecting particles in a Monte Carlo simulation. This section shows three different methods how an equilibrium distribution can be sampled.

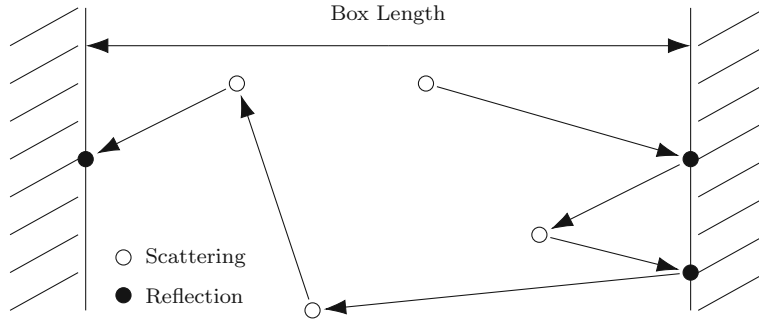


Figure 3.2.: Sampling using the box method.

Box Method

A single-particle Monte Carlo simulation is performed in a box with constant length. To obtain an equilibrium distribution, the electric field is set to zero. Every time the carrier hits a boundary and gets reflected, its state is added to the sample, as illustrated in Fig. 3.2. The distribution of the generated sample represents a velocity weighted Maxwellian distribution [65]

$$f_v(\mathbf{k}) = |v_{\perp}(\mathbf{k})| f(\mathbf{k}), \quad (3.52)$$

where $|v_{\perp}(\mathbf{k})|$ is the velocity component perpendicular to the boundary.

In the statistical average of an attribute $A(\mathbf{k})$ the weighting factor $|v_{\perp}(\mathbf{k})|^{-1}$ is obtained by replacing $f(\mathbf{k})$ by $f_v(\mathbf{k}) |v_{\perp}(\mathbf{k})|^{-1}$ [P3]:

$$\langle A \rangle_{\text{Box}} = \frac{\int f(\mathbf{k}) A(\mathbf{k}) d^3k}{\int f(\mathbf{k}) d^3k} = \frac{\int f_v(\mathbf{k}) |v_{\perp}(\mathbf{k})|^{-1} A(\mathbf{k}) d^3k}{\int f_v(\mathbf{k}) |v_{\perp}(\mathbf{k})|^{-1} d^3k} \approx \frac{\sum_{i=1}^N A(\mathbf{k}_i) |v_{\perp}(\mathbf{k}_i)|^{-1}}{\sum_{i=1}^N |v_{\perp}(\mathbf{k}_i)|^{-1}}, \quad (3.53)$$

where N represents the number of sampled states.

Bulk Method

A single-particle Monte Carlo simulation is performed for a uniform semiconductor at zero field. The equilibrium distribution is obtained by sampling the particle state before a scattering event occurs (*before scattering method*). With this method the distribution of the obtained \mathbf{k} -values is a Maxwellian distribution $f(\mathbf{k})$ weighted with the scattering rate $\Gamma(\mathbf{k})$ [46, 60].

$$f_{\Gamma}(\mathbf{k}) = \Gamma(\mathbf{k}) f(\mathbf{k}), \quad (3.54)$$

3. Transport Modeling Approaches

When the mean value of an attribute $A(\mathbf{k})$ is calculated, the weighting factor Γ^{-1} has to be taken into account:

$$\langle A \rangle_{\text{Bulk}} = \frac{\int f(\mathbf{k}) A(\mathbf{k}) d^3k}{\int f(\mathbf{k}) d^3k} = \frac{\int f_{\Gamma}(\mathbf{k}) \Gamma(\mathbf{k})^{-1} A(\mathbf{k}) d^3k}{\int f_{\Gamma}(\mathbf{k}) \Gamma(\mathbf{k})^{-1} d^3k} \approx \frac{\sum_{i=1}^N A(\mathbf{k}_i) \Gamma(\mathbf{k}_i)^{-1}}{\sum_{i=1}^N \Gamma(\mathbf{k}_i)^{-1}}. \quad (3.55)$$

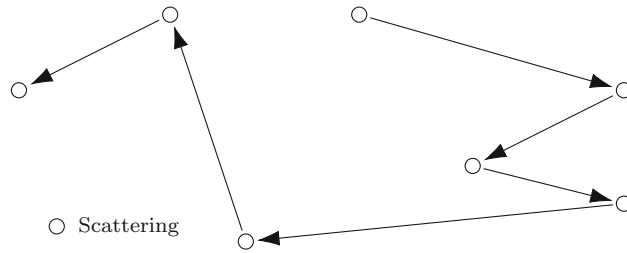


Figure 3.3.: Sampling using the before-scattering method.

Constant Time Sampling Method

Again, a single particle Monte Carlo simulation is performed for a uniform semiconductor at zero field. Now, the trajectory is sampled at constant time intervals. In this case the equilibrium distribution is directly obtained [46] and the average can be calculated from the sampled states without any additional weighting factors.

$$\langle A \rangle_{\text{Time}} = \frac{\int f(\mathbf{k}) A(\mathbf{k}) d^3k}{\int f(\mathbf{k}) d^3k} \approx \frac{1}{N} \sum_{i=1}^N A(\mathbf{k}_i). \quad (3.56)$$

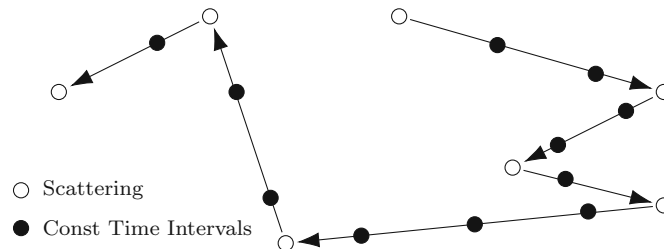


Figure 3.4.: Constant time sampling method.

3.3.6. Calculation of Equilibrium Averages

With the numerical representation of the dispersion relation in the first Brillouin zone, averages such as mean kinetic energy or injection velocity at thermal equilibrium can be calculated by numerical integration over the equilibrium distribution [P3].

This method is faster than Monte Carlo integration. In contrast to the Monte Carlo methods, this method can be only applied in thermal equilibrium, where the distribution function is known to be a Maxwell-Boltzmann or a Fermi-Dirac distribution. Here we assume a Maxwell-Boltzmann (MB) distribution. The average of an attribute A is calculated like [74]

$$\langle A \rangle = \frac{\sum_n \int_{\text{BZ}} A_n(\mathbf{k}) e^{-\beta \mathcal{E}_n(\mathbf{k})} d^3k}{\sum_n \int_{\text{BZ}} e^{-\beta \mathcal{E}_n(\mathbf{k})} d^3k}, \quad (3.57)$$

where BZ denotes the whole Brillouin zone, n is the band index, $\beta = (k_{\text{B}}T)^{-1}$ with the Boltzmann constant k_{B} and the Temperature T . In statistical mechanics a parameter Z called partition function is introduced [74].

$$Z = \sum_n \int_{\text{BZ}} e^{-\beta \mathcal{E}_n(\mathbf{k})} d^3k \quad (3.58)$$

With the partition function (3.58) the statistical average (3.57) becomes:

$$\langle A \rangle = \frac{1}{Z} \sum_n \int_{\text{BZ}} A_n(\mathbf{k}) e^{-\beta \mathcal{E}_n(\mathbf{k})} d^3k. \quad (3.59)$$

For a detailed description of the numerical integration see Appendix A.1 or [P3].

3.3.7. Estimation of Non-Equilibrium Averages

With the Monte Carlo method, average values of attributes of interest can be estimated, such as electron density, carrier velocity, energy and many more. For the estimation of local attributes using the single particle method, there is commonly one method used: the before scattering method. This work presents a second method to estimate local attributes based on the box-sampling method. Further, the estimation of global attributes, for example, the current through a contact is shown.

3. Transport Modeling Approaches

Before scattering method

The *before scattering* method is obtaining the values of the attributes of interest before a scattering event takes place. These values are weighted with the total scattering rate $\Gamma(\mathbf{k})$, as shown in (3.55) [51, 60]:

In a spatial discretization every grid point P_j in a device has a volume V_j assigned. Inside this Volume V_j , the closest grid point is P_j , where j is an index for every grid point in \mathbf{r} space. This kind of discretization volume is also known as *Voronoi* volume. The averages of the local attributes can be built for every discretization volume V_j separately in the manner of [88]:

$$\langle A(\mathbf{k}) \rangle_j \approx \frac{\sum_{\mathbf{r}_i \in V_j} A(\mathbf{k}_i) \Gamma(\mathbf{k}_i)^{-1}}{\sum_{\mathbf{r}_i \in V_j} \Gamma(\mathbf{k}_i)^{-1}}. \quad (3.60)$$

Here, the summation runs over the before scattering states $(\mathbf{k}_i, \mathbf{r}_i)$, where the scattering takes place inside the Volume V_j [60].

One drawback of this method is, that if no scattering event happens while a particle traverses a discretization volume, no contributions are made to the sum in (3.60).

Boundary method

The boundary method gathers statistical information when a particle crosses a boundary from one Voronoi volume to another. Therefore, the \mathbf{k} -values are weighted with the velocity component of the particle perpendicular to the boundary $|v_\perp(\mathbf{k})|$ [65]. In the manner of the box method, the mean values of the local attributes can be calculated like:

$$\langle A(\mathbf{k}) \rangle_j \approx \frac{\sum_{\mathbf{r}_n \in e_j} A(\mathbf{k}_n) |v_\perp(\mathbf{k}_n)|^{-1}}{\sum_{\mathbf{r}_n \in e_j} |v_\perp(\mathbf{k}_n)|^{-1}}, \quad (3.61)$$

where \mathbf{r}_n is the point on the j -th edge, where one particle is crossing the n -th time the edge e_j between two Voronoi volumes.

The benefit of this method is, that also in regimes where there is barely no scattering, sampling values can be obtained. Therefore, statistical averages of local attributes even in areas with ballistic transport can be estimated.

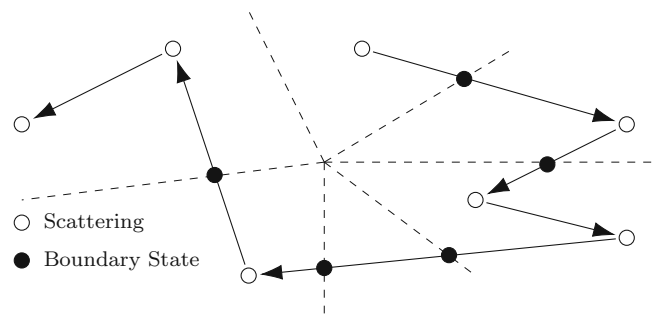


Figure 3.5.: Boundary method sampling in a device. The dashed lines are the boundaries between the Voronoi volumes.

Combination of methods

The before-scattering method and the boundary method can be combined. This combination of methods gives a smaller statistical error than the ones of each method individually.

To investigate this combined averaging method, a silicon $n^+n^-n^+$ diode with abrupt junctions was chosen. The doping levels are 10^{19}cm^{-3} and 10^{15}cm^{-3} , respectively. Fig. 3.6 shows the conduction band edge and the electron density for an applied voltage of 2 V.

Fig. 3.7 compares the different averaging methods in the $n^+n^-n^+$ diode in the area of the n^+n^- junction at 200 nm. The simulation with constant grid size shows a nearly constant factor between *before-scattering* and *boundary* method. The diode with variable grid size shows a clear dependence of the number of entries of the *before-scattering* method on the grid size. At $x > 250$ nm the grid size is becoming so big, that the *before-scattering* method has an advantage over the *boundary* method. Nevertheless, the combination of the two methods always gathers more entries than one method alone.

3. Transport Modeling Approaches

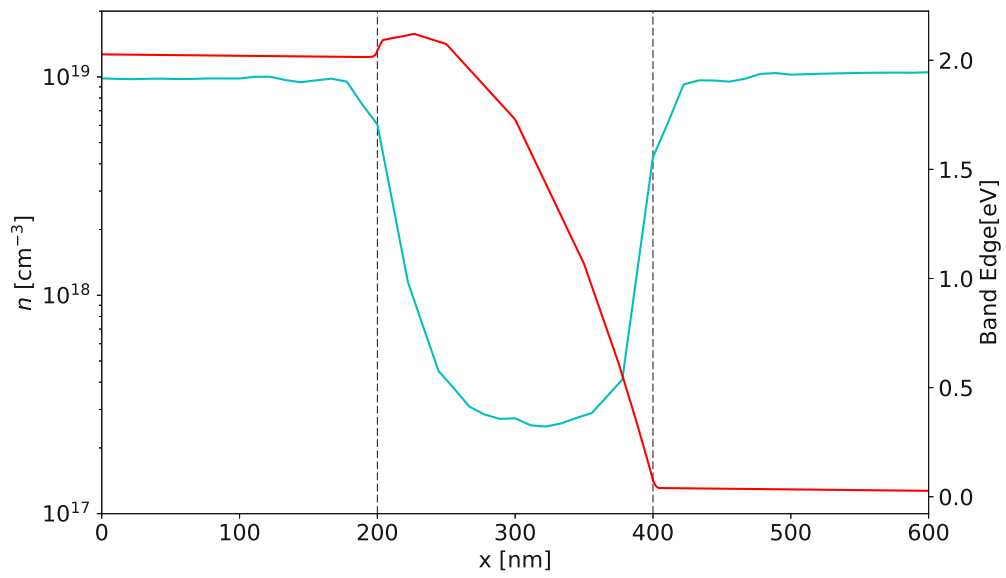
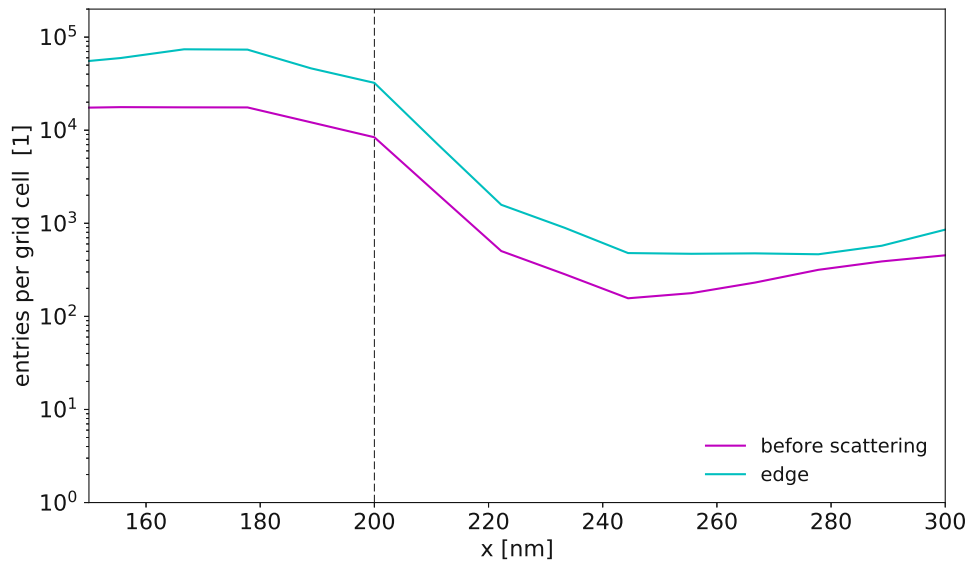
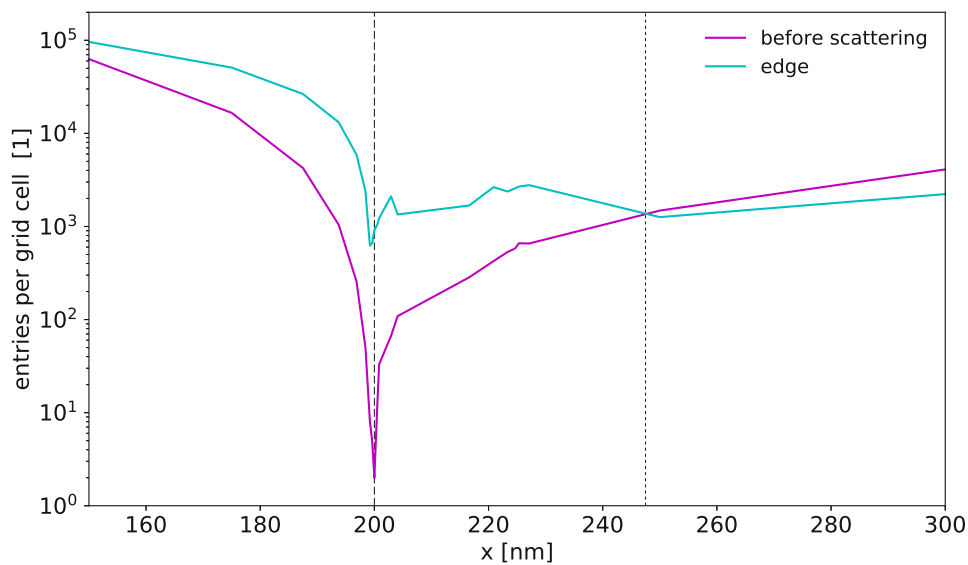


Figure 3.6.: Conduction band edge (red) and the electron density (blue) in an $n^+n^-n^+$ diode with abrupt junctions.



(a) Constant grid-cell size. The number of entries on the edge is always higher than in the Voronoi volume (before-scattering method)



(b) Variable grid-cell size. For $x < 250$ nm, the number of entries on the edges is higher. For $x > 250$ nm, the number of entries in the Voronoi volumes is higher. This results from different grid-cell sizes.

Figure 3.7.: Comparison of two different averaging methods in an silicon $n^+n^-n^+$ diode with constant and variable grid size. Both images show the region around the n^+n^- junction at 200 nm.

3. Transport Modeling Approaches

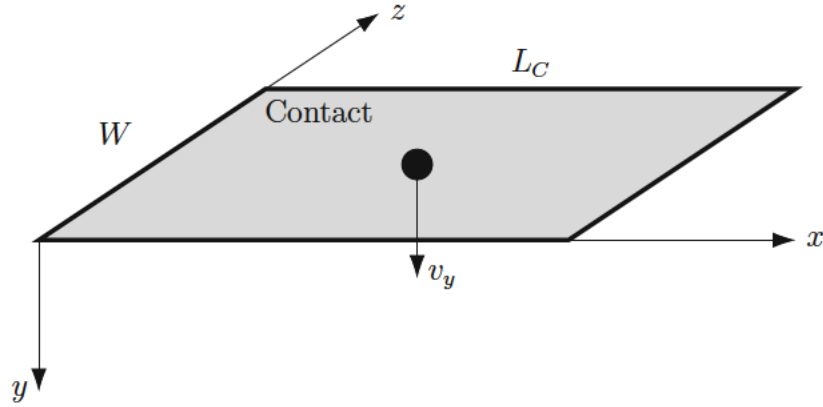


Figure 3.8.: Sketch of a device contact in the x - z plane.

3.3.8. Current Estimation

The Monte Carlo method is capable of estimating global attributes as well as local ones. The current is chosen here exemplarily for a global attribute to estimate. The following calculations of the current in a two dimensional device can be found in [P3]. The definition of the current density reads:

$$\mathbf{J} = \frac{2q}{(2\pi)^3} \int_{\text{BZ}} \mathbf{v}(\mathbf{k}) f(\mathbf{k}, \mathbf{r}) d^3k, \quad (3.62)$$

where $f(\mathbf{k}, \mathbf{r})$ is the unknown solution of the BTE and q is the particle charge. The current through a contact in a two-dimensional device can be calculated as

$$I = \int_{\text{contact}} \mathbf{J} \cdot d\mathbf{A} = \int_{z=0}^W \int_{x=0}^{L_C} \mathbf{J} \cdot \mathbf{e}_y dx dz = W \int_{x=0}^{L_C} J_y(x, 0) dx \quad (3.63)$$

$$= \frac{q}{4\pi^3} W \int_{x=0}^{L_C} \int_{\text{BZ}} v_y(\mathbf{k}) f(\mathbf{k}, x, 0) d^3k dx, \quad (3.64)$$

where $\int d\mathbf{A} = \int \mathbf{e}_y W dx$ represents the integration over the contact area and W is the width of the contact, as shown in Figure 3.8. Introducing the velocity weighted distribution of the contact [65],

$$f_v(\mathbf{k}, \mathbf{r}) = |v_y(\mathbf{k})| f(\mathbf{k}, \mathbf{r}), \quad (3.65)$$

the current is reformulated as

$$I = \frac{q}{4\pi^3} W \int_{x=0}^{L_C} \int_{\text{BZ}} \text{sign}(v_y(\mathbf{k})) f_v(\mathbf{k}, x, 0) d^3k dx, \quad (3.66)$$

where v_y is the velocity component normal to the contact. To estimate this integral with the Monte Carlo method (Section 3.3.1) the distribution function $f_v(\mathbf{k}, x, 0)$ needs to be normalized [61]. We assume that the doping concentration under the contact is constant:

$$N_D(x, y = 0) = N_{\text{surf}}. \quad (3.67)$$

This results in a constant electron concentration under the contact ($n_{\text{surf}} = N_{\text{surf}}$) and, therefore, the boundary distribution is independent of the x -coordinate:

$$f_v(\mathbf{k}, x, 0) = f_v^{\text{surf}}(\mathbf{k}) \quad (3.68)$$

The electron concentration in general is defined as

$$n(\mathbf{r}) = \frac{1}{4\pi^3} \int_{\text{BZ}} f(\mathbf{k}, \mathbf{r}) d^3k = \frac{1}{4\pi^3} \int_{\text{BZ}} \frac{1}{|v_y|} f_v(\mathbf{k}, \mathbf{r}) d^3k. \quad (3.69)$$

With the definition of the normalized distribution function

$$p_v^{\text{surf}}(\mathbf{k}) = \frac{f_v^{\text{surf}}(\mathbf{k})}{\mathcal{C}}, \quad (3.70)$$

equations (3.66) and (3.69) become

$$I = \frac{q}{4\pi^3} W L_C \mathcal{C} \int_{\text{BZ}} \text{sign}(v_y(\mathbf{k})) p_v^{\text{surf}}(\mathbf{k}) d^3k, \quad (3.71)$$

$$n_{\text{surf}} = \frac{\mathcal{C}}{4\pi^3} \int_{\text{BZ}} \frac{1}{|v_y|} p_v^{\text{surf}}(\mathbf{k}) d^3k. \quad (3.72)$$

The normalization constant \mathcal{C} can be eliminated from this system of equations:

$$I = q W L_C n_{\text{surf}} \frac{\int_{\text{BZ}} \text{sign}(v_y) p_{\text{surf}}(\mathbf{k}) d^3k}{\int_{\text{BZ}} \frac{1}{|v_y|} p_{\text{surf}}(\mathbf{k}) d^3k}. \quad (3.73)$$

The integrals in the numerator and denominator represent expectation values, that can be estimated by sample means, see Section 3.3.1.

$$I = q W L_C N_{\text{surf}} \frac{\sum_{i=1}^N \text{sign}(v_y)}{\sum_{i=1}^N \frac{1}{|v_y|}} = q W L_C n_{\text{surf}} \frac{N_{\text{in}} - N_{\text{out}}}{\sum_{i=1}^N \frac{1}{|v_y|}}. \quad (3.74)$$

3. Transport Modeling Approaches

Here, $N = N_{\text{in}} + N_{\text{out}}$, where N_{in} is the number of injected particles ($\text{sign}(v_y) = 1$), N_{out} is the number of absorbed particles ($\text{sign}(v_y) = -1$), N_{surf} is the constant doping concentration under the contact and $W L_C$ is the area of the contact as shown in Figure 3.8.

To estimate the error of the contact current, an estimator ν_i is introduced:

$$\nu_i = \begin{cases} -1 & : \text{particle gets absorbed but not injected at this contact} \\ 0 & : \text{particle gets injected and absorbed at this contact} \\ +1 & : \text{particle gets injected but not absorbed at this contact} \end{cases}, \quad (3.75)$$

where the index i corresponds to one particular trajectory. The current is proportional to the sample mean of the ν_i , and the statistical error of the current is proportional to the sample variance:

$$s_\nu^2 = \frac{1}{N-1} \left(\sum_{i=1}^N \nu_i^2 - N \bar{\nu}^2 \right) \quad (3.76)$$

The standard deviation of the current is estimated as

$$s_I = \frac{s_\nu}{\sqrt{N}} \Rightarrow s_{\text{rel}} = \frac{s_I}{I}. \quad (3.77)$$

The relative standard deviation s_{rel} can be used as a measure for the statistical error. These equations are applicable because the starting points of all trajectories are statistically independent, and so are the random numbers ν_i .

Chapter 4

Backward Monte Carlo Method

The backward MC method (BMC) was introduced at the end of the 1980s [45, 73]. These early algorithms turned out to be numerically unstable, as the carrier energy tends to grow indefinitely on a trajectory that is followed back in time [P4]. A numerically stable algorithm was proposed in 2003 [62]. Since the backward transition rates are chosen to obey the principle of detailed balance, a runaway of the carrier energy along a backward trajectory is avoided. From a practical point of view, this means that the scattering rates of the forward method can be used in the backward method as well [62].

The principle of the BMC method for the solution of a boundary value problem is to choose a set of states in phase space and trace trajectories from these states back in time until a contact is reached. The value of the given distribution function (DF) at the contact determines the statistical weight of the backward trajectory and consequently its contribution to the estimator of interest [P4].

This method enables the calculation of a current, that is controlled by an energy barrier. The current through a device is typically determined by the states at the top of the barrier, see Fig. 4.1. If the barrier is high, a forward trajectory is very unlikely to reach the top of the barrier, whereas in the backward method only these unlikely states are considered, and no computation time is wasted with the vast majority of trajectories that do not overcome the barrier [P4].

It is also possible to combine the backward and the forward MC method. Once a backward trajectory with an initial state $(\mathbf{v}_0, \mathbf{r}_0)$ is calculated, and the statistical weight of that state is determined, a forward trajectory can be started from the very same state (Fig. 4.5). The mean values of interest are then calculated from a set of forward trajectories in the usual manner [P3, P4].

4. Backward Monte Carlo Method

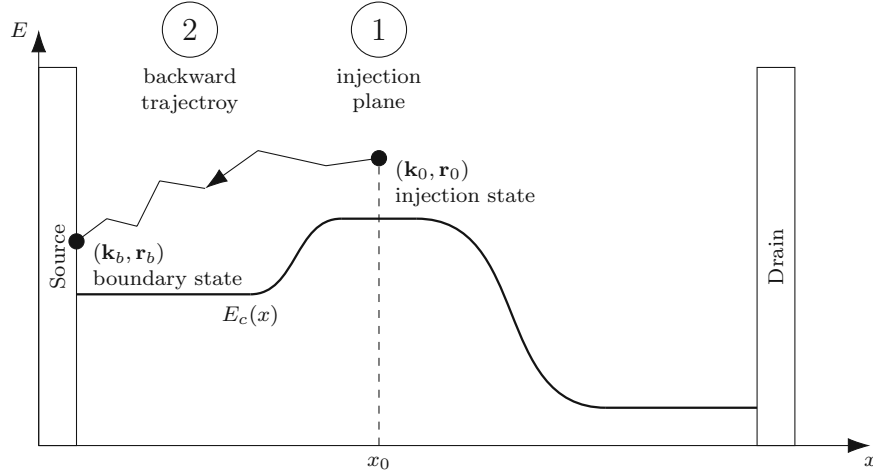


Figure 4.1.: Principle of the backward MC method applied to a MOSFET. The injected particle has a chosen state in r - and k -space. A trajectory is traced back in time to its origin to calculate its weight [P4].

4.1. Theory of the Backward Monte Carlo Method

With the initial conditions

$$\mathbf{K}_0(t_0) = \mathbf{k}_0 \quad \text{and} \quad \mathbf{R}_0(t_0) = \mathbf{r}_0, \quad (4.1)$$

a phase space trajectory can be obtained by formally integrating the equations of motion (2.22) and (2.23) [P4]:

$$\mathbf{K}_0(t) = \mathbf{k}_0 + \int_{t_0}^t \mathbf{F}_e(\mathbf{R}_0(\tau), \tau) d\tau, \quad (4.2)$$

$$\mathbf{R}_0(t) = \mathbf{r}_0 + \int_{t_0}^t \mathbf{v}(\mathbf{K}_0(\tau)) d\tau. \quad (4.3)$$

The BTE (2.26) can be integrated over the phase space trajectory in the manner of [59]:

$$f(\mathbf{k}_0, \mathbf{r}_0, t_0) = \int_0^{t_0} dt_1 \int d^3k_1 K(\mathbf{k}_0, t_0, \mathbf{k}_1, t_1) f(\mathbf{k}_1, \mathbf{R}(t_1), t_1) + f_0(\mathbf{k}_0, \mathbf{r}_0, t_0) \quad (4.4)$$

The resulting integral equation (4.4) represents the generalization of Chamber's path integral [13, P4, 64]. The source term of this equation includes the initial distribution for a initial value problem [61], or the boundary distribution for a boundary value problem [59]. The kernel of the integral equation is of the form:

$$K(\mathbf{k}_0, t_0, \mathbf{k}_1, t_1) = S(\mathbf{k}_1, \mathbf{K}_0(t_1)) \exp\left(-\int_{t_1}^{t_0} \lambda(\mathbf{K}_0(\tau)) d\tau\right) \quad (4.5)$$

The trajectory $\mathbf{K}_0(\tau)$ passes through \mathbf{k}_0 at the time t_0 . The kernel (4.5) in a physical sense describes a transition from (\mathbf{k}_1, t_1) to (\mathbf{k}_0, t_0) [P4].

4.1.1. Probability Density Functions

The components of the kernel (4.5) allow the construction of probability density functions (PDF). From the scattering rate S a PDF of the after-scattering states \mathbf{k}_a can be constructed [P4]:

$$p_k(\mathbf{k}_a|\mathbf{k}_b) = \frac{S(\mathbf{k}_b, \mathbf{k}_a)}{\lambda(\mathbf{k}_b)} \quad (4.6)$$

The PDF of the before-scattering states \mathbf{k}_b can be constructed in a reverse manner:

$$p_k^*(\mathbf{k}_b|\mathbf{k}_a) = \frac{S(\mathbf{k}_b, \mathbf{k}_a)}{\lambda^*(\mathbf{k}_a)}. \quad (4.7)$$

The scattering rates

$$\lambda(\mathbf{k}_b) = \int S(\mathbf{k}_b, \mathbf{k}_a) d^3k_a, \quad (4.8)$$

$$\lambda^*(\mathbf{k}_a) = \int S(\mathbf{k}_b, \mathbf{k}_a) d^3k_b, \quad (4.9)$$

are serving as normalization factors. The path integral in (4.5) is leading to the PDF of the backward free-flight time t_1 [P4]:

$$p_t^*(t_1|t_0; \mathbf{k}_0) = \lambda(\mathbf{K}_0(t_1)) \exp\left(-\int_{t_1}^{t_0} \lambda(\mathbf{K}_0(\tau)) d\tau\right), \quad t_1 < t_0 \quad (4.10)$$

With the transformation $t^* = -t$, $\mathbf{k}^* = -\mathbf{k}$, and $\mathbf{v}^* = -\mathbf{v}$, the equations of motion (2.22) and (2.23) can be shown to be form-invariant [P4]. Therefore, the equations of motion for the forward path can also be used for the backward path. The vector \mathbf{r} and the force field \mathbf{F}_e need not be inverted. Consequently, the substitution $\tau^* = -\tau$ transforms the PDF of the backward free-flight time (4.10) to the PDF of the forward free-flight [P4]:

$$p_t(t_1^*|t_0^*; \mathbf{k}_0^*) = \lambda(\mathbf{K}_0^*(t_1^*)) \exp\left(-\int_{t_0^*}^{t_1^*} \lambda(\mathbf{K}_0^*(\tau^*)) d\tau^*\right), \quad t_1^* > t_0^* \quad (4.11)$$

4. Backward Monte Carlo Method

Both PDFs (4.10) and (4.11) are normalized:

$$\int_{-\infty}^{t_0} p_t^*(t_1|t_0) dt_1 = 1, \quad (4.12)$$

$$\int_{t_0^*}^{\infty} p_t(t_1^*|t_0^*) dt_1^* = 1. \quad (4.13)$$

4.1.2. The Backward MC Method

In the more familiar forward MC method, the scattering events occur in an ascending time sequence: $t_0 < t_1 < t_2 < \dots$. In the backward MC method based on (4.4) the scattering events occur in a descending sequence: $t_0 > t_1 > t_2 > \dots$.

The distribution function f in one point $(\mathbf{k}_0, \mathbf{r}_0)$ can be estimated by the BMC method by the following sample mean [P4]:

$$f(\mathbf{k}_0, \mathbf{r}_0, t_0) \simeq \frac{1}{N} \sum_{s=1}^N \mu_s^{(n(s))}(\mathbf{k}_0, \mathbf{r}_0, t_0) \quad (4.14)$$

The number of trajectories is represented by N , and $n(s)$ is denoting the order of the s -th numerical trajectory, which is the number of scattering events occurring in the time interval $[0, t_0]$. In literature, there are two different kinds of estimators $\mu^{(n)}$. One is based on mathematical considerations, the other on physical considerations. Both of them will be discussed below.

Transition Rate Derived from Mathematical Considerations

The first works regarding the BMC method, [45] and [73], interpreted $S(\mathbf{k}_b, \mathbf{k}_a)$ as the unnormalized distribution of the before-scattering states \mathbf{k}_b . Thus, the normalized PDF (4.10) is applied [P4]. With the transition density

$$P(\mathbf{k}_1, t_1 | \mathbf{k}_0, t_0) = p_k^*(\mathbf{k}_1 | \mathbf{K}_0(t_1)) p_t(t_1 | t_0; \mathbf{k}) \quad (4.15)$$

the estimator in (4.14) becomes

$$\mu^{(n)}(\mathbf{k}_0, \mathbf{r}_0, t_0) = \frac{\lambda^*(\mathbf{K}_0(t_1))}{\lambda(\mathbf{K}_0(t_1))} \dots \frac{\lambda^*(\mathbf{K}_{n-1}(t_n))}{\lambda(\mathbf{K}_{n-1}(t_n))} f_{\text{in}}(\mathbf{K}_n(0), \mathbf{R}_n(0)), \quad (4.16)$$

where f_{in} denotes the initial distribution. A trajectory of second order ($n = 2$) is illustrated in Fig. 4.2.

Though the estimator (4.16) is formally derived from the BTE, previous simulations revealed a stability problem. The energy of one particle becomes statistical

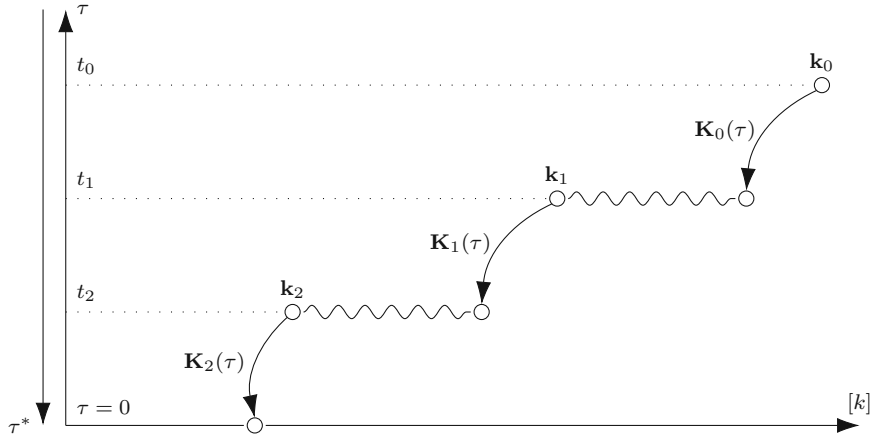


Figure 4.2.: Illustration of a backward trajectory starting at time t_0 and reaching time 0 after three free flights. The symbols used in the estimator (4.16) are shown.

very high when the trajectory is followed back in time, as sketched in Fig. 4.3. The initial distribution takes on very small values for high energies. Whereas the probability that the particle energy becomes low is very small, but the initial distribution for low energies is high. These rare events are contributing mainly to the estimator and causing a large variance. The simulations show that the variance is increasing quickly over time. However, for a finite time t the variance of the estimator is finite [P4].

Transition Rate Derived from Physical Considerations, based on [P4]

The time evolution of the particle energy can be understood from a property of the scattering rate known as the principle of detailed balance. This property ensures that in any system particles scatter preferably to lower energies. If the backward transition rate (4.7) is employed for trajectory construction, in the simulation the principle of detailed balance is inverted, and scattering to higher energies is preferred.

The principle of detailed balance is reflected by the following symmetry property of the scattering rate [61]:

$$S(\mathbf{k}_i, \mathbf{k}_j) = S(\mathbf{k}_j, \mathbf{k}_i) e^{\beta_D(\mathcal{E}(\mathbf{k}_i) - \mathcal{E}(\mathbf{k}_j))}, \quad (4.17)$$

where $\beta_D = (k_B T_D)^{-1}$ with T_D being the device temperature, and $\mathcal{E}(\mathbf{k})$ denoting the carrier energy. The stability problem can be solved by using the forward scattering rate also for the construction of the backward trajectory and changing the estimator accordingly, as sketched in Fig. 4.4. In the transition density the

4. Backward Monte Carlo Method

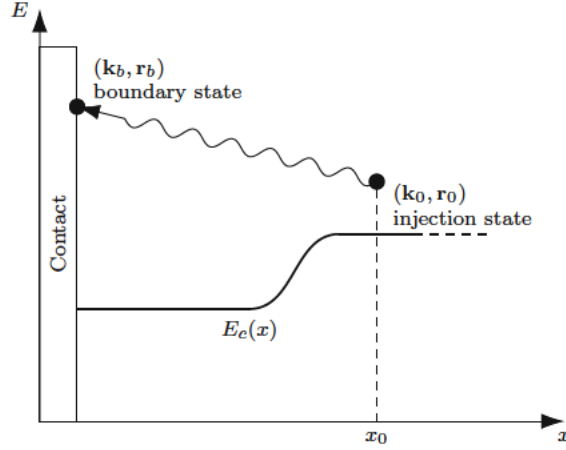


Figure 4.3.: Unstable BMC algorithm. Particle tend to higher energies.

forward PDF (4.6) is employed [61].

$$P(\mathbf{k}_1, t_1 | \mathbf{k}_0, t_0) = p_k(\mathbf{k}_1 | \mathbf{K}_0(t_1)) p_t(t_1 | t_0; \mathbf{k}_0) \quad (4.18)$$

The estimator in (4.14) becomes

$$\mu^{(n)}(\mathbf{k}, \mathbf{r}, t) = e^{\beta_D \Delta \mathcal{E}_1} \dots e^{\beta_D \Delta \mathcal{E}_n} f_{\text{in}}(\mathbf{K}_n(0), \mathbf{R}_n(0)). \quad (4.19)$$

Here, the difference in carrier energy induced by the l -th scattering event is denoted by $\Delta \mathcal{E}_l$.

The result obtained for the initial value problem can be adapted straightforwardly for the stationary boundary value problem. The total electron energy is defined as

$$H(\mathbf{k}, \mathbf{r}) = \mathcal{E}(\mathbf{k}) + E_C(\mathbf{r}) \quad (4.20)$$

where $E_C(\mathbf{r})$ is the conduction band edge. In the following, the starting point of a backward trajectory is labeled as $(\mathbf{k}_0, \mathbf{r}_0)$, and the endpoint at a Dirichlet boundary as $(\mathbf{k}_b, \mathbf{r}_b)$, see Fig. 4.1. A Dirichlet boundary is imposed by an ohmic contact, where an equilibrium distribution can be assumed. The boundary distribution at a contact will be referred to as f_b . Inelastic scattering events cause a difference in the total energy along a trajectory. Using the energy balance equation

$$H(\mathbf{k}_b, \mathbf{r}_b) - H(\mathbf{k}_0, \mathbf{r}_0) = \sum_l \Delta \mathcal{E}_l \quad (4.21)$$

the estimator (4.19) becomes

$$\mu^{(n)}(\mathbf{k}, \mathbf{r}, t) = e^{\beta_D (H(\mathbf{k}_b, \mathbf{r}_b) - H(\mathbf{k}_0, \mathbf{r}_0))} f_b(\mathbf{k}_{b,i}, \mathbf{r}_{b,i}), \quad (4.22)$$

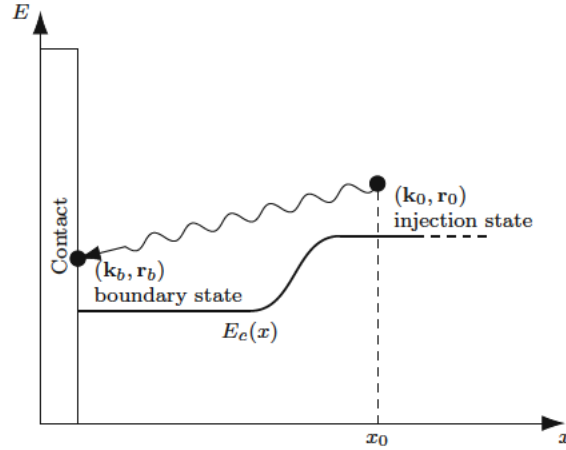


Figure 4.4.: Stable BMC algorithm, satisfying the principle of detailed balance.

where the initial distribution f_{in} has been replaced by the boundary distribution f_b . Finally, the distribution function in a given point $(\mathbf{k}_0, \mathbf{r}_0)$ is estimated by the sample mean (4.14). The distribution function in a given point $(\mathbf{k}_0, \mathbf{r}_0)$ becomes

$$f(\mathbf{k}_0, \mathbf{r}_0) = \frac{1}{M} \sum_{i=1}^M f_b(\mathbf{k}_{b,i}, \mathbf{r}_{b,i}) e^{\beta_D(H(\mathbf{k}_{b,i}, \mathbf{r}_{b,i}) - H(\mathbf{k}_0, \mathbf{r}_0))}. \quad (4.23)$$

Here, M is the number of backward trajectories started from the point $(\mathbf{k}_0, \mathbf{r}_0)$. Note that the backward trajectory is constructed in the very same manner as a forward trajectory. Using the forward PDF (4.11) to generate the free-flight time means that we have inverted the time axis and are progressing along the negative time axis. The selection of the scattering mechanism and the calculation of the after-scattering state are also identical to the forward algorithm.

4.2. Current Estimators

The main difference between the current definition of the FMC method (3.64) and the BMC method is, that the BMC method is calculating the current not through a contact but through an area $y_m \times W$ in the yz -plane located at $x = x_0$ [P6]:

$$I = \frac{q}{4\pi^3} W \int_0^{y_m} \int_{\text{BZ}} v_x(\mathbf{k}_0) f(\mathbf{k}_0, x_0, y_0) d^3k_0 dy_0, \quad (4.24)$$

In principle, the integral in (4.24) could be evaluated by numerical integration, whereby the values of the distribution function at the discrete points $(\mathbf{k}_0, \mathbf{r}_0)$ are

4. Backward Monte Carlo Method

estimated by (4.23). However, it is more convenient to employ Monte Carlo integration instead. For this purpose, the current has to be expressed as an expectation value. This is accomplished by introducing a PDF $p_0(\mathbf{k}_0, y_0)$ which can be chosen freely, and reformulating (4.24) as [P4]:

$$I = qW \int_0^{y_m} \int_{\text{BZ}} \mu(\mathbf{k}_0, y_0; x_0) p_0(\mathbf{k}_0, y_0) d^3k_0 dy_0 \equiv qWE\{\mu\} \quad (4.25)$$

with

$$\mu(\mathbf{k}_0, y_0; x_0) = \frac{v_x(\mathbf{k}_0) f(\mathbf{k}_0, x_0, y_0)}{4\pi^3 p_0(\mathbf{k}_0, y_0)}. \quad (4.26)$$

In a Monte Carlo simulation, the expectation value is estimated by a sample mean [83].

$$I = qWE\{\mu\} \approx qW \frac{1}{N} \sum_{i=1}^N \mu(\mathbf{k}_{0,i}, y_{0,i}; x_0) \quad (4.27)$$

Here, N denotes the number of sampling points. With the estimated distribution function (4.23) the estimator (4.26) takes the form

$$\mu(\mathbf{k}_0, y_0; x_0) = \frac{v_x(\mathbf{k}_0) f_b(\mathbf{k}_b, \mathbf{r}_b)}{4\pi^3 p_0(\mathbf{k}_0, y_0)} e^{\beta_D(H(\mathbf{k}_b, \mathbf{r}_b) - H(\mathbf{k}_0, \mathbf{r}_0))}. \quad (4.28)$$

Consider, that with this definition only one trajectory per sampling point $(\mathbf{k}_{0,i}, y_{0,i})$ is started, corresponding to $M = 1$ in (4.23).

The estimator (4.28) is the fundamental equation from which various variants can be derived. The following sections discuss different choices of the injection PDF p_0 and the properties of the resulting current estimators [P4]. In (4.28), \mathbf{k}_0 and y_0 are random variables, whereas x_0 is a given parameter. In the following, x_0 is omitted from the argument list for the sake of readability.

4.2.1. The Boundary Distribution

Distribution functions at ohmic contacts are close to thermal equilibrium. Therefore, a Maxwell-Boltzmann or Fermi-Dirac distribution is an appropriate choice for the the boundary distribution f_b . Here, an equilibrium Boltzmann distribution is assumed:

$$f_b(\mathbf{k}, \mathbf{r}) = \mathcal{C}(\mathbf{r}) e^{-\beta_D \mathcal{E}(\mathbf{k})} \quad (4.29)$$

Two normalization integrals will be needed in the following. The first one is the partition function $Z(T)$ (3.58) and the second integral is defined as

$$V(T) = \int_{\text{BZ}} |v_x(\mathbf{k}_0)| e^{-\beta(T)\mathcal{E}(\mathbf{k}_0)} d^3k. \quad (4.30)$$

The integrations over the Brillouin zone (BZ) are carried out numerically, see Appendix A.1. From these two quantities the injection velocity is obtained:

$$v_{\text{inj}}(T) = \frac{V(T)}{Z(T)} \quad (4.31)$$

The definition of the electron concentration

$$n(\mathbf{r}) = \frac{1}{4\pi^3} \int_{\text{BZ}} f_b(\mathbf{k}, \mathbf{r}) d^3k \quad (4.32)$$

is used to determine the normalization constant \mathcal{C} in (4.29):

$$\mathcal{C}(\mathbf{r}) = \frac{4\pi^3 n(\mathbf{r})}{Z(T_D)} \quad (4.33)$$

4.2.2. Injection from an Equilibrium Maxwellian

The starting points of the backward trajectories are generated by the PDF p_0 . We express p_0 as a product of two independent PDFs:

$$p_0(\mathbf{k}_0, y_0) = f_0(\mathbf{k}_0) p_y(y_0) \quad (4.34)$$

The PDF of the injection coordinate y_0 is assumed to be proportional to the electron concentration at the injection coordinate x_0 .

$$p_y(y_0) = \frac{n(x_0, y_0)}{\int_0^{y_m} n(x_0, y) dy} \quad (4.35)$$

For the injection distribution f_0 , a normalized Boltzmann distribution at device temperature T_D is chosen.

$$f_0(\mathbf{k}_0) = \frac{1}{Z(T_D)} e^{-\beta_D \mathcal{E}(\mathbf{k}_0)} \quad (4.36)$$

Inserting the boundary distribution (4.29) and the injection distribution (4.36) in (4.28) gives the following current estimator [P4]:

$$\mu = v_x(\mathbf{k}_0) \frac{e^{\beta_D (E_C(\mathbf{r}_b) - E_C(\mathbf{r}_0))}}{p_y(y_0)} n(\mathbf{r}_b) \quad (4.37)$$

Note that both the Boltzmann factors $e^{-\beta_D \mathcal{E}(\mathbf{k}_0)}$ and $e^{-\beta_D \mathcal{E}(\mathbf{k}_b)}$ have canceled out of this expression. To generate wave vectors from the equilibrium distribution (4.36), the *constant time sampling* method described in Section 3.3.5 can be used.

4. Backward Monte Carlo Method

4.2.3. Injection from a Velocity-weighted Maxwellian

Another choice for f_0 is a velocity-weighted Maxwellian at equilibrium temperature T_D [P4]:

$$f_0(\mathbf{k}_0) = \frac{1}{V(T_D)} |v_x(\mathbf{k}_0)| e^{-\beta_D \mathcal{E}(\mathbf{k}_0)} \quad (4.38)$$

This choice is motivated by the fact that in the numerator of (4.28) a term $v_x(k_0) e^{-\beta_D \mathcal{E}(k_0)}$ occurs. Division by (4.38) will essentially cancel out this term. This reduces the k_0 -dependence of the estimator which is expected to reduce its variance. Inserting the boundary distribution (4.29) and the injection distribution (4.38) in (4.28) yields

$$\mu = \text{sign}(v_x(\mathbf{k}_0)) v_{\text{inj}}(T_D) \frac{e^{\beta_D (E_C(\mathbf{r}_b) - E_C(\mathbf{r}_0))}}{p_y(y_0)} n(\mathbf{r}_b). \quad (4.39)$$

In this equation, $\text{sign}(v_x)$ denotes the sign of the velocity component v_x , and v_{inj} is the injection velocity defined by (4.31). To generate wave vectors from the equilibrium distribution (4.38), the *box sampling* method described in Section 3.3.5 can be used.

4.2.4. Injection from a Non-equilibrium Maxwellian

For some applications, it can be useful to generate the initial points \mathbf{k}_0 from a Maxwellian at a temperature T_0 different from the device temperature T_D [P4]. When calculating quantities depending on the high energy tail of the distribution, an injection temperature $T_0 > T_D$ will be beneficial as it enhances the number of initial points at higher energies. In this work a non-equilibrium Maxwellian of the form

$$f_0(\mathbf{k}_0) = \frac{1}{Z(T_0)} e^{-\beta_0 \mathcal{E}(\mathbf{k}_0)} \quad (4.40)$$

is considered. Injecting with this non-equilibrium distribution, equation (4.28) leads to an estimator η :

$$\eta(\mathbf{k}_0, y_0) = \frac{Z(T_0)}{Z(T_D)} v_x(\mathbf{k}_0) \frac{e^{\beta_D (E_C(\mathbf{r}_b) - E_C(\mathbf{r}_0))}}{p_y(y_0)} \times e^{(\beta_0 - \beta_D) \mathcal{E}(\mathbf{k}_0)} n(\mathbf{r}_b) \quad (4.41)$$

The sample mean of η ,

$$I = qW \frac{1}{N} \sum_{i=1}^N \eta(\mathbf{k}_{0,i}, y_{0,i}), \quad (4.42)$$

can be reformulated as a weighted average of the form:

$$I = qW \frac{\sum_{i=1}^N \mu(\mathbf{k}_{0,i}, y_{0,i}) w(\mathbf{k}_{0,i})}{\sum_{i=1}^N w(\mathbf{k}_{0,i})} \quad (4.43)$$

Here, μ is given by (4.37) and the weight factor w is defined as

$$w(\mathbf{k}_0) = e^{(\beta_0 - \beta_D) \mathcal{E}(\mathbf{k}_0)}. \quad (4.44)$$

The derivation of (4.43) is described in detail in [P4]. In the case of a velocity-weighted Maxwellian with $T_0 \neq T_D$,

$$f_0(\mathbf{k}_0) = \frac{1}{V(T_0)} |v_x(\mathbf{k}_0)| e^{-\beta_0 \mathcal{E}(\mathbf{k}_0)}$$

a similar procedure can be applied. In the weighted average (4.43) the estimator (4.39) and the very same weight (4.44) have to be used [P4].

4.2.5. Injection from the Equilibrium Concentration

All previous estimators have a dependence on the injection coordinate y_0 through the term $e^{\beta_D E_C(\mathbf{r}_0)}/p_y(y_0)$. However, this dependency is weak and can even be eliminated from the estimator by choosing the injection distribution as [P4]:

$$p_0(\mathbf{k}_0, y_0; x_0) = \frac{1}{A(T_D)} |v_x(\mathbf{k}_0)| e^{-\beta_D H(\mathbf{k}_0, x_0, y_0)} \quad (4.45)$$

Inserting (4.20) in (4.45) again yields a product of two independent PDFs.

$$p_0(\mathbf{k}_0, y_0) = f_0(\mathbf{k}_0) \tilde{p}_y(y_0) \quad (4.46)$$

Here, f_0 is given by (4.38), and \tilde{p}_y is defined as

$$\tilde{p}_y(y_0) = \frac{\tilde{n}(x_0, y_0)}{B(T_D)} \quad (4.47)$$

with $\tilde{n}(x_0, y_0) = e^{-\beta_D E_C(x_0, y_0)}$. This quantity is up to a constant the equilibrium concentration determined by the band edge energy E_C . On the other hand, n in (4.35) represents the actual carrier concentration as obtained from a device simulation. With the normalization integral in (4.47) defined as

$$B(T_D) = \int_0^{y_m} \tilde{n}(x_0, y) dy, \quad (4.48)$$

4. Backward Monte Carlo Method

the total normalization factor A in (4.45) becomes

$$A(T_D) = V(T_D) B(T_D). \quad (4.49)$$

Using the boundary distribution (4.29) and the injection distribution (4.45) the current estimator (4.28) can be reformulated as:

$$\mu = \text{sign}(v_x(\mathbf{k}_0)) v_{\text{inj}}(T_D) B(T_D) n(\mathbf{r}_b) e^{\beta_D E_C(\mathbf{r}_b)} \quad (4.50)$$

Other than the estimators discussed above, this estimator is independent of the injection coordinate y_0 . A more transparent physical interpretation is achieved by expressing the equilibrium concentration $n(\mathbf{r}_b)$ as a function of the local quasi-Fermi level F_n .

$$n(\mathbf{r}_b) = N_C(T_D) e^{\beta_D (F_n(\mathbf{r}_b) - E_C(\mathbf{r}_b))} \quad (4.51)$$

Here, the effective density of states N_C is related to the partition function Z by $N_C = Z/(4\pi^3)$. Also, the normalization factor B will be expressed through an energy \bar{E}_C defined as

$$\bar{E}_C = -k_B T_D \ln \left(\frac{B}{y_m} \right). \quad (4.52)$$

\bar{E}_C has the meaning of an average of the band edge energy over the injection coordinate y_0 :

$$e^{-\beta_D \bar{E}_C(x_0)} = \frac{1}{y_m} \int_0^{y_m} e^{-\beta_D E_C(x_0, y_0)} dy_0 \quad (4.53)$$

Expressing the estimator (4.50) in terms of the parameters F_n and \bar{E}_C gives

$$\mu = y_m N_C(T_D) v_{\text{inj}}(T_D) \text{sign}(v_x(\mathbf{k}_0)) e^{\beta_D (F_n(\mathbf{r}_b) - \bar{E}_C)}. \quad (4.54)$$

This equation states that a backward trajectory represents an elementary particle flux $N_C v_{\text{inj}}$. This flux is multiplied by a statistical weight given by the e-function. The higher the energy of the starting point (\bar{E}_C) with respect to the Fermi level at the trajectory end point (F_n), the lower is the statistical weight. If a constant $\Delta\mathcal{E}$ were added to \bar{E}_C , the estimator μ and subsequently also the current I would be scaled by the factor $e^{-\beta_D \Delta\mathcal{E}}$. In other words, increasing the barrier height by some energy increment will result in an exponential decrease in current. This means that the exponential dependence of the thermionic current on the barrier height can be directly deduced from the current estimator (4.54) [P4].

4.2.6. Symmetric Sampling

In thermodynamic equilibrium the distribution function is symmetric. Because of this symmetry, the current will vanish. In a BMC simulation the current is not vanishing exactly because of the finite sample size. However, this type of statistical error can be eliminated by always generating positive and negative values of the estimator in pairs. When a backward trajectory is started from a state (\mathbf{k}_0, y_0) , also another one is started with opposite momentum from the state $(-\mathbf{k}_0, y_0)$. This procedure will give exactly $I = 0$ in thermal equilibrium without statistical error and is reducing the statistical error in situations close to thermal equilibrium.

Every estimator described above can be used to define a new estimator by taking the algebraic mean value [P4]:

$$\mu_{\text{symm}}(\mathbf{k}_0, y_0) = \frac{\mu(\mathbf{k}_0, y_0) + \mu(-\mathbf{k}_0, y_0)}{2} \quad (4.55)$$

Using (4.54) the new estimator will be of the form:

$$\mu_{\text{symm}} = \frac{y_m N_C(T_D) v_{\text{inj}}(T_D)}{2} \left(e^{\beta_D F_n^+(\mathbf{r}_b)} - e^{\beta_D F_n^-(\mathbf{r}_b)} \right) e^{-\beta_D \bar{E}_C} \quad (4.56)$$

Here, F_n^+ denotes the quasi-Fermi level of the contact where the trajectory injected from k_0 has terminated, whereas F_n^- is the quasi-Fermi level of the contact where the trajectory injected from $-k_0$ has terminated [P4].

4.2.7. Estimation of the Statistical Error

Because of the statistical independence of the backward trajectories, an expression for the statistical error of the simulation result is readily found. In the following, μ is a function of the random variables (\mathbf{k}_0, y_0) . Several such functions $\mu(\mathbf{k}_0, y_0)$ have been discussed in the preceding sections.

In the case of the injection states \mathbf{k}_0 being generated from an equilibrium distribution, the sample mean $\bar{\mu}$ and the variance s_μ^2 of the samples $\{\mu_1, \mu_2, \dots, \mu_N\}$ can be calculated straightforwardly. The sample mean

$$\bar{\mu} = \frac{1}{N} \sum_{i=1}^N \mu_i \quad (4.57)$$

gives the current, $I = qW\bar{\mu}$, whereas the sample variance s_μ^2 allows an estimate of the current's statistical error.

$$s_\mu^2 = \frac{1}{N-1} \left(\sum_{i=1}^N \mu_i^2 - N\bar{\mu}^2 \right) \quad (4.58)$$

4. Backward Monte Carlo Method

The standard deviation of the current is estimated as

$$s_I = qW \frac{s_\mu}{\sqrt{N}} \Rightarrow \frac{s_I}{I} = \frac{1}{\sqrt{N}} \frac{s_\mu}{\bar{\mu}}. \quad (4.59)$$

The relative standard deviation s_I/I can be used as a measure for the statistical error.

In the case of the injection states \mathbf{k}_0 being generated from a non-equilibrium distribution, the random variable w defined by (4.44) and the random variable ξ defined by

$$\xi = \mu w, \quad (4.60)$$

are needed. In the course of a Monte Carlo simulation, the sample means $\bar{\xi}$ and \bar{w} have to be calculated in order to obtain the current [P4]:

$$\bar{\xi} = \frac{1}{N} \sum_{i=1}^N \xi_i, \quad \bar{w} = \frac{1}{N} \sum_{i=1}^N w_i \Rightarrow I = qW \frac{\bar{\xi}}{\bar{w}} \quad (4.61)$$

In addition, the sample variances and the sample covariance have to be determined.

$$s_\xi^2 = \frac{1}{N-1} \left(\sum_{i=1}^N \xi_i^2 - N \bar{\xi}^2 \right) \quad (4.62)$$

$$s_w^2 = \frac{1}{N-1} \left(\sum_{i=1}^N w_i^2 - N \bar{w}^2 \right) \quad (4.63)$$

$$s_{\xi w}^2 = \frac{1}{N-1} \left(\sum_{i=1}^N \xi_i w_i - N \bar{\xi} \bar{w} \right) \quad (4.64)$$

Using these parameters, the variance of the random variable $\mu = \xi/w$ can be estimated as

$$s_\mu^2 = s_\xi^2 - 2r s_{\xi w}^2 + r^2 s_w^2, \quad (4.65)$$

where $r = \bar{\xi}/\bar{w}$ [83]. From s_μ , the standard deviation of the current can be computed.

$$s_I = qW \frac{s_\mu}{\sqrt{N} \bar{w}} \Rightarrow \frac{s_I}{I} = \frac{1}{\sqrt{N}} \frac{s_\mu}{\bar{\xi}} \quad (4.66)$$

4.3. Multi-Band Semiconductors

The formalism in the sections above is assuming carrier transport in one band only. However, the extension of the formalism to a many band structure is straightforward. The definitions of the normalization factors (3.58) and (4.30) have to be

4.4. The Combined Backward-Forward MC Method

extended by a summation over the band index n [P4]:

$$Z(T) = \sum_n \int_{\text{BZ}} e^{-\beta(T) \mathcal{E}_n(\mathbf{k})} d^3k \quad (4.67)$$

$$V(T) = \sum_n \int_{\text{BZ}} |v_x^{(n)}(\mathbf{k}_0)| e^{-\beta(T) \mathcal{E}_n(\mathbf{k}_0)} d^3k \quad (4.68)$$

The band energy \mathcal{E}_n denotes the energy of an electron in band n with respect to the band edge energy E_C . Equation (4.32) defining the electron concentration at equilibrium has to account for a summation over the band index as well.

$$n(\mathbf{r}) = \frac{\mathcal{C}(\mathbf{r})}{4\pi^3} \sum_n \int_{\text{BZ}} e^{-\beta(T) \mathcal{E}_n(\mathbf{k})} d^3k \quad (4.69)$$

The definition (4.33) of normalization factor \mathcal{C} remains unchanged. Sampling an equilibrium trajectory in a multi-band simulation yields random injection states of the form (n_0, \mathbf{k}_0) , where n_0 is the initial band index.

4.4. The Combined Backward-Forward MC Method

The forward MC method and the backward MC method can be combined. The following considerations can be found in [P4].

In semiconductor devices, there are various processes which are caused by carriers with energies above a certain energy threshold. Such processes are impact ionization, carrier injection into the oxide, and the generation of interface traps due to hot carriers. To model such processes, only carriers with energies above the threshold need to be considered, whereas carriers with lower energies have no effect. Therefore, a reasonable approximation in the modeling of such processes is to consider only those high energetic carriers that are able to surmount the energy barrier and to neglect the vast majority of carriers close to thermal equilibrium that get reflected on either side of the barrier.

This motivates the introduction of a combined backward-forward Monte Carlo method which simulates only those trajectories passing the energy barrier, as shown in Fig. 4.5. In the first step of this method, a backward trajectory is started from the injection plane at x_0 with a random initial state (\mathbf{k}_0, y_0) . The contribution of this trajectory to the estimator (4.23) determines the statistical weight of this state:

$$w(\mathbf{k}_0, \mathbf{r}_0) = f_b(\mathbf{k}_b, \mathbf{r}_b) e^{\beta_D(H(\mathbf{k}_b, \mathbf{r}_b) - H(\mathbf{k}_0, \mathbf{r}_0))} \quad (4.70)$$

4. Backward Monte Carlo Method

In the second step, a forward trajectory is started from the state $(-\mathbf{k}_0, y_0)$. This trajectory is assigned the statistical weight (4.70). The quantities of interest are computed as a weighted average over an ensemble of forward trajectories. Note that the backward trajectories are only needed to determine the weights. No averages are computed from those trajectories.

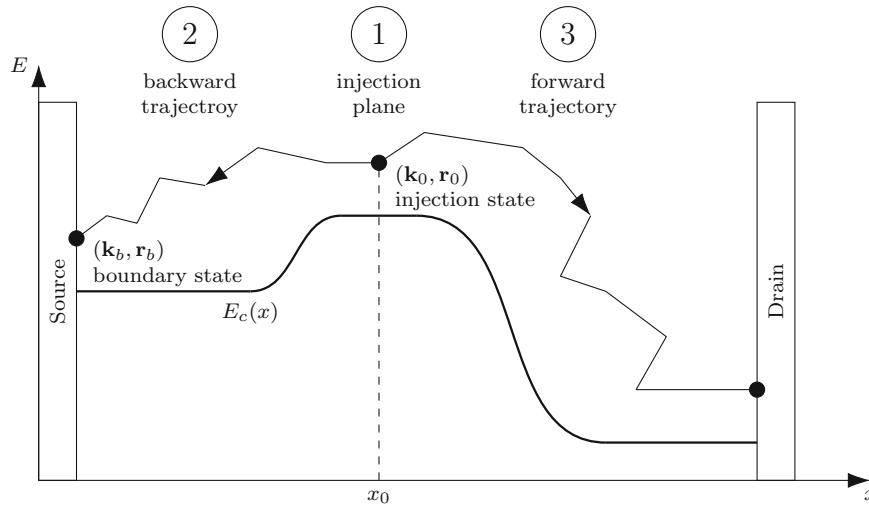


Figure 4.5.: Principle of the combined backward-forward MC method for a MOSFET. The injected particle has a chosen state in \mathbf{r} - and \mathbf{k} -space. A trajectory is traced back in time to its origin to calculate the weight. The local attributes are calculated from the weighted forward trajectories [P4].

4.5. Results and Discussion

The BMC method, as well as the different estimators described above, have been implemented in the full-band Monte Carlo simulator VMC [P1]. Backward trajectories are constructed in the same manner as forward trajectories. Routines for the computation of the free flight and the after scattering states can be used without modification.

For testing purposes the structure of a planar n-channel MOSFET with a gate length of $L_G = 65$ nm, an effective oxide thickness of $t_{ox} = 2.5$ nm, and a channel width of $W = 1 \mu\text{m}$ is used. Device geometry and doping profiles have been obtained by process simulation [104]. A sketch of the device structure is shown in Fig. 4.6. Room temperature is assumed for all simulations ($T_D = 300$ K). The following results and discussions are found in a previous work [P4].

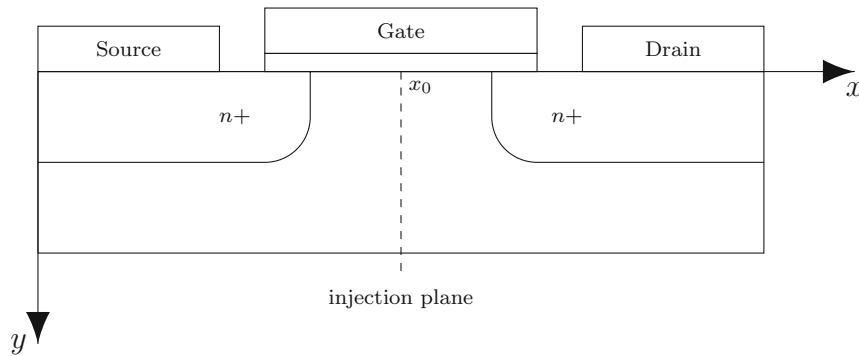


Figure 4.6.: Sketch of a MOSFET.

4.5.1. Transfer Characteristics

The transfer characteristics have been calculated using the classical device simulator Minimos-NT [71, 94], the conventional FMC method, and the novel BMC method. Each bias point is calculated with 10^6 trajectories, both with the backward and forward methods. The maximum of the energy barrier determines the location of the injection plane. It is located at $x_0 = 10.2 \text{ nm}$ relative to the left edge of the gate contact. Fig. 4.7 shows the transfer characteristics. Good agreement between the classical device simulation and the MC simulations is found. The BMC method works well in the entire sub-threshold region, whereas the FMC method (without statistical enhancement) can cover only a few orders of magnitude of the current. The barrier height in the channel increases with decreasing gate voltage. Thus, at some point none of the forward trajectories will be able to surmount the barrier, giving an estimated current of $I = 0$.

Further, the statistical error of the BMC method is depicted in Fig. 4.8. In a MOSFET the current component due to carriers injected at the source contact is nearly independent of the drain voltage, whereas the current component of carries originating from the drain contact depends strongly on the drain voltage. At $V_{DS} = 2.2 \text{ V}$ the back diffusion current from the drain is extremely small, and the total current is dominated by forward diffusion, which will result in a low variance. At $V_{DS} = 50 \text{ mV}$, on the other hand, the back diffusion current is significant, and a stronger compensation of the two current components takes place, which will result in a higher variance. This explanation, using the forward time picture also holds true in the backward time picture. There a large difference in the two current components is reflected by a significant difference in the statistical weights of the forward and backward diffusing carriers.

In Fig. 4.9 the computation times for a given error tolerance of 10^{-2} are compared. In the on-state ($V_{GS} = 2.2 \text{ V}$) BMC is about five times faster than FMC.

4. Backward Monte Carlo Method

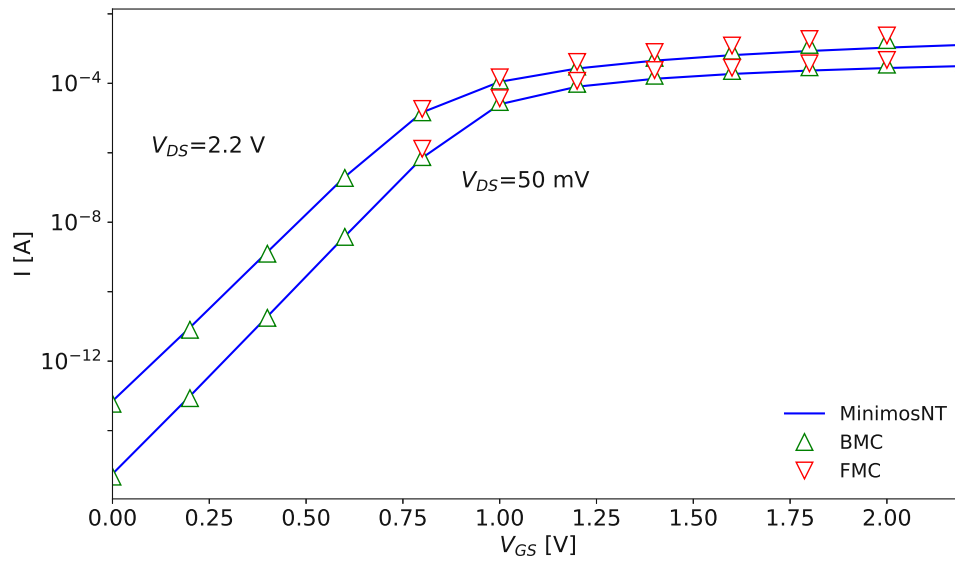


Figure 4.7.: Transfer characteristics of the nMOSFET for two drain voltages, simulated with Minimos-NT, the backward and the forward MC methods.

Although in this operating point the energy barrier in the channel is almost completely suppressed, many electrons injected at the source contact get reflected by the geometrical constriction at the source-channel junction. Since the BMC method needs not simulate these reflected carriers, it shows a clear gain also in the on-state. The last point that could be simulated with FMC within a reasonable time was $V_{GS} = 0.8$ V. In this operating point, BMC is about 2300 times faster than FMC as shown in Fig. 4.9.

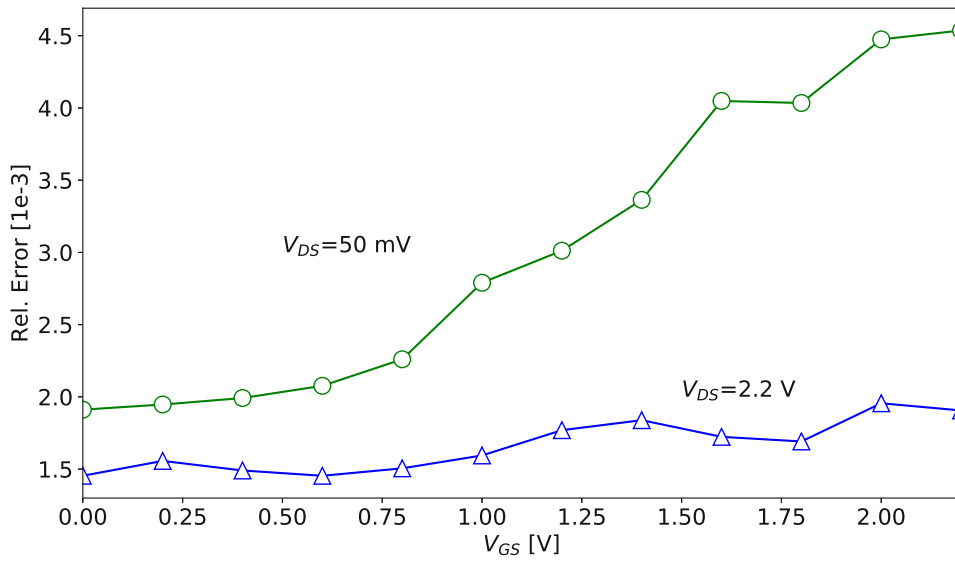


Figure 4.8.: Relative Error (relative standard deviation) of the drain current for two drain voltages. Each bias point is calculated with 10^6 backward trajectories. The current estimator (4.37) was used.

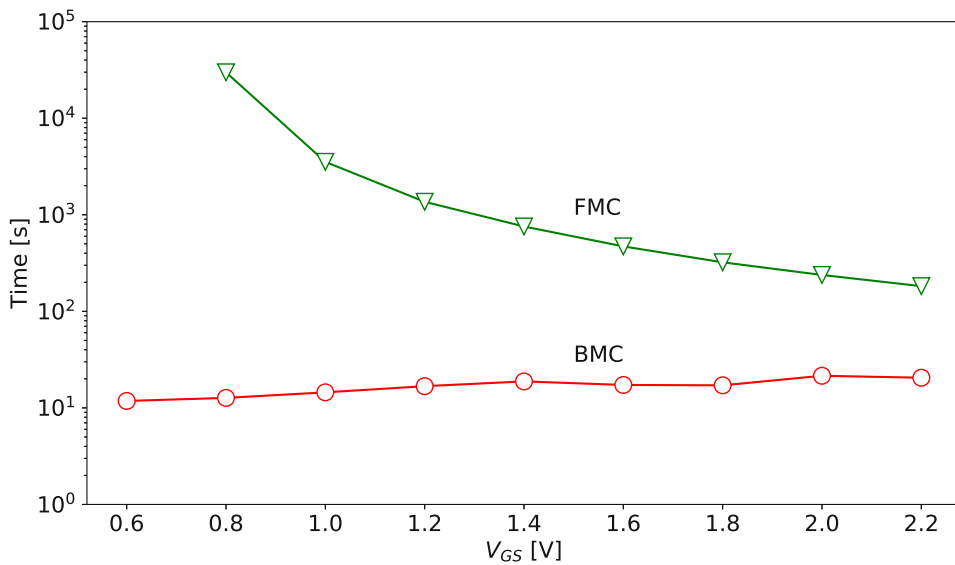


Figure 4.9.: Computation times by a single core of an Intel i7 processor. The operating points of the transfer characteristics at $V_{DS} = 2.2$ V are considered. A relative standard deviation of 10^{-2} is assumed.

4.5.2. Output Characteristics

Fig. 4.10 compares the output characteristics computed by three different methods. As shown in Fig. 4.11, the statistical error decreases with increasing V_{DS} , a trend already discussed in the previous section. The figure also shows that the variance of the symmetric estimator (4.56) is lower in the entire range of drain voltages. Especially at low V_{DS} , where the device is approaching thermal equilibrium, the variance of the non-symmetric estimator tends to explode, whereas the variance of the symmetric estimator shows only a slight increase. In this regime, variance reduction by the symmetric estimator is particularly effective. Evaluation of the

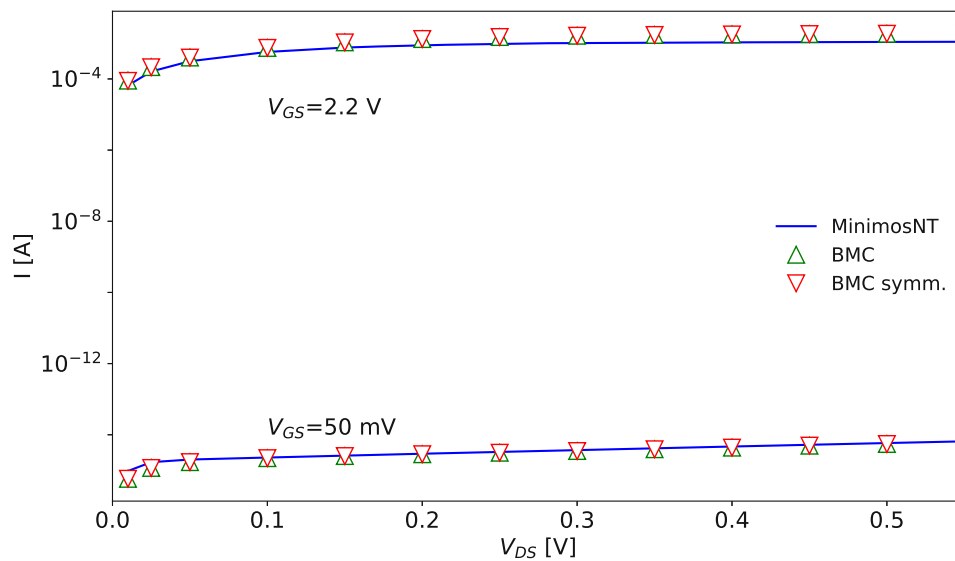


Figure 4.10.: Output characteristics of the MOSFET for two gate voltages, simulated with MinimosNT, the forward and the backward MC methods.

symmetric estimator (4.56) requires the computation of two numerical trajectories. To obtain a fair comparison of the two estimators at equal computational cost, we compute $N = 10^6$ realizations of the non-symmetric estimator (4.39) and only $N = 5 \cdot 10^5$ realizations of the symmetric estimator. Despite the sample size being smaller in the latter case, this smaller sample gives the lower statistical error.

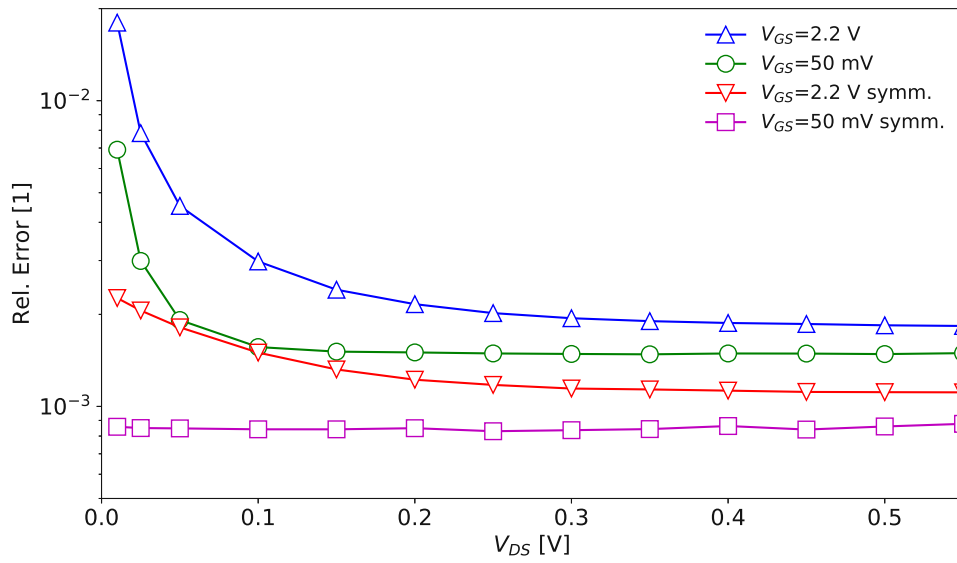


Figure 4.11.: Relative errors of the output characteristics at two gate voltages. The non-symmetric and the symmetric estimator based on the velocity-weighted Maxwellian are compared. Each bias point involves the calculation of 10^6 backward trajectories.

4.5.3. Injection from a Non-equilibrium Distribution

The injection distribution f_0 can be freely chosen and does not have any influence on the expectation value, but it does affect the estimator's variance. This fact is demonstrated by generating the random states \mathbf{k}_0 from non-equilibrium Maxwellian distributions at different temperatures. The operating point is $V_{GS} = 0.6$ V and $V_{DS} = 2.2$ V. The current is calculated using (4.43) in conjunction with the estimators (4.37) and (4.39). Fig. 4.12 shows the independence of the estimated current from the injection temperature T_0 .

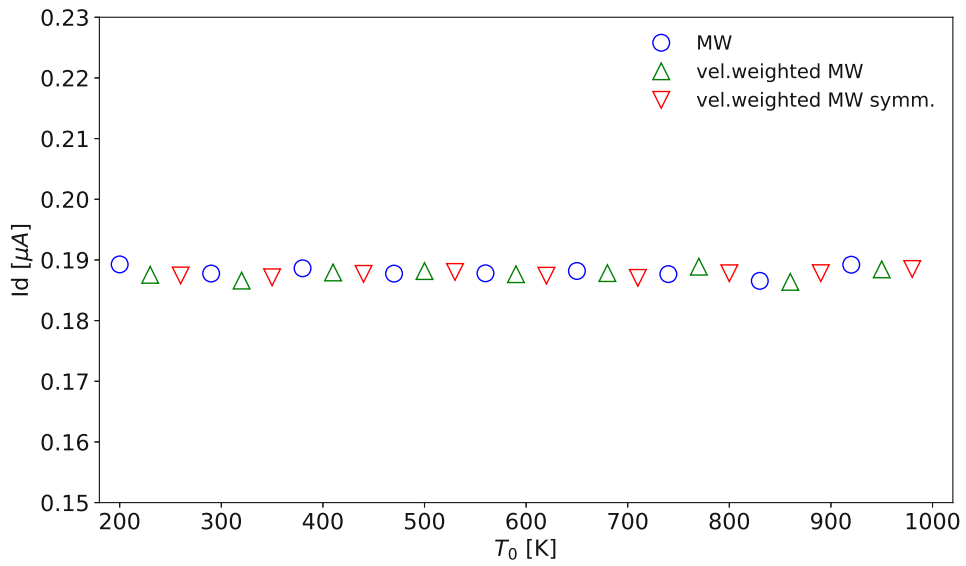


Figure 4.12.: Temperature stability of the current estimators (4.37), (4.39) and (4.56) which are based, respectively, on a Maxwellian (MW) and a velocity-weighted Maxwellian (vel.weighted MW) injection PDF. Operating point is $V_{GS} = 0.6$ V and $V_{DS} = 2.2$ V.

The estimators' relative errors are compared in Fig. 4.13. Below 700 K, estimator (4.39) shows less statistical error than estimator (4.37). For both estimators, the relative error shows a clear minimum, which can be explained as follows: the more the injection PDF f_0 resembles the real flux density $v_x f$, the lower is the current estimator's variance. From Fig. 4.13 one can conclude that a velocity-weighted Maxwellian at 290 K is the best approximation of the real flux $v_x f$ at the injection plane. With increasing and decreasing T_0 the difference between f_0 and the real flux $v_x f$ becomes larger and the relative error increases. For $T_0 > 700$ K the

velocity-weighted Maxwellian is a worse approximation to the real flux $v_x f$ than the Maxwellian and thus shows a higher variance.

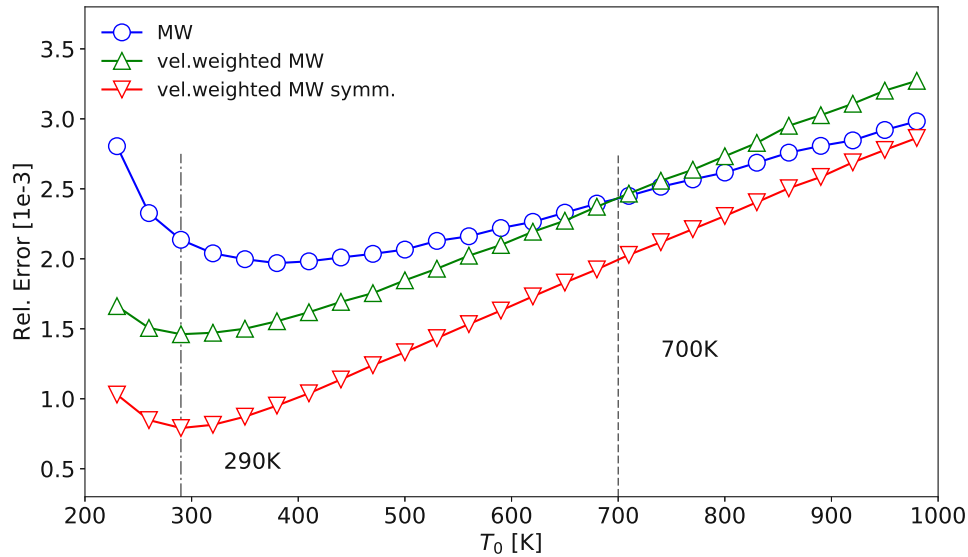


Figure 4.13.: Comparison of the relative errors of the current estimators (4.37), (4.39) and (4.56). Operating point is $V_{GS} = 0.6$ V and $V_{DS} = 2.2$ V.

4.5.4. Energy Distribution Function

Figure 4.14 shows the energy distribution function (EDF) for full-bands at three surface points in the channel of the MOSFET. The forward MC simulation performed with 10^9 trajectories can resolve only a few orders of magnitude of the EDF. Then again, with the backward MC method, the EDF is calculated point-wise with 10^4 trajectories per point using the estimator (4.23). The EDF shows a Maxwellian tail. One can compute as many orders of magnitude of the high energy tail as needed.

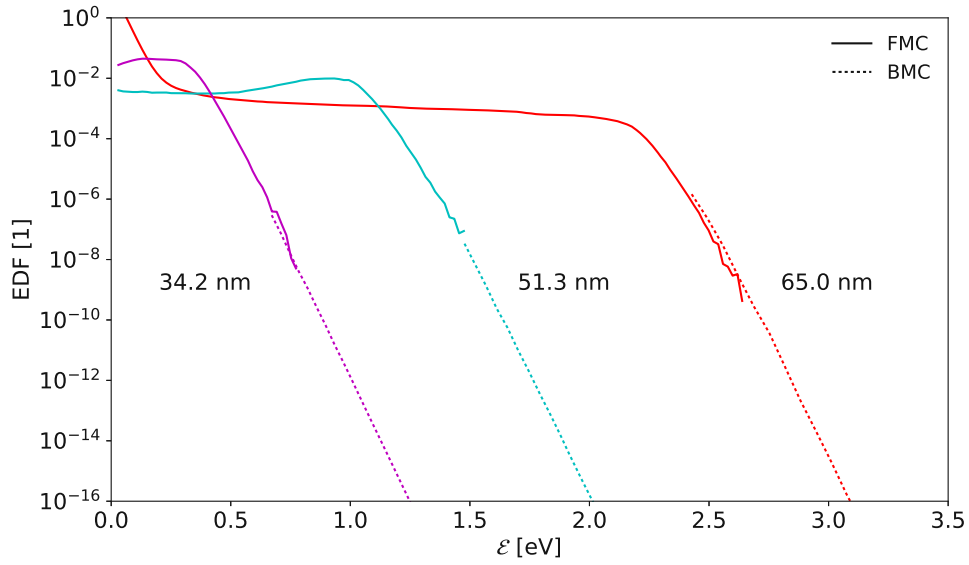


Figure 4.14.: Energy distribution function for full-bands at three surface points in the channel. The distances from the left edge of the gate electrode are given. Operating point is $V_{GS} = 2.2$ V and $V_{DS} = 2.2$ V. Solid lines: Forward MC simulation with 10^9 trajectories. Dotted lines: High energy tails computed with the backward MC method.

4.5.5. Hot Carrier Degradation

In long channel devices and high-voltage MOSFETs degradation is triggered by hot carriers. It is assumed that degradation is caused by the breaking of Si-H bonds at the silicon-oxynitride/silicon interface [104]. The bond dissociation rates are modeled by the acceleration integral, which has the general form [69]

$$I_A = \sigma_0 \int_{E_{th}}^{\infty} (E - E_{th})^p v(E) f(E) g(E) dE. \quad (4.71)$$

E_{th} denotes an energy threshold, $g(E)$ the density of states, and $v(E)$ the group velocity. For the purpose of MC estimation, (4.71) is converted into a \mathbf{k} -space integral.

$$I_A = \sigma_0 \int_{\text{BZ}} \Theta(\mathcal{E}(\mathbf{k}) - E_{\text{th}}) (\mathcal{E}(\mathbf{k}) - E_{\text{th}})^p |\mathbf{v}(\mathbf{k})| f(\mathbf{k}) d^3k \quad (4.72)$$

Here, Θ is the unit step function. For the process considered here in which one hot carrier is able to break a bond, an exponent of $p = 11$ and an energy threshold of $E_{\text{th}} = 1.5 \text{ eV}$ are assumed [104].

We used the combined backward/forward MC method (Section 4.4) to evaluate the acceleration integral. The statistical average is calculated from the forward trajectories using the before-scattering method [46]. In this simulation, 10^{10} scattering events have been computed. To enhance the number of numerical trajectories at high energies the injection temperature T_0 has been raised significantly (5000 K and 10 000 K).

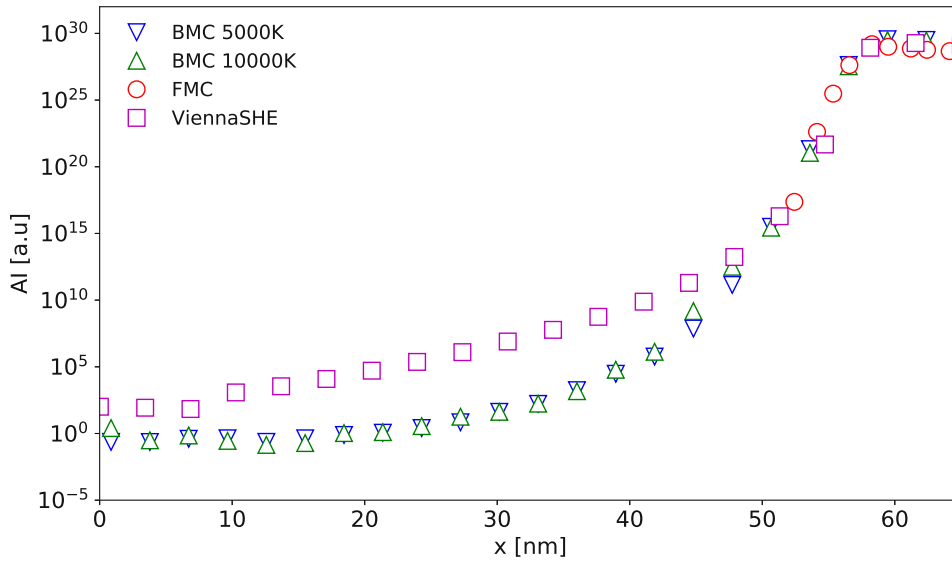


Figure 4.15.: Acceleration integral for a 65nm nMOS, simulated with FMC and BMC method at different injection temperatures.

In Fig. 4.15 the MC results are compared to the result of ViennaSHE, a deterministic solver for the BTE based on a spherical harmonics expansion of the distribution function [108]. Fig. 4.15 shows that the MC results are independent of the injection temperature. ViennaSHE predicts higher values in the first part of the channel where carrier heating is still moderate. One could attribute this

4. Backward Monte Carlo Method

difference to the band structure model which is more approximate in ViennaSHE than it is in VMC.

4.6. Conclusion

A stable backward method has been developed and implemented to overcome the statistical drawbacks of the forward method. The method allows one to calculate the current in the entire sub-threshold region including the leakage current in the off-state. Symmetric current estimators are proposed which produce less statistical error than the non-symmetric ones. This improvement is achieved for all operating conditions and is particularly large when thermal equilibrium is approached [P4].

The current through a plane is calculated by Monte Carlo integration of the current density. For this integration, one has to assume a distribution of the sampling points which in the present case are the initial wave vectors of the backward trajectories. By assuming a Maxwellian distribution at elevated temperature, the method will generate more sampling points at higher energies. This method of statistical enhancement reduces the statistical error of quantities that depend on the high-energy tail of the distribution function. It is shown that the estimated current is independent of the injection temperature, whereas the statistical error shows a clear minimum where the injection distribution most closely resembles the actual distribution [P4].

The proposed backward Monte Carlo method is able to estimate the energy distribution function in a chosen point in the (\mathbf{r}, \mathbf{k}) phase space with the desired accuracy. The high-energy tail of the distribution can be calculated point-wise.

Chapter 5

Electron-Electron Scattering

In the previous chapter we presented a method to investigate the high-energy tail of the energy distribution. One particular scattering mechanism and its implications on the high energy tail of the energy distribution function is controversially discussed in the literature, namely electron-electron scattering (EES) [5, 10, 14, 15, 31, 32, 57, 79, 80, 103, 107] [P2].

One can distinguish between selfconsistent models which assume the actual or an approximate non-equilibrium distribution for the partner electrons, and non-selfconsistent models which assume an equilibrium distribution for the partner electrons. The latter approach is suitable to describe the interaction of channel hot electrons with a reservoir of cold electrons in the drain region of a MOSFET. This case is studied in the present thesis [P5].

Scattering due to a perturbation potential can be treated by Fermi's Golden rule, see Section 2.3. The essential term of Fermi's Golden rule is the matrix element of the perturbation potential.

5.1. Matrix Element

The perturbation potential for electron-electron scattering is caused by two-body screened Coulomb interaction. Assuming a three-dimensional electron gas (3DEG), the perturbation potential reads [11]:

$$U_s(\mathbf{r}_1, \mathbf{r}_2) = \frac{e^2}{4\pi\epsilon_s} \frac{e^{-\beta_s|\mathbf{r}_1-\mathbf{r}_2|}}{|\mathbf{r}_1 - \mathbf{r}_2|}, \quad (5.1)$$

5. Electron-Electron Scattering

where \mathbf{r}_1 and \mathbf{r}_2 are the spatial coordinates of the electrons and $1/\beta_s$ is the screening length also known as the *Debye length*, defined as [102]:

$$\beta_s^2 = \frac{e^2 n}{\epsilon_s k_B T}. \quad (5.2)$$

The electronic states for the electron-electron scattering are assumed to be plane-waves.

$$|\mathbf{k}_1, \mathbf{k}_2\rangle = \frac{1}{\Omega} e^{i\mathbf{k}_1 \cdot \mathbf{r}_1} e^{i\mathbf{k}_2 \cdot \mathbf{r}_2} \quad (5.3)$$

With these assumptions, the matrix element (2.24) can be written as:

$$\begin{aligned} M &= \langle \mathbf{k}'_1, \mathbf{k}'_2 | U_s | \mathbf{k}_1, \mathbf{k}_2 \rangle \\ &= \frac{e^2}{4\pi\epsilon_s} \frac{1}{\Omega^2} \int_{\Omega} d^3 r_1 \int_{\Omega} d^3 r_2 e^{-i(\mathbf{k}'_1 \cdot \mathbf{r}_1 + \mathbf{k}'_2 \cdot \mathbf{r}_2)} \frac{e^{-\beta_s |\mathbf{r}_1 - \mathbf{r}_2|}}{|\mathbf{r}_1 - \mathbf{r}_2|} e^{i(\mathbf{k}_1 \cdot \mathbf{r}_1 + \mathbf{k}_2 \cdot \mathbf{r}_2)} \end{aligned} \quad (5.4)$$

We define the spatial distance between the electrons as a new integration variable:

$$\mathbf{u} = \mathbf{r}_1 - \mathbf{r}_2, \quad (5.5)$$

In (5.4) the following substitutions are made:

$$\mathbf{r}_1 = \mathbf{r}_2 + \mathbf{u}, \quad d^3 r_1 = d^3 u. \quad (5.6)$$

This leads to following expression for the matrix element:

$$\langle \mathbf{k}'_1, \mathbf{k}'_2 | U_s | \mathbf{k}_1, \mathbf{k}_2 \rangle = \frac{e^2}{\epsilon_s} \frac{1}{\Omega^2} \int_{\Omega} \frac{e^{-\beta_s u}}{4\pi u} e^{i(\mathbf{k}_1 - \mathbf{k}'_1) \cdot \mathbf{u}} d^3 u \int_{\Omega} e^{i(\mathbf{k}_1 + \mathbf{k}_2 - \mathbf{k}'_1 - \mathbf{k}'_2) \cdot \mathbf{r}_2} d^3 r_2. \quad (5.7)$$

The first integral represents the Fourier transform of the screened Coulomb potential, see Appendix A.3:

$$\int_{R^3} \frac{e^{-\beta_s u}}{4\pi u} e^{i(\mathbf{k}_1 - \mathbf{k}'_1) \cdot \mathbf{u}} d^3 u = \frac{1}{|\mathbf{k}_1 - \mathbf{k}'_1|^2 + \beta_s^2}, \quad (5.8)$$

whereas the second integral results in a Kronecker-delta

$$\int_{\Omega} e^{i(\mathbf{k}_1 + \mathbf{k}_2 - \mathbf{k}'_1 - \mathbf{k}'_2) \cdot \mathbf{r}_2} d^3 r_2 = \Omega \delta_{\mathbf{k}_1 + \mathbf{k}_2, \mathbf{k}'_1 + \mathbf{k}'_2}, \quad (5.9)$$

which describes conservation of the total momentum

$$\mathbf{k}_1 + \mathbf{k}_2 = \mathbf{k}'_1 + \mathbf{k}'_2. \quad (5.10)$$

Due to the finite normalization volume Ω all wave vectors are discrete. Substituting (5.8) and (5.9) into (5.7) leads to the following expression for the matrix element [P5]:

$$\langle \mathbf{k}'_1, \mathbf{k}'_2 | U_s | \mathbf{k}_1, \mathbf{k}_2 \rangle = \frac{e^2}{\epsilon_s \Omega} \frac{\delta_{\mathbf{k}_1 + \mathbf{k}_2, \mathbf{k}'_1 + \mathbf{k}'_2}}{|\mathbf{k}_1 - \mathbf{k}'_1|^2 + \beta_s^2} \quad (5.11)$$

5.2. Two-particle Transition Rate

The transition rate from the initial state $|\mathbf{k}_1, \mathbf{k}_2\rangle$ to the final state $|\mathbf{k}'_1, \mathbf{k}'_2\rangle$ is expressed by Fermi's golden rule:

$$P(\mathbf{k}_1, \mathbf{k}_2, \mathbf{k}'_1, \mathbf{k}'_2) = \frac{2\pi}{\hbar} |\langle \mathbf{k}'_1, \mathbf{k}'_2 | U_s | \mathbf{k}_1, \mathbf{k}_2 \rangle|^2 \delta(E(\mathbf{k}'_1, \mathbf{k}'_2) - E(\mathbf{k}_1, \mathbf{k}_2)). \quad (5.12)$$

The total energy of state $|\mathbf{k}_1, \mathbf{k}_2\rangle$ is equal to $E(\mathbf{k}_1, \mathbf{k}_2) = \mathcal{E}(\mathbf{k}_1) + \mathcal{E}(\mathbf{k}_2)$. Inserting the matrix element (5.11) in (5.12), the transition rate becomes:

$$P_2(\mathbf{k}_1, \mathbf{k}_2, \mathbf{k}'_1, \mathbf{k}'_2) = \frac{2\pi}{\hbar} \left(\frac{e^2}{\epsilon_s \Omega} \right)^2 \frac{\delta_{\mathbf{k}_1 + \mathbf{k}_2, \mathbf{k}'_1 + \mathbf{k}'_2}}{(|\mathbf{k}_1 - \mathbf{k}'_1|^2 + \beta_s^2)^2} \delta[\mathcal{E}(\mathbf{k}'_1) + \mathcal{E}(\mathbf{k}'_2) - \mathcal{E}(\mathbf{k}_1) - \mathcal{E}(\mathbf{k}_2)]. \quad (5.13)$$

This derivation is based on the assumptions of a finite normalization volume Ω and the resulting discreteness of the \mathbf{k} -vectors. Thus, a Kronecker-delta is obtained, which is idempotent.

$$\delta_{\mathbf{k}_1 + \mathbf{k}_2, \mathbf{k}'_1 + \mathbf{k}'_2}^2 = \delta_{\mathbf{k}_1 + \mathbf{k}_2, \mathbf{k}'_1 + \mathbf{k}'_2} \quad (5.14)$$

5.2.1. Principle of Detailed Balance

In Section 4.1.2 we introduced a novel backward Monte Carlo method, which utilizes the principle of detailed balance. This section shows that the expression for electron-electron scattering also obeys the principle of detailed balance.

The transition rate (5.13) is conserving the total energy of the two particles involved. Thus, it describes an elastic scattering process. The principle of detailed balance states that for elastic processes the transition rate is symmetric [49, 62].

$$P_2(\mathbf{k}_1, \mathbf{k}_2, \mathbf{k}'_1, \mathbf{k}'_2) = P_2(\mathbf{k}'_1, \mathbf{k}'_2, \mathbf{k}_1, \mathbf{k}_2) \quad (5.15)$$

5. Electron-Electron Scattering

The symmetry property can be seen in the original definition of the transition rate:

$$P_2(\mathbf{k}_1, \mathbf{k}_2, \mathbf{k}'_1, \mathbf{k}'_2) = \frac{2\pi}{\hbar} |\langle \mathbf{k}'_1, \mathbf{k}'_2 | U_s | \mathbf{k}_1, \mathbf{k}_2 \rangle|^2 \delta[\mathcal{E}(\mathbf{k}'_1) + \mathcal{E}(\mathbf{k}'_2) - \mathcal{E}(\mathbf{k}_1) - \mathcal{E}(\mathbf{k}_2)] \quad (5.16)$$

Since both, the absolute value of the matrix element and the δ -function, are invariant under interchange of initial and final state, so is the transition rate.

5.3. Single-particle Transition Rate

The Monte Carlo methods described above estimate the solution of the Boltzmann equation, which is the single-particle distribution function. In order to stay in this single-particle framework, the two-particle scattering rate has to be reduced to a single-particle scattering rate. For this purpose, some assumptions about the distribution of the partner-electrons have to be made. These assumptions can vary from case to case. One can assume an equilibrium distribution or a more realistic self-consistent distribution for the partner electrons.

The total transition rate for a single-particle can be obtained by summing over all initial states \mathbf{k}_2 and final states \mathbf{k}'_2 of the partner electrons [P5].

$$P_1(\mathbf{k}_1, \mathbf{k}'_1) = \sum_{\mathbf{k}'_2} \sum_{\mathbf{k}_2} P_2(\mathbf{k}_1, \mathbf{k}_2, \mathbf{k}'_1, \mathbf{k}'_2) [1 - f(\mathbf{k}'_2)] 2f(\mathbf{k}_2) \quad (5.17)$$

Here, f is the distribution function of the partner electrons. The factor 2 in front of the distribution $f(\mathbf{k}_2)$ results from spin degeneracy. This means that, every state \mathbf{k}_2 can be occupied by two electrons. One summation in (5.17) can be evaluated using the Kronecker-delta. The other summation is converted to an integral taking into account the density of states, $\Omega/(2\pi)^3$. Therefore, the transition rate becomes

$$P_1(\mathbf{k}_1, \mathbf{k}'_1) = \frac{2\pi}{\hbar} \left(\frac{e^2}{\epsilon_s \Omega} \right)^2 \frac{\Omega}{(2\pi)^3} \times \int d^3k_2 \frac{\delta[\mathcal{E}(\mathbf{k}'_1) + \mathcal{E}(\mathbf{k}_1 + \mathbf{k}_2 - \mathbf{k}'_1) - \mathcal{E}(\mathbf{k}_1) - \mathcal{E}(\mathbf{k}_2)]}{(|\mathbf{k}_1 - \mathbf{k}'_1| + \beta_s^2)^2} \times [1 - f(\mathbf{k}_1 + \mathbf{k}_2 - \mathbf{k}'_1)] 2f(\mathbf{k}_2) \quad (5.18)$$

Additionally, we define the differential transition rate S .

$$S_1(\mathbf{k}_1, \mathbf{k}'_1) = \frac{\Omega}{(2\pi)^3} P_1(\mathbf{k}_1, \mathbf{k}'_1). \quad (5.19)$$

We define the momentum transfer \mathbf{q} as

$$\mathbf{q} = \mathbf{k}'_1 - \mathbf{k}_1 = \mathbf{k}_2 - \mathbf{k}'_2 \quad (5.20)$$

and introduce the function w .

$$w(\mathbf{k}_2, \mathbf{q}) = f(\mathbf{k}_2)[1 - f(\mathbf{k}_2 - \mathbf{q})] \quad (5.21)$$

Using these definitions, the differential transition rate (5.19) becomes

$$S_1(\mathbf{k}_1, \mathbf{k}_1 + \mathbf{q}) = \frac{2e^4}{(2\pi)^5 \hbar \epsilon_s^2} \int \frac{\delta[\mathcal{E}(\mathbf{k}_1 + \mathbf{q}) + \mathcal{E}(\mathbf{k}_2 - \mathbf{q}) - \mathcal{E}(\mathbf{k}_1) - \mathcal{E}(\mathbf{k}_2)]}{(q^2 + \beta_s^2)^2} w(\mathbf{k}_2, \mathbf{q}) d^3 k_2. \quad (5.22)$$

Note that S_1 is independent of the normalization volume Ω .

5.3.1. Spin Degeneracy and Normalization

The electron concentration n is given by:

$$n = \frac{2}{(2\pi)^3} \int f(\mathbf{k}) d^3 k \quad (5.23)$$

The factor 2 accounts for spin degeneracy. We introduce the normalized distribution function p_0 ,

$$p_0(\mathbf{k}) = \frac{f(\mathbf{k})}{\int f(\mathbf{k}) d^3 k} = \frac{2 f(\mathbf{k})}{(2\pi)^3 n} \quad (5.24)$$

and define \bar{w} as

$$\bar{w}(\mathbf{k}_2, \mathbf{q}) = p_0(\mathbf{k}_2)[1 - f(\mathbf{k}_2 - \mathbf{q})]. \quad (5.25)$$

Thus, the differential transition rate (5.22) becomes

$$S_1(\mathbf{k}_1, \mathbf{k}_1 + \mathbf{q}) = A \int \frac{\delta[\mathcal{E}(\mathbf{k}_1 + \mathbf{q}) + \mathcal{E}(\mathbf{k}_2 - \mathbf{q}) - \mathcal{E}(\mathbf{k}_1) - \mathcal{E}(\mathbf{k}_2)]}{(q^2 + \beta_s^2)^2} \bar{w}(\mathbf{k}_2, \mathbf{q}) d^3 k_2, \quad (5.26)$$

where the pre-factor A is of the form

$$A = \frac{ne^4}{(2\pi)^2 \hbar \epsilon_s^2}. \quad (5.27)$$

The transition rate is proportional to the electron density n and does not contain the spin degeneracy factor.

5. Electron-Electron Scattering

5.3.2. A Model for the Partner Electrons

The scattering rate (5.22) depends on the unknown distribution function $f(k)$. Therefore, a Boltzmann equation including this scattering rate will be nonlinear. In this work, the partner electrons are assumed to be in thermal equilibrium, described by the equilibrium distribution f_0 . The equilibrium distribution can be either a Fermi-Dirac or a Maxwell-Boltzmann distribution. With this assumption, the Boltzmann equation will be linear. This assumption is valid if hot carriers in the highly doped drain region are investigated. However, by fixing the distribution of the partner electron the heating of the partner electrons due to hot carriers is neglected.

Another assumption of our model is, that the cold partner electrons are described with a parabolic and isotropic dispersion relation.

$$\mathcal{E}(\mathbf{k}) = \frac{\hbar^2 \mathbf{k}^2}{2m} \quad (5.28)$$

Here, \mathbf{k} is the wavevector relative to the valley minimum located at \mathbf{k}_0

$$\mathbf{k} = \mathbf{k}_{FB} - \mathbf{k}_0, \quad (5.29)$$

where \mathbf{k}_{FB} represents the wave vector in the Brillouin zone, relative to the Γ -point.

5.3.3. Principle of Detailed Balance

In the single-particle picture, EES is no longer an elastic process. However, it can be shown that this process still satisfies the principle of detailed balance. With the following relation of the Fermi-Dirac distribution f_0

$$\frac{1 - f_0(\mathcal{E})}{f_0(\mathcal{E})} = e^{\beta(\mathcal{E} - E_F)} \quad (5.30)$$

the term of (5.17) can be reformulated as

$$[1 - f_0(\mathcal{E}'_2)] f_0(\mathcal{E}_2) = [1 - f_0(\mathcal{E}'_2)] [1 - f_0(\mathcal{E}_2)] e^{-\beta(\mathcal{E}_2 - E_F)}. \quad (5.31)$$

Using (5.31) and the energy balance equation

$$\mathcal{E}_2 = \mathcal{E}'_2 + \mathcal{E}'_1 - \mathcal{E}_1 \quad (5.32)$$

one can reformulate the transition rate (5.17) as

$$P_1(\mathbf{k}_1, \mathbf{k}'_1) = e^{\beta(\mathcal{E}_1 - \mathcal{E}'_1)} \sum_{\mathbf{k}_2, \mathbf{k}'_2} P_2(\mathbf{k}_1, \mathbf{k}_2, \mathbf{k}'_1, \mathbf{k}'_2) [1 - f_0(\mathcal{E}'_2)] [1 - f_0(\mathcal{E}_2)] e^{-\beta(\mathcal{E}'_2 - E_F)}. \quad (5.33)$$

5.3. Single-particle Transition Rate

In (5.33) we interchange the variables $\mathbf{k}_1, \mathbf{k}_2$ and $\mathbf{k}'_1, \mathbf{k}'_2$ and employ the symmetry property (5.15).

$$\begin{aligned} P_1(\mathbf{k}'_1, \mathbf{k}_1) &= e^{\beta(\mathcal{E}'_1 - \mathcal{E}_1)} \sum_{\mathbf{k}_2, \mathbf{k}'_2} P_2(\mathbf{k}'_1, \mathbf{k}'_2, \mathbf{k}_1, \mathbf{k}_2) [1 - f_0(\mathcal{E}_2)] [1 - f_0(\mathcal{E}'_2)] e^{-\beta(\mathcal{E}_2 - E_F)} \\ &= e^{\beta(\mathcal{E}'_1 - \mathcal{E}_1)} P_1(\mathbf{k}_1, \mathbf{k}'_1) \end{aligned} \quad (5.34)$$

This equation shows that P_1 satisfies the principle of detailed balance:

$$P_1(\mathbf{k}'_1, \mathbf{k}_1) e^{-\beta \mathcal{E}'_1} = P_1(\mathbf{k}_1, \mathbf{k}'_1) e^{-\beta \mathcal{E}_1}. \quad (5.35)$$

5.3.4. Angular Integration of the Transition Rate

The energy transfer of both involved particles is defined by

$$\Delta_1(\mathbf{k}_1, \mathbf{q}) = \mathcal{E}(\mathbf{k}_1 + \mathbf{q}) - \mathcal{E}(\mathbf{k}_1), \quad (5.36)$$

$$\Delta_2(\mathbf{k}_2, \mathbf{q}) = \mathcal{E}(\mathbf{k}_2 - \mathbf{q}) - \mathcal{E}(\mathbf{k}_2). \quad (5.37)$$

Thus, energy conservation of one scattering event can be formulated as

$$\Delta_1(\mathbf{k}_1, \mathbf{q}) + \Delta_2(\mathbf{k}_2, \mathbf{q}) = 0 \quad (5.38)$$

Note, that the equilibrium distribution $f_0(\mathcal{E})$ is a function of energy, and so is function \bar{w} , defined by (5.25).

$$\bar{w}_2(\mathcal{E}_2, \Delta_1) = p_0(\mathcal{E}_2) [(1 - f_0(\mathcal{E}_2 - \Delta_1))] \quad (5.39)$$

The transition rate (5.26) can be expressed in terms of Δ_1 and Δ_2 as follows:

$$S_1(\mathbf{k}_1, \mathbf{k}_1 + \mathbf{q}) = A \int \frac{\delta[\Delta_1(\mathbf{k}_1, \mathbf{q}) + \Delta_2(\mathbf{k}_2, \mathbf{q})]}{(q^2 + \beta_s^2)^2} \bar{w}_0(\mathcal{E}_2, \Delta_1) d^3 k_2. \quad (5.40)$$

The \mathbf{k}_2 -integration

$$I(\mathbf{k}_1, \mathbf{q}) = \int \delta[\Delta_1(\mathbf{k}_1, \mathbf{q}) + \Delta_2(\mathbf{k}_2, \mathbf{q})] \bar{w}_0(\mathcal{E}_2, \Delta_1) d^3 k_2 \quad (5.41)$$

can be evaluated in spherical polar coordinates, where \mathbf{q} is the polar axis. With the parabolic band approximation (5.28) the energy difference for the partner electron can be expressed as

$$\Delta_2(\mathbf{k}, \mathbf{q}) = \mathcal{E}(\mathbf{k}_2 - \mathbf{q}) - \mathcal{E}(\mathbf{k}_2) = \frac{\hbar^2}{2m} (q^2 - 2 k_2 q \cos \vartheta). \quad (5.42)$$

5. Electron-Electron Scattering

Substitution of (5.42) in (5.41) gives

$$I(\mathbf{k}_1, \mathbf{q}) = 2\pi \int_0^\pi d\vartheta \sin \vartheta \int_0^\infty dk_2 k_2^2 \delta \left[\Delta_1 + \frac{\hbar^2}{2m} \left(q^2 - 2 k_2 q \cos \vartheta_2 \right) \right] \bar{w}_0(\mathcal{E}_2, \Delta_1) \quad (5.43)$$

In the next step we substitute $\chi = \cos \vartheta$ and define the wave number κ as

$$\kappa = \frac{m}{\hbar^2} \frac{\Delta_1}{q} + \frac{q}{2}, \quad (5.44)$$

to obtain

$$I(\mathbf{k}_1, \mathbf{q}) = 2\pi \int_0^\infty dk_2 k_2^2 \bar{w}_0(\mathcal{E}_2, \Delta_1) \int_{-1}^1 \delta \left(\frac{\hbar^2 k_2 q}{m} \left(\frac{\kappa}{k_2} - \chi \right) \right) d\chi \quad (5.45)$$

The χ -integration can be carried out using the δ -function.

$$\begin{aligned} \int_{-1}^1 \delta \left(\frac{\hbar^2 k_2 q}{m} \left(\frac{\kappa}{k_2} - \chi \right) \right) d\chi &= \frac{m}{\hbar^2 q k_2} \int_{-1}^1 \delta \left(\frac{\kappa}{k_2} - \chi \right) d\chi \\ &= \frac{m}{\hbar^2 q k_2} (\Theta(\kappa + k_2) - \Theta(\kappa - k_2)) = \frac{m}{\hbar^2 q k_2} \Theta(k_2 - |\kappa|) \end{aligned} \quad (5.46)$$

Here, Θ is the unit step function. The integral (5.45) now simplifies to

$$I(\mathbf{k}_1, \mathbf{q}) = 2\pi \frac{m}{\hbar^2 q} \int_{|\kappa|}^\infty dk_2 k_2 \bar{w}_0(\mathcal{E}_2, \Delta_1). \quad (5.47)$$

The arguments \mathbf{k}_1 and \mathbf{q} enter the expression via the lower integration limit $|\kappa(\mathbf{k}_1, \mathbf{q})|$ and the argument Δ_1 . With (5.47), the transition rate (5.40) becomes:

$$S_1(\mathbf{k}_1, \mathbf{k}_1 + \mathbf{q}) = B \frac{\beta_s^2}{q (q^2 + \beta_s^2)^2} \int_{|\kappa|}^\infty \bar{w}_0(\mathcal{E}_2, \Delta_1) k_2 d^3 k_2, \quad (5.48)$$

with the pre-factor B defined as

$$B = 2\pi A \frac{m}{\hbar^2 \beta_s^2} = \frac{n e^4 m}{2\pi \hbar^3 \epsilon_s^2 \beta_s^2}. \quad (5.49)$$

5.3.5. Transition Rate for Boltzmann Statistics

To simplify notation we introduce the reduced Fermi energy η and the thermal wave number τ .

$$\eta = \beta E_F = \frac{E_F}{k_B T} \quad (5.50)$$

$$\tau^2 = \frac{2mk_B T}{\hbar^2} \quad (5.51)$$

To obtain the normalized distribution p_0 , one has to calculate the the normalization factor C_{MB} for the Maxwell-Boltzmann distribution, as shown in Appendix A.4.

$$p_0(\mathbf{k}) = \frac{f_0(\mathbf{k})}{C_{\text{MB}}} = \frac{e^{-k^2/\tau^2}}{\pi^{3/2}\tau^3} \quad (5.52)$$

Note, that the normalized Maxwell-Boltzmann distribution is independent of the Fermi level η . The integral in the partial evaluated transition rate (5.48) can be evaluated as shown in Appendix A.4:

$$\int_{|\kappa|}^{\infty} \bar{w}_0(\mathcal{E}_2, \Delta_1) k dk = \frac{e^{-\kappa^2/\tau^2}}{2\pi^{3/2}\tau} \quad (5.53)$$

Using (5.53) and denoting the final state as $\mathbf{k}'_1 = \mathbf{k}_1 + \mathbf{q}$, the equation of the transition rate (5.48) becomes:

$$S_1(\mathbf{k}_1, \mathbf{k}'_1) = \frac{C}{2\pi} \frac{\beta_s^2}{q(q^2 + \beta_s^2)^2} e^{-\kappa^2/\tau^2}, \quad (5.54)$$

with

$$q = |\mathbf{k}'_1 - \mathbf{k}_1| \quad \text{and} \quad (5.55)$$

$$C = \frac{\hbar}{\sqrt{2\pi} m k_B T} B. \quad (5.56)$$

From the definitions (5.44) and (5.51) we obtain

$$\frac{\kappa^2}{\tau^2} = \frac{\beta(E_q + \Delta_1)^2}{4E_q} \quad (5.57)$$

with

$$E_q = \frac{\hbar^2 q^2}{2m}.$$

Consequently, the transition rate (5.54) can be reformulated to:

$$S_1(\mathbf{k}_1, \mathbf{k}'_1) = \frac{C}{2\pi} \frac{\beta_s^2}{q(q^2 + \beta_s^2)^2} \times \exp\left(-\frac{(\mathcal{E}(\mathbf{k}'_1) - \mathcal{E}(\mathbf{k}_1) + E_q)^2}{4E_q k_B T}\right). \quad (5.58)$$

5. Electron-Electron Scattering

5.3.6. Transition Rate for Fermi Dirac Statistics

For Fermi Dirac statistics, the normalized distribution p_0 can be obtained by calculating the normalization factor C_{FD} , see Appendix A.5

$$p_0(\mathbf{k}) = \frac{f_0(\mathbf{k})}{C_{\text{FD}}} = \frac{1}{\pi^{3/2} \tau^3 \mathcal{F}_{1/2}(\eta) (e^{k^2/\tau^2 - \eta} + 1)} \quad (5.59)$$

where $\mathcal{F}_{1/2}$ denotes the Fermi integral of order 1/2. The integral in the partial evaluated transition rate (5.48) can be evaluated by substituting $\bar{w} = w/C_{\text{FD}}$ as shown in Appendix A.5:

$$\int_{|\kappa|}^{\infty} \bar{w}_0(\mathcal{E}_2, \Delta_1) k d^3k = \left(\frac{\tau^2 e^\eta}{2C_{\text{FD}}} \right) \frac{e^{-\eta}}{1 - e^{\beta\Delta_1}} \ln \left(\frac{1 + e^{\eta - \kappa^2/\tau^2}}{1 + e^{\eta + \beta\Delta_1 - \kappa^2/\tau^2}} \right) \quad (5.60)$$

With (5.60), the scattering rate (5.48) becomes

$$S_1(\mathbf{k}_1, \mathbf{k}_1 + \mathbf{q}) = \frac{C}{2\pi} \frac{e^\eta}{\mathcal{F}_{1/2}(\eta)} \frac{\beta_s^2}{q(q^2 + \beta_s^2)^2} \frac{e^{-\eta}}{1 - e^{\beta\Delta_1}} \ln \left(\frac{1 + e^{\eta - \kappa^2/\tau^2}}{1 + e^{\eta + \beta\Delta_1 - \kappa^2/\tau^2}} \right). \quad (5.61)$$

Finally, with the relations (5.57) and the relation

$$\frac{\kappa^2}{\tau^2} - \beta\Delta_1 = \frac{\beta(E_q - \Delta_1)^2}{4E_q}, \quad (5.62)$$

the scattering rate (5.61) can be reformulated to:

$$S_1(\mathbf{k}_1, \mathbf{k}_1 + \mathbf{q}) = \frac{C}{2\pi} \frac{e^\eta}{\mathcal{F}_{1/2}(\eta)} \frac{\beta_s^2}{q(q^2 + \beta_s^2)^2} \frac{e^{-\eta}}{1 - e^{\beta\Delta_1}} \ln \left(\frac{1 + e^{\eta - \frac{\beta(E_q + \Delta_1)^2}{4E_q}}}{1 + e^{\eta - \frac{\beta(E_q - \Delta_1)^2}{4E_q}}} \right) \quad (5.63)$$

Boltzmann Limit

For small carrier concentration the Boltzmann limit must be recovered. We consider the limit $\eta \rightarrow -\infty$. In this regime the Fermi-integral behaves as e^η . It holds

$$\lim_{\eta \rightarrow -\infty} \frac{e^\eta}{\mathcal{F}_{1/2}(\eta)} = 1. \quad (5.64)$$

The limit of the following expression is calculated using the rule of l'Hôpital.

$$\lim_{\eta \rightarrow -\infty} \frac{\ln \left(1 + e^{\eta - \kappa^2/\tau^2} \right) - \ln \left(1 + e^{\eta + \beta\Delta_1 - \kappa^2/\tau^2} \right)}{e^\eta} = \quad (5.65)$$

$$\lim_{x \rightarrow 0} \frac{\ln \left(1 + x e^{-\kappa^2/\tau^2} \right) - \ln \left(1 + x e^{\beta\Delta_1 - \kappa^2/\tau^2} \right)}{x} = e^{-\kappa^2/\tau^2} (1 - e^{\beta\Delta_1}) \quad (5.66)$$

Taking these limits, the scattering rate (5.61) simplifies to the Boltzmann result (5.54).

5.4. Implementation for Full-Band Structures

Up to this point, no assumption about $\mathcal{E}(\mathbf{k}_1)$, the dispersion relation of the primary electron, has been made. This fact allows us to construct a model in which for the high-energetic primary electron a full-band structure, as described in Section 2.1.4, is assumed. For the low-energetic partner electron the parabolic band approximation is used, as shown in the previous sections.

5.4.1. Total Scattering Rate

The total scattering rate Γ_1 is obtained by integration of the scattering rate (5.59) or (5.63) over the final states of the sample electron:

$$\Gamma_1(\mathbf{k}_1) = \int S(\mathbf{k}_1, \mathbf{k}'_1) d^3k'_1 \quad (5.67)$$

The integral in (5.67) is approximated by a discrete sum in \mathbf{k} -space.

$$\Gamma_1(\mathbf{k}_n, N_n) \approx \sum_m^{N_n} S(\mathbf{k}_n, \mathbf{k}_m) V_m \quad (5.68)$$

Here, \mathbf{k}_m and V_m denote the center and the volume of the m -th tetrahedron, respectively. Whereas \mathbf{k}_n denotes a discrete point in \mathbf{k} -space.

The contributions of all neighboring tetrahedra of tetrahedron n are calculated and stored in a table. Recursively, all neighbors of these contributing tetrahedra are included in this table, see Fig. 5.1. The recursive search for contributing neighbors ends, when a tetrahedron contributes less than a pre-defined tolerance to the total scattering rate. The number of all tetrahedra found in this way for one particular point \mathbf{k}_n is defined as N_n .

5.4.2. Obtaining the Final State

To enable the selection of the after-scattering state, all partial sums of the form

$$\Gamma_1(\mathbf{k}_n, N) = \sum_m^N S(\mathbf{k}_n, \mathbf{k}_m) V_m, \quad N \in [1, N_n] \quad (5.69)$$

are pre-computed and stored in a table [P5]. This table of the partial sums (5.69) is stored for each discrete initial state \mathbf{k}_n in the irreducible wedge of the Brillouin

5. Electron-Electron Scattering

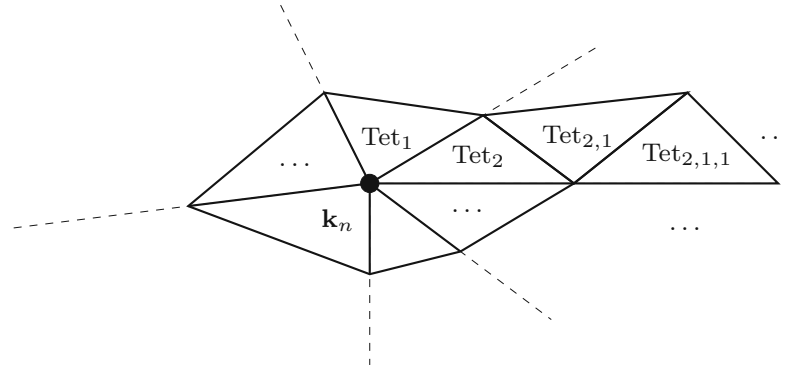


Figure 5.1.: All contributing neighbors of a point \mathbf{k}_n are recursively included. In the first step, all direct neighbours are added. For the second and third step, the tetrahedrons $\text{Tet}_{2,1}$ and $\text{Tet}_{2,1,1}$, respectively, are exemplarily illustrated. For the calculation of the scattering rate, all tetrahedra are represented by the center \mathbf{k}_m and their volume V_m .

zone, for each band b , and for a set of discrete Fermi levels E_F in the case of Fermi-Dirac statistics.

The final state is obtained by first, randomly selecting a tetrahedron $N \in [1, N_n]$ using the pre-computed table of partial sums.

$$\Gamma_1(\mathbf{k}_n, N - 1) \leq r < \Gamma_1(\mathbf{k}_n, N) \quad (5.70)$$

The uniformly distributed random number r is in the range

$$0 \leq r \leq \Gamma_1(\mathbf{k}_n, N_n). \quad (5.71)$$

Once a tetrahedron has been selected, a uniformly-distributed random state inside the tetrahedron is chosen using Barycentric coordinates.

Barycentric Coordinates for a Tetrahedron

A tetrahedron has four vertices $\{V_0, V_1, V_2, V_3\}$. The barycentric coordinates $\{\xi_0, \xi_1, \xi_2, \xi_3\}$ of a point P inside the tetrahedron can be calculated as [19]:

$$\xi_i = \frac{\text{volume}(P, V_{(i+1) \bmod 4}, V_{(i+2) \bmod 4}, V_{(i+3) \bmod 4})}{\text{volume}(V_i, V_{(i+1) \bmod 4}, V_{(i+2) \bmod 4}, V_{(i+3) \bmod 4})}. \quad (5.72)$$

Because of the condition

$$\sum_{i=0}^3 \xi_i = 1, \quad (5.73)$$

one coordinate is redundant.

Random Selection of a Point inside a Tetrahedron

A uniformly distributed random point inside a tetrahedron can be obtained by randomly chosen barycentric coordinates [81].

$$\xi_0 = r_0 \tag{5.74}$$

$$\xi_1 = r_1 (1 - \xi_0) \tag{5.75}$$

$$\xi_2 = r_2 (1 - \xi_0 - \xi_1) \tag{5.76}$$

$$\xi_3 = 1 - \xi_0 - \xi_1 - \xi_2 \tag{5.77}$$

Here, r_i are uniformly distributed random numbers in $[0, 1[$.

5.5. Implementation for Parabolic and Isotropic Bands

The next model we want to discuss assumes a parabolic dispersion for both the sample and the partner electron, which is the standard model often used in literature. Some integrals can be solved analytically if a parabolic and isotropic dispersion relation is assumed for the sample electrons:

$$\mathcal{E}(\mathbf{k}_1) = \frac{\hbar^2 \mathbf{k}_1^2}{2m}. \quad (5.78)$$

5.5.1. The Total Scattering Rate for Boltzmann Statistics

The total scattering rate is defined as

$$\Gamma_1(\mathbf{k}_1) = \int S(\mathbf{k}_1, \mathbf{k}_1 + \mathbf{q}) d^3 q. \quad (5.79)$$

We use formulation (5.54) and introduce spherical polar coordinates with \mathbf{k}_1 defining the polar axis.

$$\Gamma_1(\mathbf{k}_1) = \frac{C}{2\pi} \int_0^\infty \int_0^\pi \frac{\beta_s^2}{q(q^2 + \beta_s^2)^2} \exp \left[- \left(\frac{q + k_1 \cos \vartheta_1}{\tau} \right)^2 \right] 2\pi \sin \vartheta_1 d\vartheta_1 q^2 dq \quad (5.80)$$

Here, we make use of the relation

$$\kappa(\mathbf{k}_1, \mathbf{q}) = q - k_1 \cos \vartheta_1.$$

Defining $\chi = \cos \vartheta_1$ and the scaled variables

$$p = \frac{k_1}{\tau}, \quad s = \frac{q}{\tau}, \quad \gamma = \frac{\beta_s}{\tau} \quad (5.81)$$

we obtain

$$\Gamma_1(\mathbf{k}_1) = C \int_0^\infty \int_{-1}^1 \frac{\gamma^2 s}{(s^2 + \gamma^2)^2} e^{-(s+p\chi)^2} d\chi ds. \quad (5.82)$$

The double integral defines a function $F(p, \gamma)$:

$$F(p, \gamma) = \int_0^\infty \int_{-1}^1 \frac{\gamma^2 s}{(s^2 + \gamma^2)^2} e^{-(s+p\chi)^2} d\chi ds. \quad (5.83)$$

5.5. Implementation for Parabolic and Isotropic Bands

Evaluating the χ -integral will result in an error function. However, by applying integration by parts in s the error function can be avoided. We use

$$\int_0^{\infty} \frac{\partial u}{\partial s} v \, ds = u v \Big|_{s=0}^{\infty} - \int_0^{\infty} u \frac{\partial v}{\partial s} \, ds \quad (5.84)$$

where $\frac{\partial u}{\partial s}$ and v are defined as:

$$\begin{aligned} \frac{\partial u(s, \gamma)}{\partial s} &= \frac{\gamma^2 s}{(s^2 + \gamma^2)^2} \\ v(p, s, \chi) &= e^{-(s+p\chi)^2} \end{aligned}$$

For the antiderivative u and the partial derivative of v we find:

$$\begin{aligned} u(s, \gamma) &= \int_0^s \frac{\gamma^2 \bar{s}}{(\bar{s}^2 + \gamma^2)^2} \, d\bar{s} = \frac{s^2}{2(s^2 + \gamma^2)} \\ \frac{\partial v}{\partial s} &= -2(s + p\chi) e^{-(s+p\chi)^2} = \frac{1}{p} \frac{\partial v}{\partial \chi} \end{aligned}$$

Inserting these expression in (5.84) gives

$$\int_0^{\infty} \frac{\partial u}{\partial s} v \, ds = -\frac{1}{p} \int_0^{\infty} u \frac{\partial v}{\partial \chi} \, ds$$

Now integration over χ can be carried out.

$$F(p, \gamma) = -\frac{1}{p} \int_0^{\infty} ds \int_{-1}^1 u \frac{\partial v}{\partial \chi} \, d\chi = \frac{1}{p} \int_0^{\infty} u(s, \gamma) [v(p, s, -1) - v(p, s, 1)] \, ds$$

Back substitution of the functions u and v gives

$$F(p, \gamma) = \frac{1}{2p} \int_0^{\infty} \frac{s^2}{s^2 + \gamma^2} \left(e^{-(s-p)^2} - e^{-(s+p)^2} \right) \, ds \quad (5.85)$$

The asymptotic behavior of $F(p, \gamma)$ is discussed in Appendix A.5.2

$$F(0, 0) = 1.$$

5. Electron-Electron Scattering

With back substitution of p and τ , the single-particle scattering can be reformulated to

$$\Gamma_1(\mathcal{E}) = C F \left(\sqrt{\mathcal{E}/k_B T}, \beta_s/\tau \right). \quad (5.86)$$

The pre-factor C (5.56) with (5.49) reads

$$C = \frac{ne^4}{(2\pi)^{3/2} \hbar^2 \epsilon_s^2 \beta_s^2} \sqrt{\frac{m}{k_B T}} \quad (5.87)$$

Inserting the definition of β_s^2 (5.2), the pre-factor C becomes independent of the electron density n .

$$C = \frac{ne^4}{(2\pi)^{3/2} \hbar^2 \epsilon_s^2} \frac{\epsilon_s k_B T}{e^2 n} \sqrt{\frac{m}{k_B T}} = \frac{e^2 \sqrt{m k_B T}}{(2\pi)^{3/2} \hbar^2 \epsilon_s} \quad (5.88)$$

The electron-electron scattering rate only depends on the electron density through the screening parameter $\gamma = \beta_s/\tau$ in the function F . Since γ shows up in the denominator of the integral in F , the electron-electron scattering decreases at higher electron concentrations.

5.5.2. Two-particle Scattering Rate for Boltzmann Statistics

In the previous section the total scattering rate was calculated by integrating the scattering rate $S(\mathbf{k}_1, \mathbf{k}'_1)$. The latter is the result of another integration. Thus the total scattering rate is obtained by two consecutive integrations. Inserting (5.26) in (5.79) and assuming Boltzmann statistics gives

$$\Gamma_1(\mathbf{k}_1) = A \int \frac{\delta[\mathcal{E}(\mathbf{k}_1 + \mathbf{q}) + \mathcal{E}(\mathbf{k}_2 - \mathbf{q}) - \mathcal{E}(\mathbf{k}_1) - \mathcal{E}(\mathbf{k}_2)]}{(q^2 + \beta_s^2)^2} p_0(\mathbf{k}_2) d^3 k_2 d^3 q \quad (5.89)$$

In this section we reverse the order of integration and perform the \mathbf{q} -integration first. The result of the first integration is the two-particle scattering rate $\Gamma_2(\mathbf{k}_1, \mathbf{k}_2)$.

$$\Gamma_2(\mathbf{k}_1, \mathbf{k}_2) = A \int \frac{\delta[\mathcal{E}(\mathbf{k}_1 + \mathbf{q}) + \mathcal{E}(\mathbf{k}_2 - \mathbf{q}) - \mathcal{E}(\mathbf{k}_1) - \mathcal{E}(\mathbf{k}_2)]}{(q^2 + \beta_s^2)^2} p_0(\mathbf{k}_2) d^3 q \quad (5.90)$$

For a parabolic band the argument of the δ -function in (5.90) becomes

$$\begin{aligned} \mathcal{E}(\mathbf{k}_1 + \mathbf{q}) - \mathcal{E}(\mathbf{k}_1) + \mathcal{E}(\mathbf{k}_2 - \mathbf{q}) - \mathcal{E}(\mathbf{k}_2) &= \frac{\hbar^2}{2m} ((\mathbf{k}_1 + \mathbf{q})^2 + (\mathbf{k}_2 - \mathbf{q})^2 - \mathbf{k}_1^2 - \mathbf{k}_2^2) \\ &= \frac{\hbar^2}{m} (q^2 + (\mathbf{k}_1 - \mathbf{k}_2) \cdot \mathbf{q}) = \frac{\hbar^2}{m} (q^2 - Kq \cos \vartheta). \end{aligned} \quad (5.91)$$

5.5. Implementation for Parabolic and Isotropic Bands

Here we have introduced the difference vector \mathbf{K} defined as

$$\mathbf{K} = \mathbf{k}_2 - \mathbf{k}_1, \quad (5.92)$$

and ϑ , the angle between \mathbf{K} and \mathbf{q} . In a spherical polar coordinate system, with \mathbf{K} as the polar axis and ϑ as the polar angle, the energy conservation requires a positive $\cos \vartheta$

$$q^2 - qK \cos \vartheta = 0 \quad \Rightarrow \quad \cos \vartheta = \frac{q}{K} \geq 0. \quad (5.93)$$

Since $q = |\mathbf{q}|$ and $K = |\mathbf{K}|$ are positive by definition the allowed range of ϑ is

$$\vartheta \in \left[0, \frac{\pi}{2}\right].$$

With (5.91) the integral (5.90) becomes

$$\Gamma_2(\mathbf{k}_1, \mathbf{k}_2) = A \int_0^\infty \int_0^{\pi/2} \frac{\delta\left[\frac{\hbar^2}{m}(q^2 - Kq \cos \vartheta)\right]}{(q^2 + \beta_s^2)^2} 2\pi \sin \vartheta \, d\vartheta \, q^2 \, dq$$

We carry out the ϑ -integration first. Defining $\xi = \cos \vartheta$ we obtain

$$\begin{aligned} H(q) &= \int_0^1 \delta\left(\frac{\hbar^2}{m}q(q - K\xi)\right) d\xi \\ &= \frac{m}{\hbar^2 q} \int_0^1 \delta(K\xi - q) d\xi = \frac{m}{\hbar^2 K q} \left[\Theta(K - q) - \underbrace{\Theta(-q)}_0 \right] \end{aligned} \quad (5.94)$$

Note that $H(q)$ restricts the domain of integration to $q \in [0, K]$.

$$\Gamma_2(\mathbf{k}_1, \mathbf{k}_2) = 2\pi A \int_0^\infty \frac{q^2}{(q^2 - \beta_s^2)^2} H(q) \, dq = 2\pi A \frac{m}{\hbar^2 K} \int_0^K \frac{q^2}{(q^2 - \beta_s^2)^2} \, dq \quad (5.95)$$

With the pre-factor B (5.49), the scattering rate can be evaluated as [100]:

$$\Gamma_2(\mathbf{k}_1, \mathbf{k}_2) = \frac{B}{2} \frac{K}{K^2 + \beta_s^2}. \quad (5.96)$$

5. Electron-Electron Scattering

5.5.3. Single-particle Scattering Rate for Boltzmann Statistics

Having evaluated the \mathbf{q} -integral in (5.89), we now evaluate the \mathbf{k}_2 -integral. The single-particle scattering rate Γ_1 can be calculated by integrating the two-particle scattering rate Γ_2 against the normalized probability density $p_0(\mathbf{k}_2)$, see [100].

$$\Gamma_1(\mathbf{k}_1) = \int \Gamma_2(\mathbf{k}_1, \mathbf{k}_2) p_0(\mathbf{k}_2) d^3 k_2 = \frac{B}{2} \int \frac{|\mathbf{k}_2 - \mathbf{k}_1|}{|\mathbf{k}_2 - \mathbf{k}_1|^2 + \beta_s^2} \frac{f_0(\mathbf{k}_2)}{C_{MB}} d^3 k_2 \quad (5.97)$$

The variable substitution

$$\mathbf{K} = \mathbf{k}_2 - \mathbf{k}_1, \quad d^3 k_2 = d^3 K, \quad \mathbf{k}_2 = \mathbf{k}_1 + \mathbf{K}$$

leads to the following expression for the single-particle scattering rate

$$\Gamma_1(\mathbf{k}_1) = \frac{B}{2C_{MB}} \int \frac{K}{K^2 + \beta_s^2} f_0(\mathbf{k}_1 + \mathbf{K}) d^3 K. \quad (5.98)$$

Introducing scaled variables

$$p = \frac{k_1}{\tau}, \quad s = \frac{K}{\tau}, \quad \gamma = \frac{\beta_s}{\tau},$$

the Boltzmann term can be reformulated as

$$f_0(\mathbf{k}_1 + \mathbf{K}) = e^{\eta - (k_1^2 + 2k_1 K \cos \vartheta + K^2)/\tau^2} = e^{\eta - p^2 - s^2 - 2ps \cos \vartheta} \quad (5.99)$$

the \mathbf{K} -integral in (5.98) can be evaluated analytically:

$$\begin{aligned} \int \frac{K}{K^2 + \beta_s^2} f_0(\mathbf{k}_1 + \mathbf{K}) d^3 K &= \tau^2 e^\eta \int \frac{s}{s^2 + \gamma^2} e^{-p^2 - s^2 - 2ps \cos \vartheta} d^3 s \\ &= 2\pi\tau^2 e^\eta \int_0^\infty \frac{s}{s^2 + \gamma^2} e^{-s^2 - p^2} s^2 ds \int_{-1}^1 e^{-2ps\chi} d\chi \\ &= 2\pi\tau e^\eta \int_0^\infty \frac{s^2}{s^2 + \gamma^2} \frac{e^{-(s-p)^2} - e^{-(s+p)^2}}{2p} ds \\ &= 2\pi\tau^2 e^\eta F(p, \gamma) \end{aligned} \quad (5.100)$$

The function $F(p, \gamma)$ is defined in (5.85), which leads finally to the single-particle scattering rate (5.86).

5.5.4. Random Selection of the Momentum Transfer \mathbf{q}

In the first step the wave vector \mathbf{k}_2 of the partner electron is selected randomly from an equilibrium Maxwellian distribution. With the current wave vector \mathbf{k}_1 of the sample electron the difference vector is computed

$$\mathbf{K} = \mathbf{k}_2 - \mathbf{k}_1, \quad K = |\mathbf{K}|.$$

The two-particle scattering rate can be used to calculate the momentum transfer \mathbf{q} . For this purpose the integrand in (5.95) can be used as a probability density for q . We define $F(q)$ as:

$$F(q) = \int_0^q \frac{\bar{q} d\bar{q}}{(\bar{q}^2 + \beta_s^2)^2} = \frac{q^2}{2\beta_s^2(q^2 + \beta_s^2)} \quad (5.101)$$

The normalized cumulative probability distribution is

$$P(q) = \frac{F(q)}{F(K)}, \quad q \in [0, K]. \quad (5.102)$$

The random number q is generated using the inversion method, see Section 3.3.2.

$$P(q_r) = r_1 \quad \Rightarrow \quad q_r^2 = \frac{r_1 K^2 \beta_s^2}{K^2(1 - r_1) + \beta_s^2}$$

The polar angle ϑ_r is given by (5.93):

$$\cos \vartheta_r = \frac{q_r}{K}. \quad (5.103)$$

With a second random number r_2 the azimuthal angle φ is generated from a uniform distribution in $[0, 2\pi]$.

$$\varphi_r = 2\pi r_2 \quad (5.104)$$

From $(q_r, \cos \vartheta_r, \varphi_r)$ the 3D vector \mathbf{q}_r can be constructed. Note that the polar axis is given by the difference vector $\mathbf{K} = \mathbf{k}_2 - \mathbf{k}_1$. In the last step the final state is computed.

$$\mathbf{k}'_1 = \mathbf{k}_1 + \mathbf{q}_r \quad (5.105)$$

5.6. Results and Discussion

The following results and discussion are taken from a previous work [P5].

5.6.1. Screened Coulomb Scattering Mechanisms

Since ionized-impurity scattering (IIS) and e-e scattering (EES) are caused by the very same screened Coulomb interaction, we compare the rates of these two scattering mechanisms in Fig. 5.2 and Fig. 5.3. For this comparison we used the IIS model of Brooks and Herring (BH)

$$\Gamma_{\text{BH}}(\mathbf{k}) = \frac{N_I e^4 m}{4\pi \hbar^3 \epsilon^2 \beta_s^2} \frac{4k}{\beta_s^2 + 4k^2} = \frac{B}{2} \frac{4k}{\beta_s^2 + 4k^2} \quad (5.106)$$

Here, B is the already defined pre-factor (5.49) and N_I is the ionized impurity concentration. In both cases, the scattering rate becomes smaller with increasing concentration. However, since the scattering potential gets more localized with stronger screening, its distribution in momentum space gets wider, and hence the momentum transferred per scattering event gets larger. At high energies, the rates become concentration-independent in both cases. The main differences can be observed at low energies. While an electron at rest is strongly affected by the moving partner electrons, it will not be affected by the static impurities. At low energies, the EES rate assumes a constant value determined by $F(0, x)$, whereas the IIS rate vanishes for a non-zero screening parameter β_s . For weak screening ($\beta_s \rightarrow 0$) the EES rate converges to a finite value determined by $F(0, 0) = 1$, whereas the maximum of the IIS rate grows indefinitely, see Fig. 5.3.

5.6.2. Results for Bulk Silicon

As a first test, the equilibrium distribution function is simulated. We assume a parabolic dispersion, which is consistent with the integration of the transition rate (5.19). This results in an equilibrium distribution function, represented by a Maxwellian, also in the presence of EES. This is expected since EES satisfies the principle of detailed balance. The numbers of energy gain and loss processes are perfectly balanced for each scattering mechanism. Using the transition rate (5.58) in an MC simulation with a non-parabolic dispersion ($\alpha = 0.5 \text{ eV}^{-1}$), however, results in an imbalance of energy gain and loss processes. An excess of phonon emissions over absorptions indicates that the inconsistently used EES model provides net energy to the electron system.

This example indicates that the analytical formula derived for a parabolic dispersion should not be used in a transport model with any other dispersion.

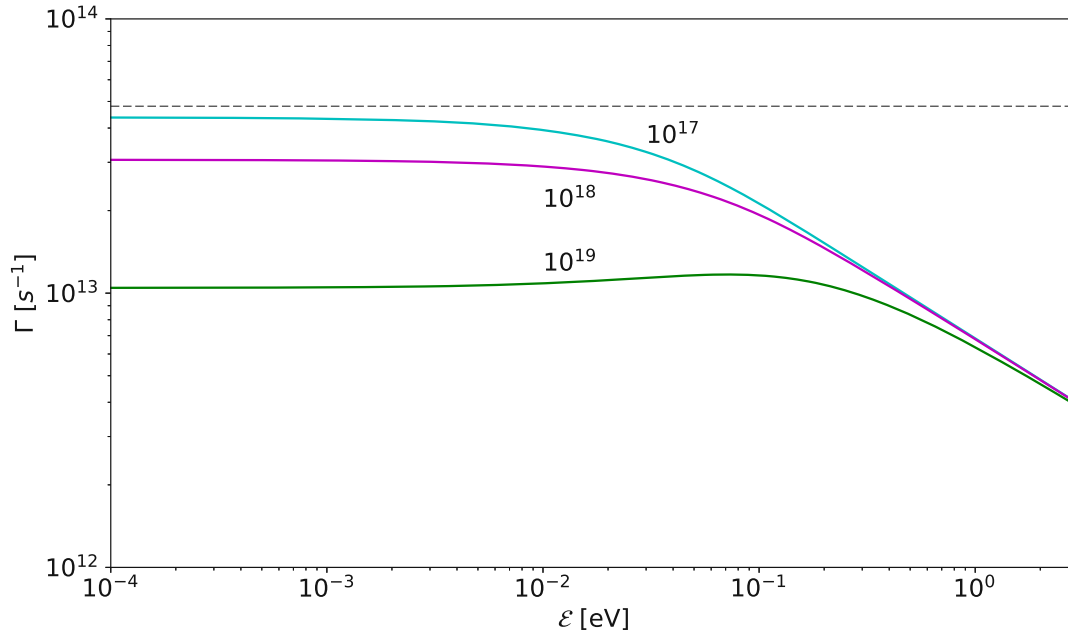


Figure 5.2.: Electron-electron scattering rate calculated from (5.86) assuming $m = 0.3m_0$, $\epsilon_s = 11.68\epsilon_0$ and $T = 300K$ and the electron concentrations $n = 10^{17}/10^{18}/10^{19} \text{ cm}^{-3}$. The dashed line represents the unscreened limit of the scattering rate.

5.6.3. Results for an $n^+n^-n^+$ Diode

The EES model has been implemented in the Monte Carlo device simulator VMC [109] for both analytical and numerical band structures. The first device investigated is an $n^+n^-n^+$ diode with abrupt junctions. The doping levels are 10^{19} cm^{-3} and 10^{15} cm^{-3} , respectively. Fig. 5.4 shows the conduction band edge for an applied voltage of 2 V and the electron densities. The plot distinguishes between the total electron density (S+D) and the density of electrons originating from the source contact only (S). Fig. 5.5 shows the energy relaxation process due to phonon scattering only (dotted lines) and due to phonon and EES (solid lines). In the drain region ($x \geq 400 \text{ nm}$), the difference between the decay of the mean energy due to scattering only (magenta lines) and due to mixing with the cold carriers from the drain contact (cyan lines) can be observed.

5. Electron-Electron Scattering

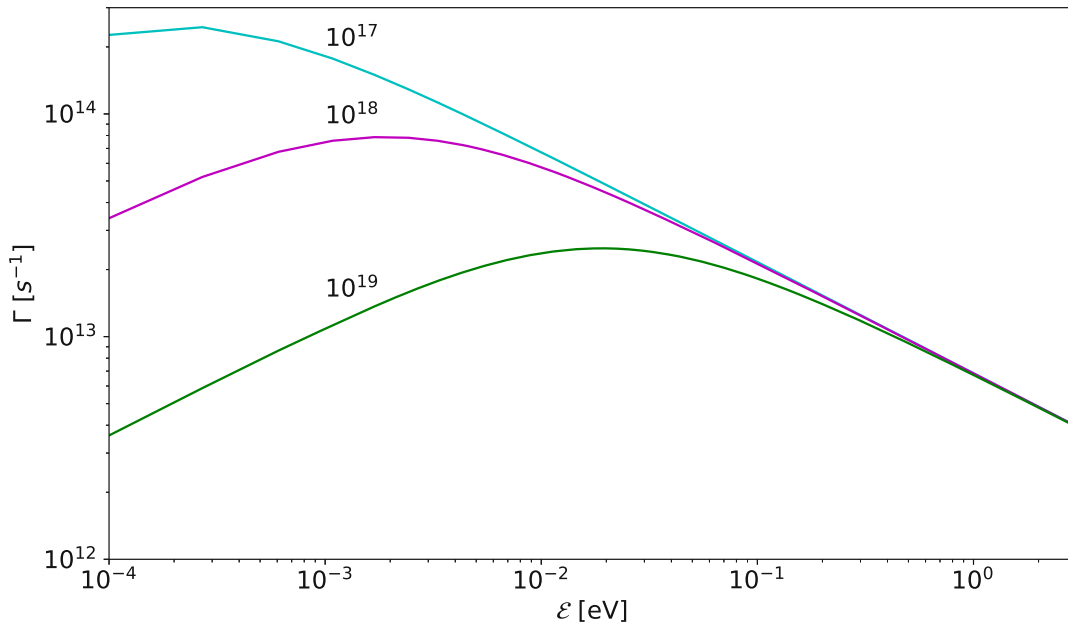


Figure 5.3.: Ionized-impurity scattering rate obtained from the Brooks-Herring model [43] for the same parameters as in Fig. 5.2.

5.6.4. Results for a n-channel MOSFET

The second device we consider is a planar n-channel MOSFET with $L_G = 65$ nm, $t_{\text{ox}} = 2.5$ nm, and a channel width of $W = 1 \mu\text{m}$. Device geometry and doping profiles have been obtained by process simulation [104]. The first simulation uses the parabolic band approximation. Fig. 5.6 shows the EDF at three interface points in the channel at $V_{GS} = 2.2$ V and $V_{DS} = 2.2$ V. Fig. 5.6 indicates that EES has virtually no influence on the non-equilibrium EDF. The reason is that the EES transition rate (5.19) assumes the interaction with an equilibrium electron system and thus does not alter the Maxwellian high energy tail.

The full-band implementation of the EES model in the MC code requires a numerical integration over the Brillouin zone. Fermi-Dirac statistics for the initial state and the Pauli blocking factor for the final state of the partner electron are taken into account. The state after scattering is selected randomly using pre-calculated lists. To resolve the high energy tail accurately, we employ the backward MC method, described in Chapter 4.

In Fig. 5.7 results from full-band transport calculations are compared to the results of ViennaSHE, a deterministic solver for the BTE based on a spherical

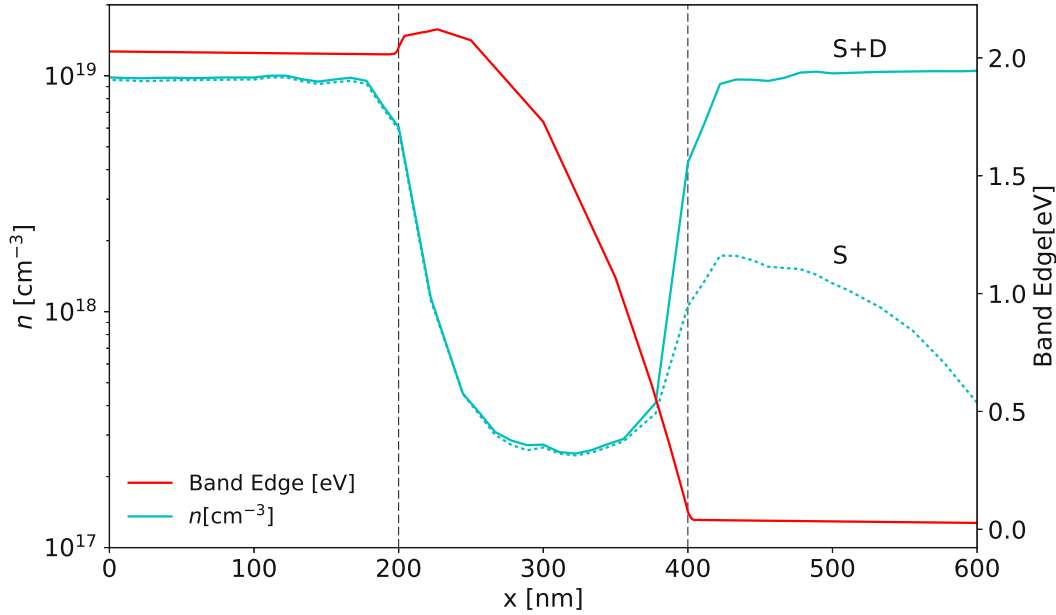


Figure 5.4.: Conduction band edge in a $n^+n^-n^+$ diode with abrupt junctions. The total electron density (S+D) and the partial density due to electrons injected from the source contact (S) are shown.

harmonics expansion of the distribution function [4, 63, 85, 108]. ViennaSHE accounts for an isotropic, multi-valley band-structure that captures some features of the full-band density of states. It is also able to take EES into account. In the EES model of ViennaSHE, additional approximations are introduced. For instance, the energy of the partner electron before scattering is treated as a constant (\mathcal{E}^*) which is set equal to the average energy. As shown in Fig. 5.7, the MC model predicts a Maxwellian tail at high energies by the assumption that the hot carriers interact with an equilibrium system of cold carriers, whereas the EES model of ViennaSHE predicts a significant deviation from the Maxwellian tail. We believe that an EES model that adequately fulfills energy and momentum conservation simultaneously would not be able to yield such strong enhancements of the high energy tail as reported in [5, 15, 104].

5. Electron-Electron Scattering

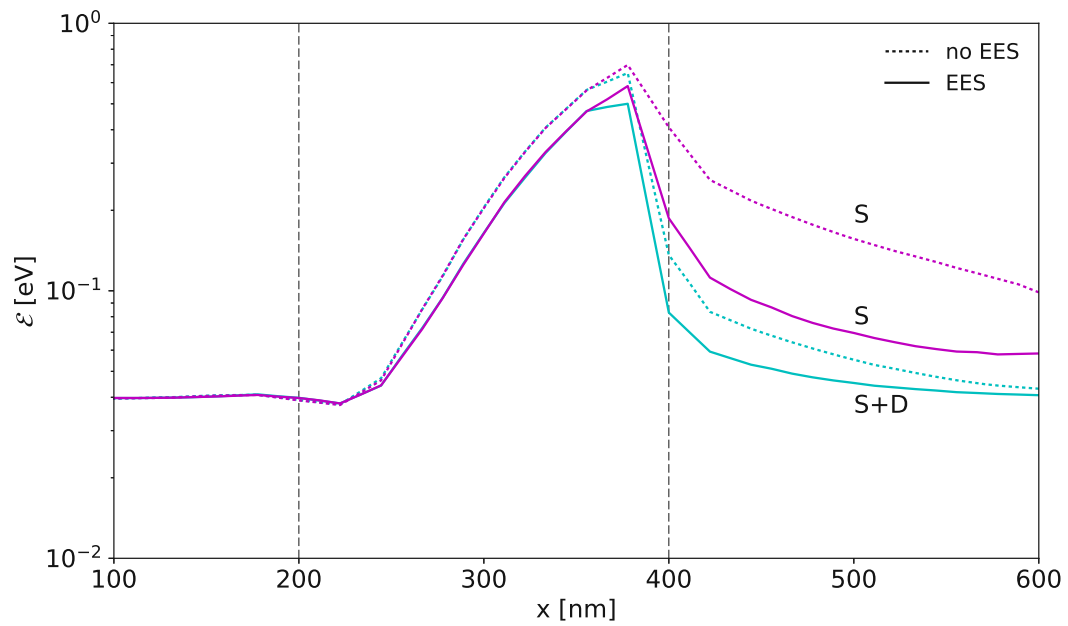


Figure 5.5.: Average electron energy in the $n^+n^-n^+$ diode. The upper curves (S) consider only the (hot) electrons originating from the source region and clearly show the additional energy relaxation due to EES. The lower curves (S+D) consider all electrons and show a stronger carrier cooling because in addition to energy relaxation there occurs also a mixing of the hot carriers with the cold carriers in the drain.

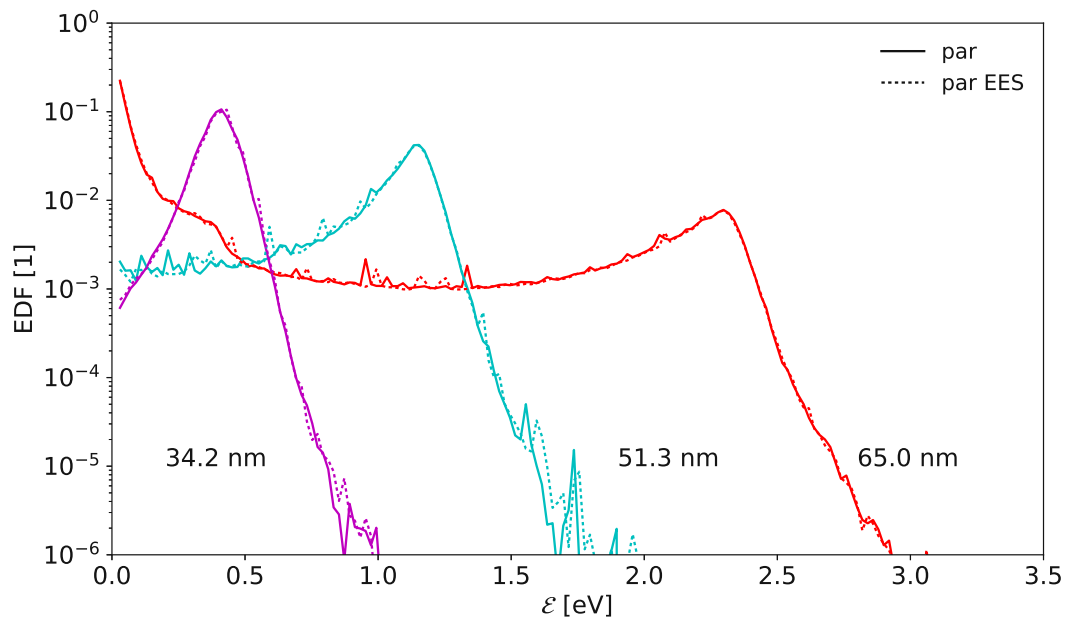


Figure 5.6.: EDF at three surface points in the channel of a MOSFET with and without EES. A parabolic dispersion is assumed in the transport model to be consistent with the EES-rate (5.86).

5. Electron-Electron Scattering

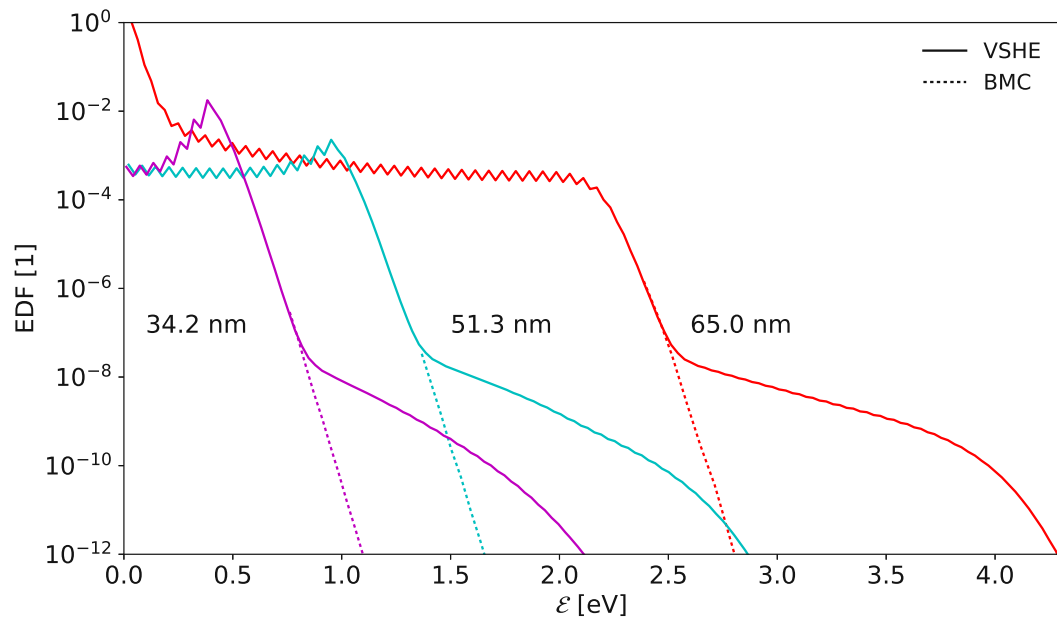


Figure 5.7.: EDF at three surface points in the channel with EES and fullband effects included. The backward MC simulation accounts for interaction with cold drain electrons and predicts a Maxwellian tail (dashed line). ViennaSHE considers interaction with non-equilibrium electrons at fixed energy and severely overestimates the high-energy tail.

Chapter 6

Outlook and Conclusion

This chapter shall discuss possible future implementations and improvements of the work done in this theses. Finally, a conclusion is drawn.

6.1. Possible Further Improvements of the BMC Method

Some of these possible improvements can be applied to the classical MC algorithm, such as using materials other than silicon, additional hole transport or other scattering processes. The self-consistent simulation can be achieved by coupling with a drift-diffusion simulator or with the ensemble MC algorithm. One improvement which could be applied to the BMC method is a combination of the stable and the unstable version of the algorithm.

6.1.1. Combination of Methods

The fact that in the original versions of the BMC algorithm particles tend to higher energies [45, 73] has led to problems, see Section 4.1.2. Thus, the algorithms were unstable. Contrarily, particles in the stable version of the algorithm [62] tend to lower energies. These considerations and their tendency for energy loss/gain are sketched in Fig. 4.3 and Fig. 4.4.

A novel idea for improvement would combine these two methods to keep the particles in a derived energy range shown in Fig. 6.1. This could lead to a significant improvement regarding the variance reduction in this specific energy range. Thus, this combination of methods could be an interesting tool to investigate processes

6. Outlook and Conclusion

which are more likely to occur in a particular energy range or have an energy threshold.

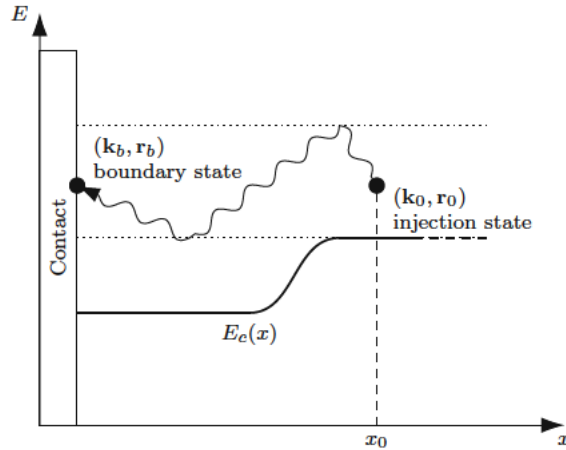


Figure 6.1.: Combination of the approaches in Fig. 4.3 and Fig. 4.4.

6.2. Possible Further Improvements for the EES

In the current implementation of the EES, the mixing of hot and cold carriers is described. This approximation is valid in the drain region, where the hot electrons from the channel are mixing with the cold electrons in the drain. In order to scatter electrons with a more realistic distribution, a novel two particle MC algorithm could be implemented. This two particle algorithm was already implemented and tested for bulk silicon. The extension to the space-dependent case has yet to be developed [41]. With this novel algorithm, the effect of EES on the high-energy-tail can be investigated not only in the drain region but also in the channel of a MOSFET.

6.3. Conclusion

This thesis covers the basics of the semi-classic transport theory in semiconductors. It covers different types of band-structure models and how to calculate them, it shows the limitation of the semi-classical transport theory and introduces the BTE, which is most commonly used to describe semi-classical transport in semiconductors.

The result of the BTE is a distribution function (DF). With this DF defined in k -space, r -space and time, every other quantity of interest can be calculated. There are three different methods shown, which are used to obtain approximate

solutions of the BTE. One method is based on the moments of the BTE. Taking only two moments into account, the method of moments yield to the drift-diffusion (DD) model. The second method discussed in this work is the spherical harmonics expansion (SHE) method. The solution of the BTE is obtained deterministically. The third method discussed is the Monte Carlo (MC) method. Based on the stochastic nature of the physical processes the solution of the BTE is obtained by MC estimates. Advantages and drawbacks of all three methods have been discussed.

The backward MC (BMC) method was proposed to overcome some drawbacks of the forward MC method [45, 62, 73]. Here, we established a stable BMC estimator based on [62] and developed several novel techniques such as symmetric injection to further reduce variance. All derived estimators were implemented in a pre-existing MC device simulator. We show that the implementations could fulfill all proposed predictions and lead to tremendous variance reduction for rare events in MC simulations. Thus, it is possible to only simulate the DF in one specific region of interest or in other words: one can choose the energy and the location in the device and estimate the DF for this point only. Thus, only the trajectories passing this specific point have to be considered and no other trajectories have to be calculated. The advantage of using full-bands, physical scattering mechanisms, and the possibility to only estimate the results of interest make the BMC method a powerful tool for investigating hot-carrier effects.

We took some effort to establish a formalism to describe EES for two particles as well as for single particles. This formalism was derived in general, and implemented with full-bands and with the parabolic band approximation. Furthermore, it was shown that the transition rates obey the principle of detailed balance. Thus, no altering of the DF's high energy tail is expected. In order to compare it to results from an SHE simulator in the drain region, the single-particle scattering model assumes that the hot-electrons get mixed in the drain with an ensemble of electrons in thermal equilibrium. With partner electrons in equilibrium and parabolic bands for both, the sample and the partner electrons, the non-self-consistent results show no altering of the distribution function's high energy tail.

The good compatibility with the standard algorithms for scattering and free-flight makes the BMC method very smooth to implement in existing MC simulators. The implemented version of the BMC method appears to be a powerful tool for investigating rare events in general and hot-carrier effects in particular. Transport across high energy barriers or physical processes with high energy thresholds can be investigated more easily than with other methods. This work shows that the BMC algorithm has no problems with high energy barriers when it comes to the calculation of the current. Moreover, the results even show a slight decrease in simulation time by increasing barrier heights. The algorithm proves to be sta-

6. Outlook and Conclusion

ble, no matter of the injection distribution that can be chosen freely. Of course, the more realistic the injection distribution, the smaller the statistical error of the estimation. Furthermore, the BMC method is able to estimate quantities with a high energy threshold such as the acceleration integral used in hot-carrier degradation modeling. With our EES method, we showed that the investigation of effects affecting hot-carrier distribution including full-bands is possible with the BMC method.

Appendix A

Integration over the Brillouin Zone

A.1. The partition function

This section is based on a previous work [P3]. The partition function [74] defined by (3.58) is evaluated by numerical integration. The contribution of band n is given by

$$Z_n = \int_{\text{BZ}} e^{-\beta \mathcal{E}_n(\mathbf{k})} d^3 k \quad (\text{A.1})$$

In VMC, only the irreducible wedge of the BZ is decomposed into M tetrahedra. One octant of the BZ can be represented by six mirroring operations of the irreducible wedge. In this case the partition function is calculated as

$$Z_n = 48 \sum_{m=1}^M \int_{\text{Tet } m} e^{-\beta \mathcal{E}_n(\mathbf{k})} d^3 k, \quad (\text{A.2})$$

The integration over the irreducible wedge is now split into integrals over tetrahedra which can be performed using barycentric coordinates [P3]. The values of the attributes are given at the vertices of the tetrahedron. A linear interpolation of the values inside the tetrahedron is assumed. $\{\mathcal{E}_0, \mathcal{E}_1, \mathcal{E}_2, \mathcal{E}_3\}$ are the energy values in the tetrahedron vertices and V_m is the volume of the m^{th} tetrahedron. From

A. Integration over the Brillouin Zone

the following integral

$$\begin{aligned}
\int_{\text{Tet } m} e^{-\beta \mathcal{E}(\mathbf{k})} d^3k &= V_m \int_0^1 d\xi_0 \int_0^{1-\xi_0} d\xi_1 \int_0^{1-\xi_0-\xi_1} d\xi_2 e^{-\beta(\xi_0(\mathcal{E}_0-\mathcal{E}_3)+\xi_1(\mathcal{E}_1-\mathcal{E}_3)+\xi_2(\mathcal{E}_2-\mathcal{E}_3)+\mathcal{E}_3)} \\
&= V_m \int_0^1 d\xi_0 \int_0^{1-\xi_0} d\xi_1 \frac{1}{\beta(\mathcal{E}_2-\mathcal{E}_3)} \left(e^{-\beta(\xi_0(\mathcal{E}_0-\mathcal{E}_3)+\xi_1(\mathcal{E}_1-\mathcal{E}_3)+\mathcal{E}_3)} \right. \\
&\quad \left. - e^{-\beta(\xi_0(\mathcal{E}_0-\mathcal{E}_2)+\xi_1(\mathcal{E}_1-\mathcal{E}_2)+\mathcal{E}_2)} \right) \\
&= V_m \int_0^1 d\xi_0 \frac{1}{\beta^2(\mathcal{E}_2-\mathcal{E}_3)(\mathcal{E}_1-\mathcal{E}_2)} \left(e^{-\beta(\xi_0(\mathcal{E}_0-\mathcal{E}_1)+\mathcal{E}_1)} - e^{-\beta(\xi_0(\mathcal{E}_0-\mathcal{E}_2)+\mathcal{E}_2)} \right) \\
&\quad - \frac{1}{\beta^2(\mathcal{E}_2-\mathcal{E}_3)(\mathcal{E}_1-\mathcal{E}_3)} \left(e^{-\beta(\xi_0(\mathcal{E}_0-\mathcal{E}_1)+\mathcal{E}_1)} - e^{-\beta(\xi_0(\mathcal{E}_0-\mathcal{E}_3)+\mathcal{E}_3)} \right) \\
&= V_m \sum_{i=0}^3 \frac{e^{-\beta \mathcal{E}_i}}{\beta^3 \prod_{\substack{j=0 \\ j \neq i}}^3 (\mathcal{E}_j - \mathcal{E}_i)} \tag{A.3}
\end{aligned}$$

follows that

$$Z = \sum_n Z_n = 48 \sum_n \sum_m V_m \sum_{i=0}^3 \frac{e^{-\beta \mathcal{E}_i}}{\beta^3 \prod_{\substack{j=0 \\ j \neq i}}^3 (\mathcal{E}_j - \mathcal{E}_i)} \tag{A.4}$$

The special case where $\mathcal{E}_j = \mathcal{E}_i$ is discussed in the next section.

A.2. Average Energy and Injection Velocity

The statistical average (3.59) can be calculated with the band-structure given in the irreducible wedge and decomposed in M tetrahedra, as follows:

$$\langle A \rangle = \frac{48}{Z} \sum_n \sum_{m=1}^M \int_{\text{Tet } m} A_n(\mathbf{k}) e^{-\beta \mathcal{E}_n(\mathbf{k})} d^3k. \tag{A.5}$$

$\{A_0, A_1, A_2, A_3\}$ are the attribute values in the tetrahedron vertices. The following derivation assumes a linear variation of the attribute and the energy in the

A.2. Average Energy and Injection Velocity

tetrahedron.

$$\begin{aligned}
 \int_{\text{Tet } m} A(\mathbf{k}) e^{-\beta \mathcal{E}(\mathbf{k})} d^3 k &= V_m \int_0^1 d\xi_0 \int_0^{1-\xi_0} d\xi_1 \int_0^{1-\xi_0-\xi_1} d\xi_2 (\xi_0 (A_0 - A_3) + \xi_1 (A_1 - A_3) \\
 &\quad + \xi_2 (A_2 - A_3) + A_3) e^{-\beta(\xi_0(\mathcal{E}_0 - \mathcal{E}_3) + \xi_1(\mathcal{E}_1 - \mathcal{E}_3) + \xi_2(\mathcal{E}_2 - \mathcal{E}_3) + \mathcal{E}_3)} \\
 &= V_m \sum_{i=0}^3 \frac{e^{-\beta \mathcal{E}_i} \left(A_i + \sum_{\substack{j=0 \\ j \neq i}}^3 \left(\frac{A_j - A_i}{\beta(\mathcal{E}_j - \mathcal{E}_i)} \right) \right)}{\beta^3 \prod_{\substack{j=0 \\ j \neq i}}^3 (\mathcal{E}_j - \mathcal{E}_i)} \tag{A.6}
 \end{aligned}$$

The statistical averages (A.5) becomes

$$\langle A \rangle = \frac{48}{Z} \sum_n \sum_m V_m \sum_{i=0}^3 \frac{e^{-\beta \mathcal{E}_i} \left(A_i + \sum_{\substack{j=0 \\ j \neq i}}^3 \left(\frac{A_j - A_i}{\beta(\mathcal{E}_j - \mathcal{E}_i)} \right) \right)}{\beta^3 \prod_{\substack{j=0 \\ j \neq i}}^3 (\mathcal{E}_j - \mathcal{E}_i)}. \tag{A.7}$$

If the attribute of interest is the energy, $A(k) = \mathcal{E}(k)$, the average gets reduced to

$$\langle \mathcal{E} \rangle = \frac{48}{Z} \sum_n \sum_m V_m \sum_{i=0}^3 \frac{e^{-\beta \mathcal{E}_i} \left(\frac{3}{\beta} + \mathcal{E}_i \right)}{\beta^3 \prod_{\substack{j=0 \\ j \neq i}}^3 (\mathcal{E}_j - \mathcal{E}_i)}. \tag{A.8}$$

In the case where the desired attribute is the injection velocity, $A(k) = |v_x(k)|$ which is constant in each tetrahedron, the average (4.30) is reduced to

$$\langle |v_x| \rangle = \frac{48}{Z} \sum_n \sum_m V_m |v_{x,m}| \sum_{i=0}^3 \frac{e^{-\beta \mathcal{E}_i}}{\beta^3 \prod_{\substack{j=0 \\ j \neq i}}^3 (\mathcal{E}_j - \mathcal{E}_i)}, \tag{A.9}$$

where $v_{x,m}$ is the constant velocity in x -direction in the tetrahedron with the index m . Because of symmetry, the absolute value has to be used, otherwise the result would be zero.

A. Integration over the Brillouin Zone

In the special case where $\mathcal{E}_i = \mathcal{E}_k$ the expression for the average energy can be written as:

$$\langle \mathcal{E} \rangle = \frac{48}{Z} \sum_n \sum_m V_m \sum_{i=0}^3 \frac{e^{-\beta \mathcal{E}_i} \left(\frac{3}{\beta} + \mathcal{E}_i \right)}{\beta^2 \prod_{\substack{j=0 \\ j \neq i \\ j \neq k}}^3 (\mathcal{E}_j - \mathcal{E}_i)}, \quad (\text{A.10})$$

because of the limit

$$\lim_{\Delta \rightarrow 0} \frac{1 - e^{-\beta \Delta}}{\Delta} = \beta. \quad (\text{A.11})$$

A.3. Fourier Transform of the Screened Coulomb Potential

The Fourier Transform of the screened Coulomb potential

$$V(u) = \frac{e^{-\beta_s u}}{4\pi u}$$

is defined as

$$\tilde{V}(\mathbf{q}) = \int d^3u \frac{e^{-\beta_s u}}{4\pi u} e^{-i \mathbf{q} \cdot \mathbf{u}}.$$

Introducing spherical polar coordinates, with \mathbf{q} defining the polar axis,

$$\mathbf{q} \cdot \mathbf{u} = q u \cos \theta \quad \text{and} \quad \cos \theta = \chi,$$

the integral can be solved as follows:

$$\begin{aligned} \tilde{V}(\mathbf{q}) &= \frac{1}{2} \int_0^\infty du u^2 \frac{e^{-\beta_s u}}{u} \int_{-1}^1 d\chi e^{-i q u \chi} = \frac{1}{2} \int_0^\infty du u^2 \frac{e^{-\beta_s u}}{u} \left[\frac{e^{-i q u \chi}}{q u} \right]_{-1}^1 \\ &= \frac{\pi}{2q} \int_0^\infty du \left[e^{-(\beta_s + i q) u} - e^{-(\beta_s - i q) u} \right] = \frac{1}{\beta_s^2 + q^2} \end{aligned}$$

A.4. The Normalized Maxwell-Boltzmann Distribution

The normalization factor for Maxwell-Boltzmann statistics and parabolic bands is defined as follows:

$$C_{\text{MB}} = \int f_0(\mathbf{k}) d^3 k = \int e^{(E_F - \mathcal{E}(\mathbf{k}))/k_B T} d^3 k \quad (\text{A.12})$$

Introducing scaled variables (5.50) and (5.51) the integral becomes:

$$\begin{aligned} C_{\text{MB}} &= e^\eta \int_0^\infty e^{-k^2/\tau^2} 4\pi k^2 dk = 2\pi \tau^3 e^\eta \int_0^\infty e^{-z} z^{1/2} dz \\ &= 2\pi \tau^3 e^\eta \underbrace{\Gamma(3/2)}_{\sqrt{\pi}/2} = \pi^{3/2} \tau^3 e^\eta \end{aligned} \quad (\text{A.13})$$

The last integral on the right-hand side defines the Gamma function:

$$\Gamma(3/2) = \frac{\sqrt{\pi}}{2}. \quad (\text{A.14})$$

A.4.1. Evaluating the Transition Rate Integral

With the normalized Boltzmann distribution p_0 , the integral in the transition rate (5.48) can be evaluated as follows:

$$\begin{aligned} \int_{|\kappa|}^\infty \bar{w}_0(\mathcal{E}_2, \Delta_1) k dk &= \int_{|\kappa|}^\infty p_0(\mathcal{E}) k dk = \frac{1}{C_{\text{MB}}} \int_{|\kappa|}^\infty e^{\eta - k^2/\tau^2} k dk \\ &= \frac{\tau^2 e^\eta}{C_{\text{MB}}} \int_{|\kappa|/\tau}^\infty e^{-u^2} u du = \frac{\tau^2 e^\eta}{2 C_{\text{MB}}} \int_{|\kappa|^2/\tau^2}^\infty e^{-z} dz \\ &= \frac{e^{-\kappa^2/\tau^2}}{2\pi^{3/2} \tau} = \frac{\hbar e^{-\kappa^2/\tau^2}}{(2\pi)^{3/2} \sqrt{m k_B T}} \end{aligned} \quad (\text{A.15})$$

A.5. The Normalized Fermi-Dirac Distribution

The normalization factor for Fermi-Dirac statistics is defined as:

$$\begin{aligned} C_{\text{FD}} &= \int f_0(\mathbf{k}) d^3k = \int_0^\infty \frac{4\pi k^2}{e^{k^2/\tau^2 - \eta} + 1} dk = 4\pi \tau^3 \int_0^\infty \frac{u^2}{e^{u^2 - \eta} + 1} du \\ &= 2\pi \tau^3 \int_0^\infty \frac{z^{1/2}}{e^{z - \eta} + 1} dz = 2\pi \tau^3 \underbrace{\Gamma(3/2)}_{\sqrt{\pi}/2} \mathcal{F}_{1/2}(\eta) = \pi^{3/2} \tau^3 \mathcal{F}_{1/2}(\eta) \end{aligned} \quad (\text{A.16})$$

Here, $\mathcal{F}_{1/2}$ denotes the Fermi integral of order $1/2$. The Fermi integral of order j is defined as:

$$\mathcal{F}_j(x) = \frac{1}{\Gamma(j+1)} \int_0^\infty \frac{z^j}{e^{z-x} + 1} dz \quad (\text{A.17})$$

A.5.1. Evaluating the Transition Rate Integral

Substituting $\bar{w}_0 = w_0/C_{\text{FD}}$, the integral in the transition rate (5.48) can be rearranged as follows:

$$\int_{|\kappa|}^\infty \bar{w}_0(\mathcal{E}_2, \Delta_1) k dk = \left(\frac{\tau^2 e^\eta}{2C_{\text{FD}}} \right) \int_{|\kappa|}^\infty e^{-\eta} w_0(\mathcal{E}_2, \Delta_1) \frac{2k}{\tau^2} dk \quad (\text{A.18})$$

Using the relation (5.30), the function w can be reformulated as

$$\begin{aligned} w_0(\mathcal{E}_2, \Delta_1) &= f_{\text{FD}}(\mathcal{E}_2) [1 - f_{\text{FD}}(\mathcal{E}_2 - \Delta_1)] \\ &= f_{\text{FD}}(\mathcal{E}_2) f_{\text{FD}}(\mathcal{E}_2 - \Delta_1) e^{\beta(\mathcal{E}_2 - \Delta_1 - E_F)} \end{aligned} \quad (\text{A.19})$$

With the variable substitutions

$$d_1 = \beta\Delta_1, \quad u = \frac{k^2}{\tau^2}, \quad du = \frac{2k}{\tau^2} dk, \quad u_1 = \frac{\kappa^2}{\tau^2},$$

the integral in (A.18) can be evaluated in the manner of:

$$\begin{aligned} I &= \int_{|\kappa|}^\infty e^{-\eta} w_0(\mathcal{E}_2, \Delta_1) \frac{2k}{\tau^2} d^3k = \int_{|\kappa|}^\infty \frac{e^{k^2/\tau^2 - \beta\Delta_1 - 2\eta}}{(e^{k^2/\tau^2 - \eta} + 1)(e^{k^2/\tau^2 - \beta\Delta_1 - \eta} + 1)} \frac{2k}{\tau^2} dk \\ &= \int_{u_1}^\infty \frac{e^{u - d_1 - 2\eta}}{(e^{u - \eta} + 1)(e^{u - d_1 - \eta} + 1)} du = e^{-\eta} \int_{u_1}^\infty \frac{e^{\eta - u}}{(1 + e^{\eta - u})(1 + e^{\eta + d_1 - u})} du \end{aligned} \quad (\text{A.20})$$

With the further substitutions

$$\begin{aligned} v &= e^{\eta-u}, & v_1 &= v(u_1) = e^{\eta-\kappa^2/\tau^2}, & v_2 &= v(\infty) = 0, \\ dv &= -e^{\eta-u} du, & a &= e^{d_1}, \end{aligned} \quad (\text{A.21})$$

the integral gets transformed to:

$$\begin{aligned} I &= e^{-\eta} \int_0^{v_1} \frac{1}{(1+v)(1+av)} dv = \frac{e^{-\eta}}{1-a} [\ln(1+v_1) - \ln(1+av_1)] \\ &= \frac{e^{-\eta}}{1-e^{d_1}} \left[\ln(1+e^{\eta-\kappa^2/\tau^2}) - \ln(1+e^{\eta+d_1-\kappa^2/\tau^2}) \right] = \frac{e^{-\eta}}{1-e^{d_1}} \ln \left(\frac{1+e^{\eta-\kappa^2/\tau^2}}{1+e^{\eta+d_1-\kappa^2/\tau^2}} \right) \end{aligned} \quad (\text{A.22})$$

A.5.2. Asymptotic behaviour of EES

$F(p, \gamma)$ at low Energies

With the relation

$$\frac{e^x - e^{-x}}{2} = \sinh x$$

the formula (5.85) can be rewritten to

$$F(p, \gamma) = \frac{e^{-p^2}}{p} \int_0^{\infty} \frac{s^2}{s^2 + \gamma^2} \sinh(2ps) e^{-s^2} ds, \quad (\text{A.23})$$

where the limit for $p \rightarrow 0$ can be obtained. With the relation

$$\lim_{p \rightarrow 0} \frac{\sinh 2ps}{2ps} = 1 \quad (\text{A.24})$$

the limit of $F(p \rightarrow 0, \gamma)$ becomes

$$F(p \rightarrow 0, \gamma) = 2 \int_0^{\infty} \frac{s^3}{s^2 + \gamma^2} e^{-s^2} ds = \int_0^{\infty} \frac{u}{u + \gamma^2} e^{-u} du \quad (\text{A.25})$$

With the substitution $t = u + \gamma^2$ and $x = \gamma^2$ the integral can be reformulated

$$F(p \rightarrow 0, x) = e^x \left(\int_x^{\infty} \frac{e^{-t}}{t} dt - x \int_x^{\infty} \frac{e^{-t}}{t} dt \right) = 1 + x e^x \text{Ei}(-x). \quad (\text{A.26})$$

Here, Ei denotes the exponential integral function. This result shows that also an electron with zero kinetic energy ($p = 0$) is affected by e-e scattering.

A. Integration over the Brillouin Zone

$F(p, \gamma)$ at low Concentrations

From the formula (5.85) the limit for $\gamma \rightarrow 0$ can be obtained. In this case, the concentration n is zero and therefore there is no screening.

$$\begin{aligned} F(p, \gamma \rightarrow 0) &= \frac{1}{2p} \int_0^\infty \left(e^{-(s-p)^2} - e^{-(s+p)^2} \right) ds = \frac{1}{2p} \left(\int_{-p}^\infty e^{-t^2} dt - \int_p^\infty e^{-t^2} dt \right) \\ &= \frac{1}{2p} \int_{-p}^p e^{-t^2} dt = \frac{\sqrt{\pi}}{2p} \operatorname{erf}(p) \end{aligned} \quad (\text{A.27})$$

The function $\operatorname{erf}(x)$ denotes the error function

$$\operatorname{erf}(x) = \frac{2}{\sqrt{\pi}} \int_0^x e^{-t^2} dt. \quad (\text{A.28})$$

Setting $\gamma = 0$ in (A.25), the asymptotic maximum of the function $F(p, \gamma)$ can be derived

$$F(0, 0) = \int_0^\infty e^{-u} du = 1. \quad (\text{A.29})$$

Bibliography

- [1] N. Ashcroft and N. Mermin. *Solid State Physics*. New York: Holt, Rinehart and Winston, 1976. ISBN: 9780030839931.
- [2] G. Baccarani. *Process and device modeling for microelectronics*. Elsevier, 1993. ISBN: 9780444899620.
- [3] G. Baccarani, M. Rudan, R. Guerrieri, and P. Ciampolini. “Process and Device Modeling”. In: ed. by W. L. Engl. Amsterdam, The Netherlands, The Netherlands: North-Holland Publishing Co., 1986. Chap. Physical Models for Numerical Device Simulation, pp. 107–158. ISBN: 0-444-87891-2. URL: <http://dl.acm.org/citation.cfm?id=21927.24382>.
- [4] M. Bina, K. Rupp, S. Tyaginov, O. Triebel, and T. Grasser. “Modeling of hot carrier degradation using a spherical harmonics expansion of the bipolar Boltzmann transport equation”. In: *2012 International Electron Devices Meeting*. Dec. 2012, pp. 30.5.1–30.5.4.
- [5] M. Bina, S. Tyaginov, J. Franco, K. Rupp, Y. Wimmer, D. Osintsev, B. Kaczer, and T. Grasser. “Predictive Hot-Carrier Modeling of n-Channel MOSFETs”. In: *IEEE Transactions on Electron Devices* 61.9 (2014), 3103–3110. ISSN: 0018-9383. DOI: 10.1109/TED.2014.2340575.
- [6] M. Bina. “Charge Transport Models for Reliability Engineering of Semiconductor Devices”. PhD thesis. Technische Universität Wien, 2014.
- [7] F. Bloch. “Über die Quantenmechanik der Elektronen in Kristallgittern”. In: *Zeitschrift für Physik* 52.7 (July 1929), pp. 555–600. ISSN: 0044-3328. DOI: 10.1007/BF01339455. URL: <https://doi.org/10.1007/BF01339455>.
- [8] K. Blotekjaer. *High-frequency Conductivity, Carrier Waves, and Acoustic Amplification in Drifted Semiconductor Plasmas*. Defense Technical Information Center, 1966.
- [9] S. Brandt. *Datenanalyse: Mit statistischen Methoden und Computerprogrammen*. Spektrum Akademischer Verlag, 1999. ISBN: 9783827401588.

Bibliography

- [10] A. Bravaix, C. Guerin, V. Huard, D. Roy, J. M. Roux, and E. Vincent. “Hot-Carrier acceleration factors for low power management in DC-AC stressed 40nm NMOS node at high temperature”. In: *2009 IEEE International Reliability Physics Symposium*. Apr. 2009, pp. 531–548. DOI: 10.1109/IRPS.2009.5173308.
- [11] K. F. Brennan. *The Physics of Semiconductors*. Cambridge University Press, 1999.
- [12] G. Casella, C. P. Robert, and M. T. Wells. “Generalized Accept-Reject sampling schemes”. In: *A Festschrift for Herman Rubin*. Ed. by A. DasGupta. Vol. Volume 45. Lecture Notes–Monograph Series. Beachwood, Ohio, USA: Institute of Mathematical Statistics, 2004, pp. 342–347. DOI: 10.1214/lnms/1196285403. URL: <https://doi.org/10.1214/lnms/1196285403>.
- [13] R. Chambers. “The Kinetic Formulation of Conduction Problems”. In: *Proc. Phys. Soc. (London)* A65 (1952), pp. 458–459.
- [14] M. Y. Chang, D. W. Dyke, C. C. C. Leung, and P. A. Childs. “High-energy electron–electron interactions in silicon and their effect on hot carrier energy distributions”. In: *Journal of Applied Physics* 82 (1997), p. 2974.
- [15] P. A. Childs and C. C. C. Leung. “A one-dimensional solution of the Boltzmann transport equation including electron–electron interactions”. In: *Journal of Applied Physics* 79 (1996), p. 222.
- [16] M. Cohen and V. Heine. “Cancellation of Kinetic and Potential Energy in Atoms, Molecules, and Solids”. In: *Physical Review* 122 (6 June 1961), pp. 1821–1826. DOI: 10.1103/PhysRev.122.1821. URL: <https://link.aps.org/doi/10.1103/PhysRev.122.1821>.
- [17] M. Cohen and J. Chelikowsky. *Electronic Structure and Optical Properties of Semiconductors*. Springer Series in Solid-State Sciences. Springer Berlin Heidelberg, 2012. ISBN: 9783642970801.
- [18] A. Duncan, U. Ravaioli, and J. Jakumeit. “Full-band Monte Carlo investigation of hot carrier trends in the scaling of metal-oxide-semiconductor field-effect transistors”. In: *IEEE Transactions on Electron Devices* 45.4 (Apr. 1998), pp. 867–876. ISSN: 0018-9383. DOI: 10.1109/16.662792.
- [19] C. Ericson. *Real-Time Collision Detection*. Morgan Kaufmann series in interactive 3D technology Bd. 1. Taylor & Francis, 2004. ISBN: 9781558607323.
- [20] G. Fasching, H. Hauser, and W. Smetana. *Werkstoffe für die Elektrotechnik: Aufgabensammlung*. Bd. 2. Springer Vienna, 1995. ISBN: 9783211826843.

- [21] W. Fawcett, A. Boardman, and S. Swain. “Monte Carlo determination of electron transport properties in gallium arsenide”. In: *Journal of Physics and Chemistry of Solids* 31.9 (1970), pp. 1963–1990. ISSN: 0022-3697. DOI: [https://doi.org/10.1016/0022-3697\(70\)90001-6](https://doi.org/10.1016/0022-3697(70)90001-6). URL: <http://www.sciencedirect.com/science/article/pii/0022369770900016>.
- [22] A. Gnudi, D. Ventura, and G. Baccarani. “One-Dimensional Simulation of a Bipolar Transistor by means of Spherical Harmonics Expansion of the Boltzmann Transport Equation”. In: *Proceedings of SISDEP*. Vol. 4. 1991, pp. 205–213.
- [23] A. Gnudi, D. Ventura, G. Baccarani, and F. Odeh. “Two-dimensional MOS-FET simulation by means of a multidimensional spherical harmonics expansion of the Boltzmann transport equation”. In: *Solid-State Electronics* 36.4 (1993), pp. 575–581. ISSN: 0038-1101. DOI: [https://doi.org/10.1016/0038-1101\(93\)90269-V](https://doi.org/10.1016/0038-1101(93)90269-V). URL: <http://www.sciencedirect.com/science/article/pii/003811019390269V>.
- [24] N. Goldsman. “Modeling Electron Transport and Degradation Mechanisms in Semi-conductor Submicron Devices”. PhD thesis. Cornell University, 1089.
- [25] N. Goldsman, L. Henrickson, and J. Frey. “A physics-based analytical/numerical solution to the Boltzmann transport equation for use in device simulation”. In: *Solid-State Electronics* 34.4 (1991), pp. 389–396. ISSN: 0038-1101. DOI: [https://doi.org/10.1016/0038-1101\(91\)90169-Y](https://doi.org/10.1016/0038-1101(91)90169-Y). URL: <http://www.sciencedirect.com/science/article/pii/003811019190169Y>.
- [26] N. Goldsman, C.-K. Lin, Z. Han, and C.-K. Huang. “Advances in the Spherical Harmonic–Boltzmann–Wigner approach to device simulation”. In: *Superlattices and Microstructures* 27.2 (2000), pp. 159–175. ISSN: 0749-6036. DOI: <https://doi.org/10.1006/spmi.1999.0810>. URL: <http://www.sciencedirect.com/science/article/pii/S0749603699908108>.
- [27] T. Grasser, H. Kosina, M. Gritsch, and S. Selberherr. “Using six moments of Boltzmann’s transport equation for device simulation”. In: *Journal of Applied Physics* 90.5 (2001), pp. 2389–2396. DOI: 10.1063/1.1389757. URL: <https://doi.org/10.1063/1.1389757>.
- [28] T. Grasser, H. Kosina, and S. Selberherr. “Investigation of spurious velocity overshoot using Monte Carlo data”. In: *Applied Physics Letters* 79.12 (2001), pp. 1900–1902. DOI: 10.1063/1.1405000. URL: <https://doi.org/10.1063/1.1405000>.

Bibliography

- [29] Grasser, Kosik, Jungemann, Kosina, Meinerzhagen, and Selberherr. “A non-parabolic six moments model for the simulation of sub-100 nm devices”. In: *2004 Abstracts 10th International Workshop on Computational Electronics*. Oct. 2004, pp. 36–37. DOI: 10.1109/IWCE.2004.1407308.
- [30] M. Gritsch. “Numerical Modeling of Silicon-on-Insulator MOSFETs”. PhD thesis. Technische Universität Wien, 2002.
- [31] C. Guerin, V. Huard, and A. Bravaix. “The Energy-Driven Hot-Carrier Degradation Modes of nMOSFETs”. In: *IEEE Transactions on Device and Materials Reliability* 7.2 (June 2007), pp. 225–235. ISSN: 1530-4388. DOI: 10.1109/TDMR.2007.901180.
- [32] C. Guerin, V. Huard, and A. Bravaix. “General framework about defect creation at the SiSiO₂ interface”. In: *Journal of Applied Physics* 105.11 (2009), p. 114513. DOI: 10.1063/1.3133096. URL: <https://doi.org/10.1063/1.3133096>.
- [33] R. N. Hall. “Electron-Hole Recombination in Germanium”. In: *Phys. Rev.* 87 (2 July 1952), pp. 387–387. DOI: 10.1103/PhysRev.87.387. URL: <https://link.aps.org/doi/10.1103/PhysRev.87.387>.
- [34] J. M. Hammersley and D. C. Handscomb. *Monte Carlo Methods*. Methuen’s monographs on applied probability and statistics. Methuen, 1964.
- [35] C. Herring. “A New Method for Calculating Wave Functions in Crystals”. In: *Phys. Rev.* 57 (12 June 1940), pp. 1169–1177. DOI: 10.1103/PhysRev.57.1169. URL: <https://link.aps.org/doi/10.1103/PhysRev.57.1169>.
- [36] R. Herrmann and U. Preppernau. *Elektronen im Kristall*. Springer Vienna, 1980. ISBN: 9783211814888.
- [37] K. Hess. *Advanced theory of semiconductor devices*. Solid state physical electronics series. Prentice-Hall, 1988. ISBN: 9780130115119.
- [38] S. M. Hong, A. T. Pham, and C. Jungemann. *Deterministic Solvers for the Boltzmann Transport Equation*. Computational Microelectronics. Springer Vienna, 2011. ISBN: 9783709107782.
- [39] S.-M. Hong and C. Jungemann. “A fully coupled scheme for a Boltzmann-Poisson equation solver based on a spherical harmonics expansion”. In: *Journal of Computational Electronics* 8.3 (Oct. 2009), p. 225. ISSN: 1572-8137. DOI: 10.1007/s10825-009-0294-y. URL: <https://doi.org/10.1007/s10825-009-0294-y>.

- [40] S. Hong, G. Matz, and C. Jungemann. “A Deterministic Boltzmann Equation Solver Based on a Higher Order Spherical Harmonics Expansion With Full-Band Effects”. In: *IEEE Transactions on Electron Devices* 57.10 (Oct. 2010), pp. 2390–2397. ISSN: 0018-9383. DOI: 10.1109/TED.2010.2062519.
- [41] G. Indalecio and H. Kosina. “Monte Carlo Simulation of Electron-electron Interactions in Bulk Silicon”. In: *Book of Abstracts of The 12th International Conference on Scientific Computing in Electrical Engineering*. Sept. 2018, pp. 97–98.
- [42] J. D. Jackson, C. Witte, and K. Müller. *Klassische Elektrodynamik*. Überarbeitete Auflage. De Gruyter, 2006. ISBN: 9783110189704.
- [43] C. Jacoboni and P. Lugli. *The Monte Carlo Method for Semiconductor Device Simulation*. Wien-New York: Springer, 1989. ISBN: 3-211-82110-4.
- [44] C. Jacoboni, R. Minder, and G. Majni. “Effects of band non-parabolicity on electron drift velocity in silicon above room temperature”. In: *Journal of Physics and Chemistry of Solids* 36.10 (1975), pp. 1129–1133. ISSN: 0022-3697. DOI: [https://doi.org/10.1016/0022-3697\(75\)90055-4](https://doi.org/10.1016/0022-3697(75)90055-4). URL: <http://www.sciencedirect.com/science/article/pii/0022369775900554>.
- [45] C. Jacoboni, P. Poli, and L. Rota. “A new Monte Carlo technique for the solution of the Boltzmann transport equation”. In: *Solid-State Electronics* 31.3 (1988), pp. 523–526. ISSN: 0038-1101. DOI: [https://doi.org/10.1016/0038-1101\(88\)90332-2](https://doi.org/10.1016/0038-1101(88)90332-2). URL: <http://www.sciencedirect.com/science/article/pii/0038110188903322>.
- [46] C. Jacoboni and L. Reggiani. “The Monte Carlo method for the solution of charge transport in semiconductors with applications to covalent materials”. In: *Rev. Mod. Phys.* 55 (3 July 1983), pp. 645–705. DOI: 10.1103/RevModPhys.55.645. URL: <https://link.aps.org/doi/10.1103/RevModPhys.55.645>.
- [47] F. James. “Monte Carlo theory and practice”. In: *Reports on Progress in Physics* 43.9 (1980), pp. 1144–1189. DOI: 10.1088/0034-4885/43/9/002. URL: <https://doi.org/10.1088/0034-4885/43/9/002>.
- [48] S. Jin, S. Hong, and C. Jungemann. “An Efficient Approach to Include Full-Band Effects in Deterministic Boltzmann Equation Solver Based on High-Order Spherical Harmonics Expansion”. In: *IEEE Transactions on Electron Devices* 58.5 (May 2011), pp. 1287–1294. ISSN: 0018-9383. DOI: 10.1109/TED.2011.2108659.
- [49] A. Jünger. *Transport Equations for Semiconductors*. Lecture Notes in Physics. Springer Berlin Heidelberg, 2009. ISBN: 9783540895268.

Bibliography

- [50] C. Jungemann, A. T. Pham, B. Meinerzhagen, C. Ringhofer, and M. Bollhöfer. “Stable discretization of the Boltzmann equation based on spherical harmonics, box integration, and a maximum entropy dissipation principle”. In: *Journal of Applied Physics* 100.2 (2006), p. 024502. DOI: 10.1063/1.2212207. URL: <https://doi.org/10.1063/1.2212207>.
- [51] C. Jungemann and B. Meinerzhagen. *Hierarchical Device Simulation*. Springer, 2003.
- [52] M. H. Kalos and P. A. Whitlock. *Monte Carlo Methods, Volume 1: Basics*. Monte Carlo Methods. Wiley, 1986. ISBN: 9780471898399.
- [53] C. Kittel. *Einführung in die Festkörperphysik*. Oldenbourg, 2006. ISBN: 9783486577235.
- [54] C. Kittel and C. J. Fong. *Quantentheorie der Festkörper*. Oldenbourg, 1989. ISBN: 3486214209.
- [55] C. Kittel. *Introduction to Solid State Physics*. Wiley, 2004. ISBN: 9780471415268.
- [56] L. Kleinman. “Relativistic norm-conserving pseudopotential”. In: *Phys. Rev. B* 21 (6 Mar. 1980), pp. 2630–2631. DOI: 10.1103/PhysRevB.21.2630. URL: <https://link.aps.org/doi/10.1103/PhysRevB.21.2630>.
- [57] N. Koike and K. Tatsuuma. “A drain avalanche hot carrier lifetime model for n- and p-channel MOSFETs”. In: *2002 IEEE International Reliability Physics Symposium. Proceedings. 40th Annual (Cat. No.02CH37320)*. Apr. 2002, pp. 86–92. DOI: 10.1109/RELPHY.2002.996614.
- [58] H. Kosina, M. Harrer, P. Vogl, and S. Selberherr. “A Monte Carlo Transport Model Based on Spherical Harmonics Expansion of the Valence Bands”. In: *Proceedings of the International Conference on Simulation of Semiconductor Devices and Processes (SISDEP)*. 1995, pp. 396–399.
- [59] H. Kosina, M. Nedjalkov, and S. Selberherr. “Theory of the Monte Carlo Method for Semiconductor Device Simulation”. In: *IEEE Transactions on Electron Devices* 47.10 (2000), pp. 1898–1908.
- [60] H. Kosina. “Simulation des Ladungstransportes in elektronischen Bauelementen mit Hilfe der Monte-Carlo-Methode”. PhD thesis. Technische Universität Wien, 1992.
- [61] H. Kosina, M. Nedjalkov, and S. Selberherr. “The stationary Monte Carlo method for device simulation. Part I. Theory”. In: *Journal of Applied Physics* 93.6 (2003), pp. 3553–3563.

- [62] H. Kosina, M. Nedjalkov, and S. Selberherr. “A Stable Backward Monte Carlo Method for the Solution of the Boltzmann Equation”. In: *Large-Scale Scientific Computing*. Ed. by I. Lirkov, S. Margenov, J. Waśniewski, and P. Yalamov. Berlin, Heidelberg: Springer Berlin Heidelberg, 2004, pp. 170–177. ISBN: 978-3-540-24588-9.
- [63] P. W. Lagger. “Scattering Operators for the Spherical Harmonics Expansion of the Boltzmann Transport Equation”. MA thesis. Technische Universität Wien.
- [64] P. Lugli and D. K. Ferry. “Degeneracy in the ensemble Monte Carlo method for high-field transport in semiconductors”. In: *IEEE Transactions on Electron Devices* 32.11 (Nov. 1985), pp. 2431–2437. ISSN: 0018-9383. DOI: 10.1109/T-ED.1985.22291.
- [65] M. Lundstrom. *Fundamentals of carrier transport*. Cambridge University Press, 2000.
- [66] P. Markowich, C. Ringhofer, and C. Schmeiser. *Semiconductor Equations*. Springer Vienna, 2011. ISBN: 9783709169629.
- [67] R. M. Martin. *Electronic Structure: Basic Theory and Practical Methods*. Cambridge University Press, 2004. ISBN: 9780521782852.
- [68] D. Matz. “Hot-carrier distribution function in nonparabolic energy bands”. In: *Journal of Physics and Chemistry of Solids* 28.3 (1967), pp. 373–382. ISSN: 0022-3697. DOI: [https://doi.org/10.1016/0022-3697\(67\)90302-2](https://doi.org/10.1016/0022-3697(67)90302-2). URL: <http://www.sciencedirect.com/science/article/pii/0022369767903022>.
- [69] W. McMahon, K. Matsuda, J. Lee, K. Hess, and J. Lyding. “The Effects of a Multiple Carrier Model of Interface States Generation of Lifetime Extraction for MOSFETs,” in: *Proc. Int. Conf. Mod. Sim. Micro*. Vol. 1. 2002, pp. 576–579.
- [70] B. Meinerzhagen and W. L. Engl. “The influence of the thermal equilibrium approximation on the accuracy of classical two-dimensional numerical modeling of silicon submicrometer MOS transistors”. In: *IEEE Transactions on Electron Devices* 35.5 (May 1988), pp. 689–697. ISSN: 0018-9383. DOI: 10.1109/16.2514.
- [71] *Minimos-NT User Manual*. 2018. URL: www.globaltcad.com.
- [72] B. Nag. *Electron Transport in Compound Semiconductors*. Springer Series in Solid-State Sciences. Springer Berlin Heidelberg, 1980. ISBN: 9783540098454.

Bibliography

- [73] M. Nedjalkov and P. Vitanov. “Iteration approach for solving the Boltzmann equation with the Monte Carlo method”. In: *Solid-State Electronics* 32.10 (1989), pp. 893–896. ISSN: 0038-1101. DOI: [https://doi.org/10.1016/0038-1101\(89\)90067-1](https://doi.org/10.1016/0038-1101(89)90067-1). URL: <http://www.sciencedirect.com/science/article/pii/0038110189900671>.
- [74] M. E. J. Newmann and G. T. Barkema. *Monte Carlo Methods in Statistical Physics*. Oxford University Press, 1999.
- [75] S. K. Park and K. W. Miller. “Random Number Generators: Good Ones Are Hard to Find”. In: *Commun. ACM* 31.10 (Oct. 1988), pp. 1192–1201. ISSN: 0001-0782. DOI: 10.1145/63039.63042. URL: <http://doi.acm.org/10.1145/63039.63042>.
- [76] J. C. Phillips and L. Kleinman. “New Method for Calculating Wave Functions in Crystals and Molecules”. In: *Phys. Rev.* 116 (2 Oct. 1959), pp. 287–294. DOI: 10.1103/PhysRev.116.287. URL: <https://link.aps.org/doi/10.1103/PhysRev.116.287>.
- [77] A. Prechtl. *Elektrodynamik*. TU Wien, 2005.
- [78] P. J. Price. “Monte Carlo Calculation of Electron Transport in Solids”. In: *Lasers, Junctions, Transport*. Ed. by R. Willardson and A. C. Beer. Vol. 14. Semiconductors and Semimetals. Elsevier, 1979, pp. 249–308. DOI: [https://doi.org/10.1016/S0080-8784\(08\)60267-7](https://doi.org/10.1016/S0080-8784(08)60267-7). URL: <http://www.sciencedirect.com/science/article/pii/S0080878408602677>.
- [79] Y. M. Randriamihaja, X. Federspie, V. Huard, A. Bravaix, and P. Palestri. “New Hot Carrier degradation modeling reconsidering the role of EES in ultra short N-channel MOSFETs”. In: *2013 IEEE International Reliability Physics Symposium (IRPS)*. Apr. 2013, XT.1.1–XT.1.5. DOI: 10.1109/IRPS.2013.6532116.
- [80] S. E. Rauch, F. J. Guarin, and G. LaRosa. “Impact of E-E scattering to the hot carrier degradation of deep submicron NMOSFETs”. In: *IEEE Electron Device Letters* 19.12 (Dec. 1998), pp. 463–465. ISSN: 0741-3106. DOI: 10.1109/55.735747.
- [81] C. Rocchini and P. Cignoni. “Generating Random Points in a Tetrahedron”. In: *Journal of Graphics Tools* 5 (Feb. 2001). DOI: 10.1080/10867651.2000.10487528.
- [82] W. Roosbroeck. “Theory of the Flow of Electrons and Holes in Germanium and Other Semiconductors”. In: *Bell System Technical Journal* 29.4 (1950), pp. 560–607. DOI: 10.1002/j.1538-7305.1950.tb03653.x. URL: <https://onlinelibrary.wiley.com/doi/abs/10.1002/j.1538-7305.1950.tb03653.x>.

- [83] R. Y. Rubinstein. *Simulation and the Monte Carlo Method*. John Wiley & Sons, 1981.
- [84] K. Rupp. “Numerical Solution of the Boltzmann Transport Equation using Spherical Harmonics Expansions”. MA thesis. Technische Universität Wien, 2009.
- [85] K. Rupp, T. Grasser, and A. Jüngel. “On the feasibility of spherical harmonics expansions of the Boltzmann transport equation for three-dimensional device geometries”. In: *2011 International Electron Devices Meeting*. Dec. 2011, pp. 34.1.1–34.1.4.
- [86] K. Rupp, C. Jungemann, S.-M. Hong, M. Bina, T. Grasser, and A. Jüngel. “A review of recent advances in the spherical harmonics expansion method for semiconductor device simulation”. In: *Journal of Computational Electronics* 15.3 (Sept. 2016), pp. 939–958. ISSN: 1572-8137. DOI: 10.1007/s10825-016-0828-z. URL: <https://doi.org/10.1007/s10825-016-0828-z>.
- [87] K. Rupp. “Deterministic Numerical Solution of the Boltzmann Transport Equation”. PhD thesis. Technische Universität Wien, 2011.
- [88] E. Sangiorgi, B. Ricco, and F. Venturi. “An efficient Monte Carlo Simulator for MOS devices”. In: *IEEE Transactions on Computer-Aided Design of Integrated Circuits and Systems* 7.2 (Feb. 1988), pp. 259–271. ISSN: 0278-0070.
- [89] F. Schwabl. *Quantenmechanik (QM I)*. Springer-Lehrbuch. Springer, 2002. ISBN: 9783540431060.
- [90] K. Seeger. *Semiconductor Physics: An Introduction*. Handbook of Experimental Pharmacology. Springer-Verlag, 1989. ISBN: 9783540194101.
- [91] S. Selberherr. *Analysis and Simulation of Semiconductor Devices*. Springer Vienna, 1984. ISBN: 9783211818008.
- [92] P. Sharma, S. Tyaginov, S. E. Rauch, J. Franco, A. Makarov, M. I. Vexler, B. Kaczer, and T. Grasser. “Hot-Carrier Degradation Modeling of Decanometer nMOSFETs Using the Drift-Diffusion Approach”. In: *IEEE Electron Device Letters* 38.2 (Feb. 2017), pp. 160–163. ISSN: 0741-3106. DOI: 10.1109/LED.2016.2645901.
- [93] W. Shockley and W. T. Read. “Statistics of the Recombinations of Holes and Electrons”. In: *Physical Review* 87 (5 Sept. 1952), pp. 835–842. DOI: 10.1103/PhysRev.87.835. URL: <https://link.aps.org/doi/10.1103/PhysRev.87.835>.

Bibliography

- [94] T. Simlinger, H. Brech, T. Grave, and S. Selberherr. “Simulation of Submicron Double-Heterojunction High Electron Mobility Transistors with MINIMOS-NT”. In: *IEEE Transactions on Electron Devices* 44 (1997), pp. 700–707.
- [95] J. Singh. *Electronic and Optoelectronic Properties of Semiconductor Structures*. Cambridge University Press, 2003. ISBN: 9780521823791.
- [96] R. Sonderfeld. “Numerical Calculation of Semiconductor Band Structures”. MA thesis. Technische Universität Wien, 2014.
- [97] K. Sonoda, M. Yamaji, K. Taniguchi, C. Hamaguchi, and S. T. Dunham. “Moment expansion approach to calculate impact ionization rate in submicron silicon devices”. In: *Journal of Applied Physics* 80.9 (1996), pp. 5444–5448. DOI: 10.1063/1.362732. URL: <https://doi.org/10.1063/1.362732>.
- [98] R. Stratton. “Diffusion of Hot and Cold Electrons in Semiconductor Barriers”. In: *Phys. Rev.* 126 (6 June 1962), pp. 2002–2014. DOI: 10.1103/PhysRev.126.2002. URL: <https://link.aps.org/doi/10.1103/PhysRev.126.2002>.
- [99] S. Sze and K. Ng. *Physics of Semiconductor Devices*. Wiley, 2006. ISBN: 9780470068304.
- [100] N. Takenaka, M. Inoue, and Y. Inuishi. “Influence of Inter-Carrier Scattering on Hot Electron Distribution Function in GaAs”. In: *Journal of the Physical Society of Japan* 47.3 (1979), pp. 861–868. DOI: 10.1143/JPSJ.47.861. URL: <https://doi.org/10.1143/JPSJ.47.861>.
- [101] J. Y. Tang and K. Hess. “Theory of hot electron emission from silicon into silicon dioxide”. In: *Journal of Applied Physics* 54.9 (1983), pp. 5145–5151. DOI: 10.1063/1.332738. URL: <https://doi.org/10.1063/1.332738>.
- [102] K. Tomizawa. *Numerical Simulation of Submicron Semiconductor Devices*. Artech House, 1993.
- [103] J. Y. Tsai, T. C. Chang, C. E. Chenn, S. H. Ho, K. J. Liu, Y. Lu, X. W. Liu, T. Y. Tseng, O. Cheng, C. T. Huang, and C. S. Lu. “Electron-electron scattering-induced channel hot electron injection in nanoscale n-channel metal-oxide-semiconductor field-effect-transistors with high-k/metal gate stacks”. In: *Applied Physics Letters* 105.14 (2014), p. 143505. DOI: 10.1063/1.4896995. URL: <https://doi.org/10.1063/1.4896995>.
- [104] S. Tyaginov, M. Bina, J. Franco, D. Osintsev, O. Triebel, B. Kaczer, and T. Grasser. “Physical modeling of hot-carrier degradation for short- and long-channel MOSFETs”. In: *2014 IEEE International Reliability Physics Symposium*. June 2014, XT.16.1–XT.16.8. DOI: 10.1109/IRPS.2014.6861193.

- [105] S.-E. Ungersböck. “Numerische Berechnung der Bandstruktur von Halbleitern”. MA thesis. Technische Universität Wien, 2002.
- [106] M. C. Vecchi and M. Rudan. “Modeling electron and hole transport with full-band structure effects by means of the Spherical-Harmonics Expansion of the BTE”. In: *IEEE Transactions on Electron Devices* 45.1 (Jan. 1998), pp. 230–238. ISSN: 0018-9383. DOI: 10.1109/16.658836.
- [107] D. Ventura, A. Gnudi, and G. Baccarani. “Inclusion of Electron-Electron Scattering in the Spherical Harmonics Expansion Treatment of the Boltzmann Transport Equation”. In: *Simulation of Semiconductor Devices and Processes*. Ed. by S. Selberherr, H. Stippel, and E. Strasser. Vienna: Springer Vienna, 1993, pp. 161–164. ISBN: 978-3-7091-6657-4.
- [108] *ViennaSHE User Manual*. 2018. URL: <http://viennashe.sourceforge.net/doc/>.
- [109] *VMC Homepage*. URL: <http://www.iue.tuwien.ac.at/index.php?id=vmc>.
- [110] M. Wagner. “A Base Library for Full Band Monte Carlo Simulations”. MA thesis. Technische Universität Wien, 2004.
- [111] R. Wyckoff. *Crystal Structures*. Wiley, 1963. ISBN: 9780470968604.
- [112] P. YU and M. Cardona. *Fundamentals of Semiconductors: Physics and Materials Properties*. Graduate Texts in Physics. Springer Berlin Heidelberg, 2010. ISBN: 9783642007101.

List of Publications

- [P1] M. Kampl and H. Kosina. “Investigation of Hot-carrier Effects Using a Backward Monte Carlo Method and Full Bands”. In: *Conference Proceedings of International Workshop on Computational Nanotechnology*. 2017, pp. 147–148.
- [P2] M. Kampl, H. Kosina, and O. Baumgartner. “Hot Carrier Study Including e-e Scattering Based on a Backward Monte Carlo Method”. In: *Proceedings of the 22nd International Conference on Simulation of Semiconductor Processes and Devices*. 2017, pp. 293–296.
- [P3] M. Kampl. “Implementation of a backward Monte Carlo algorithm to investigate hot carriers in semiconductor devices”. MA thesis. Technische Universität Wien, 2015.
- [P4] M. Kampl and H. Kosina. “The backward Monte Carlo method for semiconductor device simulation”. In: *Journal of Computational Electronics* 17.4 (Dec. 2018), pp. 1492–1504. ISSN: 1572-8137. DOI: 10.1007/s10825-018-1225-6. URL: <https://doi.org/10.1007/s10825-018-1225-6>.
- [P5] H. Kosina and M. Kampl. “Effect of Electron-Electron Scattering on the Carrier Distribution in Semiconductor Devices”. In: *Proceedings of the 23rd International Conference on Simulation of Semiconductor Processes and Devices*. 2018, pp. 18–21.
- [P6] H. Kosina and M. Kampl. “Current Estimation in Backward Monte Carlo Simulations”. In: *Conference Proceedings of International Workshop on Computational Nanotechnology*. 2019, accepted.

Hiermit erkläre ich, dass die vorliegende Arbeit gemäß dem Code of Conduct – Regeln zur Sicherung guter wissenschaftlicher Praxis (in der aktuellen Fassung des jeweiligen Mitteilungsblattes der TU Wien), insbesondere ohne unzulässige Hilfe Dritter und ohne Benutzung anderer als der angegebenen Hilfsmittel, angefertigt wurde. Die aus anderen Quellen direkt oder indirekt übernommenen Daten und Konzepte sind unter Angabe der Quelle gekennzeichnet.

Die Arbeit wurde bisher weder im In- noch im Ausland in gleicher oder in ähnlicher Form in anderen Prüfungsverfahren vorgelegt.

Datum

Markus Kampl